Universidad de Oviedo

Doctoral Thesis

# Design of electromagnetic band-gap structures using planar technology for RFID and microwave applications

Ramona Cosmina Hadarig

Programa de Doctorado en Tecnologías de la Información y Comunicaciones en Redes Móviles

2014

Tutor: María Elena de Cos Gómez

**Justificación**

El trabajo realizado por la autora de la tesis tiene gran calidad técnica y es altamente innovador, lo que está refrendado por diferentes publicaciones científicas tanto en revistas como en congresos de ámbito internacional:

International Journal Papers:
[1] R.C. Hadarig, M. E. de Cos Gomez and F. Las-Heras: "A Compact Band-Pass Filter with High Selectivity and 2nd Harmonic Suppression" Materials, vol.6, no.12, pp. 5613-5624, 2013.
[2] R.C. Hadarig, M. E. de Cos and F. Las-Heras: "UHF Dipole-AMC Combination for RFID Applications" IEEE Antennas and Wireless Propagation Letters, vol.12, pp. 1041-1044, 2013.
[3] R.C. Hadarig, M. E. de Cos and F. Las-Heras: "Novel Miniaturized Artificial Magnetic Conductor" IEEE Antennas and Wireless Propagation Letters, vol.12, pp. 174-177, 2013.
[4] R.C. Hadarig, M. E. de Cos and F. Las-Heras: "High-Performance Computational Electromagnetic Methods Applied to the Design of Patch Antenna with EBG Structure", International Journal of Antennas and Propagation, vol. 2012, pp.1-5, 2011.
[5] R.C. Hadarig, M. E. de Cos and F. Las-Heras: "Microstrip Patch Antenna Bandwidth Enhancement Using AMC/EBG Structures", International Journal of Antennas and Propagation, vol. 2012, pp.1-6, 2011.
[6] R.C. Hadarig, M. E. de Cos, Y. Alvarez, and F. Las-Heras: "Novel Bow-tie Antenna on Artificial Magnetic Conductor for 5.8 GHz Radio Frequency Identification Tags Usable with Metallic Objects", IET Microwaves, Antennas & Propagation, vol. 5, pp. 1097-1102, 2011.
[7] R.C. Hadarig, M. E. de Cos, Y. Alvarez, and F. Las-Heras: "Novel Bow-tie-AMC Combination for 5.8 GHz RFID Tag Usable with Metallic Objects", IEEE Antennas and Wireless Propagation Letters, vol. 9, pp. 1217-1220, 2010.
150
[8] M. E. de Cos, Y. Alvarez, R.C. Hadarig and F. Las-Heras: "Flexible Uniplanar Artificial Magnetic Conductor", Progress in Electromagnetics Research, PIER, vol. 106, pp. 349-362, 2010.
[9] M. E. de Cos, Y. Alvarez, R.C. Hadarig and F. Las-Heras: "Novel SHF band uniplanar Artificial Magnetic Conductor", IEEE Antennas and Wireless Propagation Letters, vol.9, pp. 44-47, 2010.

International Conference Papers:
[1] R.C. Hotopan, M. E. de Cos and F. Las-Heras: "Small Sized Uniplanar Artificial Magnetic Conductor", 8th European Conference on Antennas and Propagation, EUCAP, The Hague, The Netherlands, April 6 – 11, 2014.
[2] R.C. Hotopan, M. E. de Cos and F. Las-Heras: "Reduced Size CBand Band-pass Filter with 2nd Harmonic Suppression", 8th European Conference on Antennas and Propagation, EUCAP, The Hague,

# RESUMEN DEL CONTENIDO DE TESIS DOCTORAL

| 1.- Título de la Tesis | |
|---|---|
| Español/Otro Idioma: DISEÑO DE ESTRUCTURAS ELECTROMAGNETIC BAND-GAPS EN TECNOLOGÍA PLANAR PARA APLICACIONES DE RFID Y MICROONDAS | Inglés: DESIGN OF ELECTROMAGNETIC BAND-GAP STRUCTURES USING PLANAR TECHNOLOGY FOR RFID AND MICROWAVE APPLICATIONS |

| 2.- Autor | |
|---|---|
| Nombre: RAMONA COSMINA HADARIG | DNI/Pasaporte/NIE: NIE: - PASAPORTE: |
| Programa de Doctorado: TECNOLOGÍAS DE LA INFORMACIÓN Y COMUNICACIONES EN REDES MÓVILES | |
| Órgano responsable: COMISION ACADEMICA DEL PROGRAMA DE DOCTORADO TECNOLOGÍAS DE LA INFORMACIÓN Y COMUNICACIONES EN REDES MÓVILES | |

## RESUMEN (en español)

En la presente Tesis Doctoral se aborda el desarrollo de nuevas estructuras *Electromagnetic Band-Gap* (EBG) / *Artificial Magnetic Conductors* (AMC), para sistemas de comunicación, que proporcionan una mejor funcionalidad y rendimiento, tanto solas como en combinación con antenas. El gran potencial de desarrollo de estas novedosas estructuras ofrece una alternativa para superar las limitaciones de las soluciones actuales. En este contexto las estructuras EBG/AMC son un gran avance, principalmente debido a sus excelentes capacidades para guiar y controlar las ondas electromagnéticas de una manera que los materiales que se encuentran en la naturaleza no pueden.

Esta Tesis Doctoral se ha realizado con la idea de contribuir a mejorar el rendimiento de las estructuras EBG/AMC prestando especial atención a las aplicaciones en las que se utilizan para mejorar las propiedades de antenas (propiedades de la radiación, ancho de banda de funcionamiento, etc.).

La Tesis Doctoral está estructurada en cuatro capítulos. El Capítulo 1 contiene el estado del arte, la motivación, así como el análisis teórico de las estructuras EBG/AMC y las estrategias de diseño que tienen una aplicación directa en los diseños que se han estudiado en capítulos posteriores. Un EBG exhibe propiedades de prevención de propagación de las ondas electromagnéticas en unas direcciones y rangos de frecuencias mientras que un AMC presenta una impedancia de superficie alta y propiedades de reflexión en fase.

Los nuevos aportes científicos generados por la autora comienzan en el Capítulo 2, en el cual se presenta una estructura AMC sin vías, diseñada sobre sustratos rígidos y flexibles. El AMC que posee un amplio ancho de banda de operación (>7%), independencia con respecto al ángulo de polarización y mayor margen de estabilidad angular (±40°) se analiza y describe en detalle. Por otra parte, la miniaturización de los componentes de microondas y antenas se ha hecho cada vez más importante en aquellas las aplicaciones en las cuales el espacio físico es limitado. Por ejemplo, los nuevos terminales de comunicaciones inalámbricas requieren elementos de tamaño cada vez más reducido para lograr sistemas cada vez más compactos. En este contexto, una estructura AMC miniaturizada dependiente de la polarización de la onda incidente y basada en condensadores interdigitales (la dimensión de la celda unidad es más pequeña que $\lambda_0/10$) se estudia y se compara con otras estructuras AMC ya analizadas en la literatura científica.

Es bien conocido que antenas de tipo dipolo funcionan correctamente en el espacio libre, pero cuando se montan sobre objetos metálicos o en la proximidad del cuerpo humano, su rendimiento se degrada notablemente, por ejemplo, se reduce su eficiencia de radiación. Además, la superficie metálica disminuye la impedancia de entrada del dipolo y hace que la frecuencia de resonancia de la antena varíe. Para superar estos problemas y lograr aislar

FOR-MAT-VOA-010-BIS

electromagnéticamente el dipolo del objeto metálico/tejido humano, se utiliza una estructura AMC.

La estructura periódica diseñada para la implementación del AMC puede también bloquear la propagación de ondas electromagnéticas en ciertas bandas de frecuencia y proporcionar un comportamiento de *electromagnetic band-gap* (EBG). Las dos bandas de frecuencias (de AMC y de EBG) pueden no coincidir en la ausencia de vías. La banda de gap de la estructura periódica EBG podría ser calculada utilizando el diagrama de dispersión o empleando el método de la línea *microstrip* suspendida, tal como se presenta en el Capítulo 3. La aplicación de la estructura EBG para ampliar el ancho de banda y mejorar las propiedades de radiación de las antenas se ha analizado también. Por otra parte, aprovechando sus propiedades electromagnéticas (banda prohibida), un filtro paso banda con un tamaño compacto, alta selectividad y supresión del segundo armónico se ha presentado. Una estructura *Defected Ground Structure* (DGS) se desarrolla y se coloca directamente debajo de las líneas de alimentación de entrada / salida del filtro paso banda para obtener la supresión del segundo armónico.

Varios prototipos han sido fabricados y medidos para la validación experimental de todos los diseños. En el Capítulo 4, se recogen las conclusiones derivadas de la presente Tesis Doctoral así como unas posibles líneas futuras de investigación que pueden seguir.

**RESUMEN (en Inglés)**

The Doctoral Thesis has been devoted to the development of new Electromagnetic Band-Gap (EBG)/ Artificial Magnetic Conductors (AMC) structures, for communication systems that can provide improved functionality and performance both alone and combined with antennas. The great potential of developing such novel structures offers an alternative to overcome limitations of current solutions. In this context EBG/AMC structures are a breakthrough, mainly to their exquisite material properties and ability to guide and control electromagnetic waves in a way that natural occurring materials cannot.

Despite the great research effort that has being carried out, there are still quite an amount of investigation in the EBG/AMC area that should be done before these structures could be considered a mature solution to improve their performance in terms of operational bandwidth, angular stability, periodicity, etc. This Doctoral Thesis has been performed with the idea of contributing to some of those aspects, with special emphasis to those related with EBG/AMC applications for improving planar antenna performances (radiation properties, operational bandwidth, etc).

The Doctoral Thesis is organized in four chapters. Chapter 1 contains the state of the art, the motivation, as well as the theoretical analysis of EBG/AMC structures and design strategies which have a direct application on the designs that are studied in later chapters. An EBG exhibits properties of preventing electromagnetic wave propagation in specified directions and frequency ranges whereas an AMC is characterized as presenting high impedance surface and in-phase reflection properties.

The novel scientific contributions generated by the author start in Chapter 2, in which a via less AMC structure on both rigid and flexible substrate is presented. The AMC structure that shows broad AMC operation bandwidth, polarization angle independency and higher angular margin of stability is analyzed and described in detail. Moreover, miniaturization of microwave components and antennas has become increasingly important for applications where physical space is constrained. Modern wireless communication terminals require small microwave elements, which are pertinent to high-level integration into compact light-weight systems. In this context, a miniaturized polarization dependent AMC structures based on interdigital capacitors is studied and compared to other AMC structures presented in the scientific literature.

It is well known that dipole antennas perform properly in free space but when they are mounted on metallic objects or in the proximity of human body, the dipole antenna performance is

seriously degraded, for example the radiation efficiency is decreased. In addition, a metallic surface typically decreases the input impedance of the antenna and varies its resonance frequency. To overcome these problems and to electromagnetically insulate the dipole antenna from the metallic object/human tissue, high impedance surface such as the AMC is used.

The engineered periodic structure that implements the AMC could also block the propagation of electromagnetic waves at certain frequency bands and so exhibiting electromagnetic band-gap (EBG) behavior. The two frequency bands do not necessarily coincide in the absence of vias. The band-gap of an EBG periodic structure could be calculated from its dispersion characteristics or using the suspended microstrip line method as presented in Chapter 3. The application of the EBG structure for enlarging the operational bandwidth and enhancing the radiation properties of antennas is also analyzed. Furthermore, taking advantage of the electromagnetic band-gap properties, a band-pass filter with compact size, high selectivity and second harmonic suppression is presented. A Defective Ground Structure (DGS) design is developed and placed directly under the input/output feeding lines of the band-pass filter to obtain harmonic suppression.

For the experimental validation of all designs, prototypes have been manufactured and measured.

Finally Chapter 4 includes some conclusions related to Doctoral Thesis and some issues to consider in future work.

# Resumen

En la presente Tesis Doctoral se aborda el desarrollo de nuevas estructuras *Electromagnetic Band-Gap* (EBG) / *Artificial Magnetic Conductors* (AMC), para sistemas de comunicación, que proporcionan una mejor funcionalidad y rendimiento, tanto solas como en combinación con antenas. El gran potencial de desarrollo de estas novedosas estructuras ofrece una alternativa para superar las limitaciones de las soluciones actuales. En este contexto las estructuras EBG / AMC son un gran avance, principalmente debido a sus excelentes capacidades para guiar y controlar las ondas electromagnéticas de una manera que los materiales que se encuentran en la naturaleza no pueden. Esta Tesis Doctoral se ha realizado con la idea de contribuir a mejorar el rendimiento de las estructuras EBG/AMC prestando especial atención a las aplicaciones en las que se utilizan para mejorar las propiedades de antenas (propiedades de la radiación, ancho de banda de funcionamiento, etc.).

La Tesis Doctoral está estructurada en cuatro capítulos. El Capítulo 1 contiene el estado del arte, la motivación, así como el análisis teórico de las estructuras EBG/AMC y las estrategias de diseño que tienen una aplicación directa en los diseños que se han estudiado en capítulos posteriores. Un EBG exhibe propiedades de prevención de propagación de las ondas electromagnéticas en unas direcciones y rangos de frecuencias mientras que un AMC presenta una impedancia de superficie alta y propiedades de reflexión en fase.

Los nuevos aportes científicos generados por la autora comienzan en el Capítulo 2, en el cual se presenta una estructura AMC sin vías, diseñada sobre sustratos rígidos y flexibles. El AMC que posee un amplio ancho de banda de operación (>7%), independencia con respecto al ángulo de polarización y mayor margen de estabilidad angular (±40°) se analiza y describe en detalle. Por otra parte, la miniaturización de los componentes de microondas y antenas se ha hecho cada vez más importante en aquellas las aplicaciones en las cuales el espacio físico es limitado. Por ejemplo, los nuevos terminales de comunicaciones inalámbricas requieren elementos de tamaño cada vez más reducido para lograr sistemas cada vez más compactos. En este contexto, una estructura AMC miniaturizada dependiente de la polarización de la onda

incidente y basada en condensadores interdigitales (la dimensión de la celda unidad es más pequeña que $\lambda_0/10$) se estudia y se compara con otras estructuras AMC ya analizadas en la literatura científica.

Es bien conocido que antenas de tipo dipolo funcionan correctamente en el espacio libre, pero cuando se montan sobre objetos metálicos o en la proximidad del cuerpo humano, su rendimiento se degrada notablemente, por ejemplo, se reduce su eficiencia de radiación. Además, la superficie metálica disminuye la impedancia de entrada del dipolo y hace que la frecuencia de resonancia de la antena varíe. Para superar estos problemas y lograr aislar electromagnéticamente el dipolo del objeto metálico/tejido humano, se utiliza una estructura AMC .

La estructura periódica diseñada para la implementación del AMC puede también bloquear la propagación de ondas electromagnéticas en ciertas bandas de frecuencia y proporcionar un comportamiento de *electromagnetic band-gap* (EBG). Las dos bandas de frecuencias (de AMC y de EBG) pueden no coincidir en la ausencia de vías. La banda de *gap* de la estructura periódica EBG podría ser calculada utilizando el diagrama de dispersión o empleando el método de la línea *microstrip* suspendida, tal como se presenta en el Capítulo 3. La aplicación de la estructura EBG para ampliar el ancho de banda y mejorar las propiedades de radiación de las antenas se ha analizado también. Por otra parte, aprovechando sus propiedades electromagnéticas (banda prohibida), un filtro paso banda con un tamaño compacto, alta selectividad y supresión del segundo armónico se ha presentado. Una estructura *Defected Ground Structure* (DGS) se desarrolla y se coloca directamente debajo de las líneas de alimentación de entrada / salida del filtro paso banda para obtener la supresión del segundo armónico.

Varios prototipos han sido fabricados y medidos para la validación experimental de todos los diseños. En el Capítulo 4, se recogen las conclusiones derivadas de la presente Tesis Doctoral así como unas posibles líneas futuras de investigación que pueden seguir.

# Conclusiones

En el presente trabajo se han estudiado y evaluado experimentalmente estructuras de tipo *Electromagnetic Band-Gap* (EBG) y *Artificial Magnetic Conductors* (AMC) para su uso en combinación con antenas.

Tres novedosos diseños de estructuras AMC se han presentado. La primera estructura tiene la frecuencia de resonancia a 5.8 GHz, la segunda es una estructura miniaturizada cuya frecuencia de resonancia varía en función de la polarización de la onda incidente y finalmente la tercera estructura AMC presenta una doble banda de funcionamiento y es insensible a la polarización del campo. Las tres celdas unidad presentan un amplio ancho de banda de funcionamiento y en simulaciones la estabilidad angular supera los 40°. La miniaturización se obtuvo mediante el uso de condensadores interdigitales. La complejidad en el proceso de fabricación se reduce ya que no se utilizan agujeros ni estructuras multicapa.

Se ha propuesto un circuito equivalente de la celda unidad miniaturizada. El resultado analítico concuerda muy bien con el resultado de la simulación electromagnética.

En algunas aplicaciones, sería deseable tener AMCs adaptables a la forma del objeto sobre el que se utilizan sin perder su funcionalidad. Por tanto, los AMCs pueden utilizarse como parte de las etiquetas de identificación de objetos metálicos por radiofrecuencia, incluso en antenas flexibles que pueden ser adheridas al cuerpo fácilmente. Se han seleccionado y probado dos formas diferentes de doblar el AMC, un patrón progresivo (que puede ser utilizado en la industria textil teniendo el AMC integrado en la prenda, un ejemplo es el pliegue producido a la altura del codo cuando se dobla el brazo) y un patrón suave (que puede ser utilizado también en la industria textil colocando el AMC integrado en el tejido: un ejemplo es el pliegue producido sobre la rodilla o hombro). El ancho de banda del AMC flexible y la estabilidad angular no se reducen con respecto a un AMC rígido utilizando el mismo diseño de celda unidad.

El AMC a 5.8 GHz se ha utilizado en combinación con una antena de tipo *bow-tie* que presenta un funcionamiento correcto, tanto sola como cuando se combina con el

AMC y se coloca sobre una placa metálica. La ganancia del conjunto antena-AMC mejora y su diagrama de radiación se conserva cuando se coloca sobre una placa metálica. Se ha escalando el AMC y empleando una antena diferente para trabajar en la banda de 2.4 GHz, se muestran las propiedades electromagnéticas del conjunto. Por otra parte, una combinación dipolo-AMC a 868 MHz se ha conformado alrededor de una muñeca humana. El AMC evita la desadaptación de la antena causada por la proximidad al tejido humano y aísla al cuerpo de la radiación electromagnética no deseada.

Para identificar las propiedades electromagnéticas de las estructuras de tipo *Electromagnetic Band-Gap* (EBG) se ha empleado el método de la línea *microstrip* suspendida y el diagrama de dispersión. El análisis de dispersión de cualquier estructura periódica infinita se ha simulado y analizado mediante la imposición de condiciones de contorno periódicas, con los cambios de fase correspondientes, a la celda unidad. En cuanto a la propagación en una línea microstrip suspendida, el coeficiente de transmisión obtenido por medio de la línea microstrip suspendida muestra un buen acuerdo con el resultado teórico, claramente indicando la presencia de una banda en la cual se reduce la potencia transferida por los prototipos fabricados.

Considerando el resultado predicho por el diagrama de dispersión, se ha diseñado, fabricado y medido un filtro paso banda con alta selectividad a 6.4 GHz. El tamaño compacto, el bajo coste, la fabricación sencilla y la integración con otros componentes en el sistema hacen que sea apropiado para comunicaciones por satélite / terrestre.

Por otra parte, se ha demostrado que se mejora el ancho de banda de la antena de tipo parche utilizando la estructura EBG. Con el objetivo de ampliar el ancho de banda de la antena, la banda de reducción de la potencia transferida de la estructura EBG se ha diseñado para ser adyacente a la banda de frecuencias de la antena de tipo parche. A partir de las medidas se puede concluir que con el conjunto antena-EBG se mejora el ancho de banda de la antena tipo parche y se conservan sus propiedades de radiación sin que sea necesario aumentar el tamaño del prototipo. Además de las anteriores ventajas, el conjunto antena-EBG es compacto, robusto y no requiere múltiples capas de sustrato dieléctrico.

# Abstract

The Doctoral Thesis has been devoted to the development of new Electromagnetic Band-Gap (EBG)/ Artificial Magnetic Conductors (AMC) structures, for communication systems that can provide improved functionality and performance both alone and combined with antennas. The great potential of developing such novel structures offers an alternative to overcome limitations of current solutions. In this context EBG/AMC structures are a breakthrough, mainly to their exquisite material properties and ability to guide and control electromagnetic waves in a way that natural occurring materials cannot. Despite the great research effort that has being carried out, there are still quite an amount of investigation in the EBG/AMC area that should be done before these structures could be considered a mature solution to improve their performance in terms of operational bandwidth, angular stability, periodicity, etc. This Doctoral Thesis has been performed with the idea of contributing to some of those aspects, with special emphasis to those related with EBG/AMC applications for improving planar antenna performances (radiation properties, operational bandwidth, etc).

The Doctoral Thesis is organized in four chapters. Chapter 1 contains the state of the art, the motivation, as well as the theoretical analysis of EBG/AMC structures and design strategies which have a direct application on the designs that are studied in later chapters. An EBG exhibits properties of preventing electromagnetic wave propagation in specified directions and frequency ranges whereas an AMC is characterized as presenting high impedance surface and in-phase reflection properties.

The novel scientific contributions generated by the author start in Chapter 2, in which a via less AMC structure on both rigid and flexible substrate is presented. The AMC structure that shows broad AMC operation bandwidth (>7%), polarization angle independency and higher angular margin of stability under oblique incidence (±40°) is analyzed and described in detail. Moreover, miniaturization of microwave components and antennas has become increasingly important for applications where physical space is constrained. Modern wireless communication terminals require

small microwave elements, which are pertinent to high-level integration into compact light-weight systems. In this context, a miniaturized polarization dependent AMC structures based on interdigital capacitors (the dimension of the unit-cell is smaller than $\lambda_0/10$) is studied and compared to other AMC structures presented in the scientific literature.

It is well known that dipole antennas perform properly in free space but when they are mounted on metallic objects or in the proximity of human body, the dipole antenna performance is seriously degraded, for example the radiation efficiency is decreased. In addition, a metallic surface typically decreases the input impedance of the antenna and varies its resonance frequency. To overcome these problems and to electromagnetically insulate the dipole antenna from the metallic object/human tissue, high impedance surface such as the AMC is used. The engineered periodic structure that implements the AMC could also block the propagation of electromagnetic waves at certain frequency bands and so exhibiting electromagnetic band-gap (EBG) behavior. The two frequency bands do not necessarily coincide in the absence of vias.

The band-gap of an EBG periodic structure could be calculated from its dispersion characteristics or using the suspended microstrip line method as presented in Chapter 3. The application of the EBG structure for enlarging the operational bandwidth and enhancing the radiation properties of antennas is also analyzed. Furthermore, taking advantage of the electromagnetic band-gap properties, a band-pass filter with compact size, high selectivity and second harmonic suppression is presented. A Defective Ground Structure (DGS) design is developed and placed directly under the input/output feeding lines of the band-pass filter to obtain harmonic suppression.

For the experimental validation of all designs, prototypes have been manufactured and measured. Finally Chapter 4 includes some conclusions related to Doctoral Thesis and some issues to consider in future work.

# Contents


**1 Introduction** **5**

1.1 Motivation . . . . . 5

1.2 Literature Overview . . . . . 6

1.2.1 Material Classification . . . . . 6

1.2.2 Electromagnetic Band-Gap (EBG) / Artificial Magnetic Conductor (AMC) Structures and Applications . . . . . 7

1.2.3 Radio Frequency Identification Technology . . . . . 10

1.2.4 Perfect Electric Conductors / Perfect Magnetic Conductors . 12

1.3 Electromagnetic Simulation Methods . . . . . 15

1.4 Contributions of the Thesis . . . . . 15

1.5 Outline of Contents . . . . . 17

**2 Artificial Magnetic Conductor (AMC) Structures** **23**

2.1 Fundamental Concepts . . . . . 24

2.1.1 AMC Design . . . . . 29

2.1.1.1 Flexible AMC Design . . . . . 36

2.1.2 Miniaturized Polarization Dependent AMC Design . . . . . 37

2.1.2.1 Miniaturized Polarization Insensitive AMC Design . 46

2.2 Characterization and Measurement Results in Anechoic Chamber . . 49

2.2.1 Characterization of the AMC Employing Rigid Substrate . . 51

2.2.1.1 Reflection Phase Measurement for AMC Band Determination . . . . . 51

2.2.1.2 Reflection Phase Characterization for Different Field Polarization Angles . . . . . 52

2.2.1.3 Reflection Phase Characterization for Different Incident Angles . . . . . 52

2.2.2 Characterization of the AMC Employing Flexible Substrate . 54

2.2.2.1 Reflection Phase Measurement for AMC Band Determination . . . . . 55
2.2.2.2 Reflection Phase Characterization for Different Field Polarization Angles . . . . . 57
2.2.2.3 Reflection Phase Characterization for Different Incident Angles . . . . . 57
2.2.3 Characterization of the Miniaturized Polarization Dependent AMC . . . . . 59
2.2.3.1 Reflection Phase Measurement for AMC-2 Band Determination . . . . . 59
2.2.3.2 Reflection Phase Characterization for Different Field Polarization Angles . . . . . 61
2.2.3.3 Reflection Phase Characterization for Different Incident Angles . . . . . 61
2.2.4 Characterization of the Miniaturized Polarization Insensitive AMC . . . . . 62
2.2.4.1 Reflection Phase Measurement for AMC Band Determination . . . . . 63
2.2.4.2 Reflection Phase Characterization for Different Field Polarization Angles . . . . . 64
2.2.4.3 Reflection Phase Characterization for Different Incident Angles . . . . . 64
2.3 AMC Analytical Model . . . . . 66
2.3.1 Analytical Model of the Miniaturized Polarization Dependent AMC . . . . . 68
2.3.1.1 Capacitive Interdigital Finger Effect . . . . . 73
2.3.1.2 Inductive Component Width Effect . . . . . 74
2.3.1.3 Gap Width Effect . . . . . 74
2.3.1.4 Dielectric Substrate Thickness Effect . . . . . 75
2.3.1.5 Substrate Dielectric Permittivity Effect . . . . . 76
2.3.2 Analytical Model of the 5.8 GHz AMC . . . . . 77
2.4 AMC Applications . . . . . 79
2.4.1 Application in the 5.8 GHz SHF (Super High Frequency) RFID Band . . . . . 80
2.4.1.1 Bow-tie Design at 5.8 GHz . . . . . 80
2.4.1.2 Bow-tie-AMC Combination . . . . . 83
2.4.1.3 Measurement Results . . . . . 83

2.4.2 Application in the 2.48 GHz SHF (Super High Frequency) RFID Band . . . 89
2.4.2.1 Antenna Design at 2.48 GHz . . . 89
2.4.2.2 Antenna-AMC Combination . . . 89
2.4.2.3 Measurement Results . . . 90
2.4.3 Application in the 868 MHz UHF (Ultra High Frequency) RFID Band . . . 92
2.4.3.1 Dipole Design at 868 MHz . . . 92
2.4.3.2 Dipole-AMC Combination . . . 95
2.4.3.3 Measurement Results . . . 96
2.5 Conclusions . . . 101

**3 Electromagnetic Band-Gap (EBG) Structures 109**
3.1 Fundamental Concepts and Characterization of EBG Structures . . 109
3.1.1 5.8 GHz Electomagnetic Band-Gap Design . . . 113
3.1.1.1 Dispersion Diagram . . . 113
3.1.1.2 Suspended Microstrip . . . 115
3.1.1.3 Comparison Between the AMC and EBG Behaviors 116
3.1.2 Polarization Dependent Electromagnetic Band-Gap Design . 118
3.1.2.1 Suspended Microstrip . . . 118
3.1.2.2 Comparison Between the AMC and EBG Behaviors 119
3.1.3 Polarization Insensitive Electromagnetic Band-Gap Design . 119
3.1.3.1 Suspended Microstrip . . . 119
3.1.3.2 Comparison between the AMC and EBG behaviors 120
3.2 Characterization and Measurement Results Using the Suspended Microstrip Method . . . 120
3.2.1 5.8 GHz Electromagnetic Band-Gap Design . . . 120
3.2.2 Polarization Dependent Electromagnetic Band-Gap Design . 121
3.2.3 Polarization Insensitive Electromagnetic Band-Gap Design . 122
3.3 EBGs Applied to Antennas . . . 123
3.3.1 Bandwidth Enhancement of Patch Antennas . . . 123
3.3.1.1 Patch Antenna Design . . . 123
3.3.1.2 Patch Antenna Combined with EBGs/AMCs . . . 125
3.3.1.3 Measurement Results . . . 127
3.4 EBGs Applied to Filters . . . 132
3.4.1 Band-Pass Filter . . . 132
3.4.1.1 Band-Pass Filter Design . . . 133
3.4.1.2 Second Harmonic Suppression . . . 137

3.4.1.3 Measurement Results . . . . . 138
3.5 Conclusions . . . . . 142

**4 General Conclusions and Future Lines 147**
4.1 Conclusions . . . . . 147
4.2 Future Lines . . . . . 149

**List of publications 150**
Publications Directly Originated by the Thesis . . . . . 150
International Journal Papers . . . . . 150
International Conference Papers . . . . . 151

**List of Figures 153**

**List of Tables 159**

# Chapter 1

# Introduction

**Contents**


**1.1 Motivation** . . . . . **5**

**1.2 Literature Overview** . . . . . **6**

1.2.1 Material Classification . . . . . 6

1.2.2 Electromagnetic Band-Gap (EBG) / Artificial Magnetic Conductor (AMC) Structures and Applications . . . . . 7

1.2.3 Radio Frequency Identification Technology . . . . . 10

1.2.4 Perfect Electric Conductors / Perfect Magnetic Conductors 12

**1.3 Electromagnetic Simulation Methods** . . . . . **15**

**1.4 Contributions of the Thesis** . . . . . **15**

**1.5 Outline of Contents** . . . . . **17**


## 1.1 Motivation

Electromagnetics has received a lot of attention among researchers all over the world because of its immense defense and civil applications. During the Second World War, the use of radar and thereafter the wide use of microwave communication systems facilitated the transformation from radio to microwave frequency. This change demanded more advanced materials for high frequency performance and opened new dimensions in the field of electromagnetic materials.

Now modern fabrication facilities can enable more advanced materials with superior characteristics which cannot be obtained in nature. Such artificial materials with properties which cannot be found in nature are called Metamaterials. Metamaterials cover an extremely large scientific domain which ranges from material

science to antenna engineering [1]. When the periodicity of the unit-cell is much smaller than the operating wavelength, Electromagnetic Band-Gap (EBG) and Artificial Magnetic Conductor (AMC) structures are considered to be metamaterials. Because of their desirable electromagnetic properties [2], they have been widely studied for potential applications in antenna engineering. Microwave filtering has also turned out to be an important area where electromagnetic band-gap materials play an important role.

The Doctoral Thesis has been devoted to the development of new EBG/ AMC structures, for communication systems that can provide improved functionality and performance both alone and combined with antennas. The great potential of developing such novel structures offers an alternative to overcome limitations of current solutions. In this context EBG/AMC structures are a breakthrough, mainly to their exquisite material properties and ability to guide and control electromagnetic waves in a way that natural occurring materials cannot.

Despite the great research effort that has been carried out, there are still quite an amount of investigation in the EBG/AMC area that should be done before these structures could be considered a mature solution to improve their performance in terms of operational bandwidth, angular stability, periodicity, etc. This Doctoral Thesis has been carried out with the idea of contributing to some of those aspects, with special emphasis to those related with EBG/AMC applications for improving planar antenna performance (radiation properties, operational bandwidth, etc). Independent of the application, the continuing demand for small size, wide bandwidth, high efficiency, ease of fabrication, integration, and low cost are always sought in any circuit design. In addition, a compact novel band-pass filter has been designed taking advantage of an EBG unit-cell and relating the dispersion diagram of the structure with its filtering capabilities.

## 1.2 Literature Overview

### 1.2.1 Material Classification

The response of a system to the presence of electromagnetic field is determined by the properties of the materials involved. These properties are described by defining the effective permittivity $\varepsilon_{\text{eff}}$ and effective permeability $\mu_{\text{eff}}$ of the materials. By using effective permittivity $\varepsilon_{\text{eff}}$ and effective permeability $\mu_{\text{eff}}$ the medium classification can be graphically illustrated as shown in Figure 1.1.

A medium with both effective permittivity and permeability greater than zero ($\varepsilon_{\text{eff}} > 0$, $\mu_{\text{eff}} > 0$) is called double positive (DPS) or right hand material (RHM). The double positive case refers to the usual forward wave propagation in common

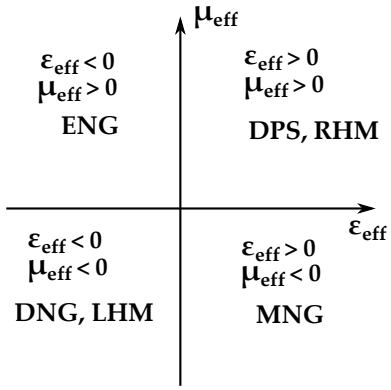


Figure 1.1: Classification of materials.

media (like dielectrics) with positive refractive index.

A medium with effective permittivity less than zero and effective permeability greater than zero ($\varepsilon_{\text{eff}} < 0$, $\mu_{\text{eff}} > 0$) is called Epsilon negative (ENG) medium. In certain frequency regimes many plasmas exhibit this characteristic. For example, noble metals (such as silver, gold) behave in this manner in the infrared (IR) and visible frequency domains. When a single constitutive parameter is negative, the refractive index is pure imaginary which results in lossy evanescent wave propagation in the medium. When both constitutive components are either positive or negative, free wave propagation is enabled.

A medium with effective permittivity greater than zero and effective permeability less than zero ($\varepsilon_{\text{eff}} > 0$, $\mu_{\text{eff}} < 0$) is called Mu negative (MNG) medium. In this category ferroelectric materials can be found.

A medium with both effective permittivity and permeability less than zero ($\varepsilon_{\text{eff}} < 0$, $\mu_{\text{eff}} < 0$) is called Double negative (DNG) or left hand materials (LHM). The last class of materials has only been demonstrated with artificial constructs.

### 1.2.2 Electromagnetic Band-Gap (EBG) / Artificial Magnetic Conductor (AMC) Structures and Applications

Electromagnetic Band-Gap (EBG) and Artificial Magnetic Conductor (AMC) structures are typically periodic artificial media, exhibiting properties which respectively prevent electromagnetic wave propagation in specified directions and frequency ranges (characterizing an EBG) and presenting high impedance surface and in-phase reflection properties (characterizing an AMC). An initial research on EBG/AMC structure at microwave frequencies was conducted by Prof. Yablanovitch and Prof. Sievenpiper [3], which explained many of its properties (surface current

suppression and zero reflection phase).

An AMC is designed to mimic the behavior of a Perfect Magnetic Conductor (PMC) and reflects electromagnetic waves without phase reversal in the electric field as it will be explained in Section 1.2.4. The engineered periodic structure that implements the AMC could also block the propagation of electromagnetic waves at certain frequency bands and so exhibiting electromagnetic band-gap (EBG) behavior. The two frequency bands do not necessarily coincide in the absence of vias [4]. The band-gap of an EBG structure is calculated from its dispersion characteristics [5], obtained using an eigenmode solver. The eigenmode solver determines the resonance frequency for a given wavenumber which is an important parameter to describe the propagation property of electromagnetic waves. The relation between the wavenumber and resonance frequency is often plotted out and referred to as the dispersion diagram [6]. Moreover, the EBG characteristics [7] (in terms of power transfer reduction more than complete band-gap) can be obtained using the suspended microstrip method in which the power transfer reduction band is characterized using the EBG periodic structure as a ground plane for a microstrip transmission line, which is suspended above the structure [8].

The electromagnetic properties of an AMC structure are determined from the reflection phase of an incident plane wave by placing a wave port half wavelength above the structure. As a first approach normal incidence is generally studied. The AMC structure is chosen as reference plane, and the 0° reflection phase defines the frequency of the in-phase reflection [9, 10].

Within the group of planar EBG/AMC, the uniplanar compact EBG/AMC unit-cell (consisting of metallic patches with narrow inset lines on a grounded dielectric substrate) [11] and the mushroom type EBG/AMC unit-cell [3] (consisting of a ground plane, a dielectric substrate, metallic patches and connecting vias) are of particular importance. [8] presents a study on in-phase reflection and wave suppression characteristics of AMC/EBG structures and it is shown that, for a specific set of parameters and for a unit-cell with vias, like the mushroom type unit-cell, the frequency band of the AMC coincides with the frequency band of the EBG. In other words, it exhibits high impedance surface for normally incident waves therefore behaving as an AMC, and at the same frequency does not support surface waves, therefore behaving as an EBG. In [4], an AMC structure composed of square shaped metallic patches with no vias (like the uniplanar compact unit-cell) is studied and it is shown that for the same dimension of metallization, by increasing the gap between unit-cells, the in-phase reflection band shifts to higher frequencies while the band-gap of the EBG structure moves to lower frequencies for the same unit-cell size. Moreover, it is noticed that the in-phase reflection phase occurs at lower fre-

quency for mushroom type AMC unit-cell than the uniplanar compact for the same dimension of unit-cell.

The compactness of EBG/AMC could be evaluated by determining the electrical size of the unit-cell at the resonance frequency (by dividing the unit-cell dimension by the free space wavelength $\lambda_0$). Further enhancement in compactness based on the uniplanar compact EBG/AMC unit-cell using vias, meandering lines, meandered loops, inter-digital capacitors has been introduced in [12].

Different dielectric substrates can be used for designing periodic structures. For reducing the size of the repeated unit-cell in the periodic structure, especially at low frequencies, ceramic composite substrates with high relative permittivity value (the ceramic MCT25 dielectric substrate has a relative dielectric permittivity $\varepsilon_r$= 25) can be used at the expense of increased costs and rigidity. However, for higher $\varepsilon_r$the surface waves are more likely to appear and so EBG structures are even more useful than for lower $\varepsilon_r$dielectric substrates.

Furthermore, the market of flexible printed designs is rapidly growing and for applications that demand flexibility, light weight, and space saving flexible substrates such as ordinary textile fabrics, thermoplastic polymers or paper can be used. In general, textiles present a very low dielectric constant (between $\varepsilon_r$= 1 and $\varepsilon_r$= 2) as they are very flexible porous materials and the presence of air approaches the relative permittivity to one. By lowering the substrate relative dielectric permittivity, the operational bandwidth of the prototype could be enlarged. Regarding the paper or thermoplastic polymer as substrate, the first one is an excellent candidate for an extremely low-cost substrate, especially for applications where mass production is required. The paper presents a relative dielectric permittivity of approximately $\varepsilon_r$= 3 whereas the relative dielectric permittivity of a thermoplastic polymer is between $\varepsilon_r$= 2 and $\varepsilon_r$= 3. Another category of dielectric substrates is represented by the conformal ones, like RO3003 and RO3010, which can be adapted to the shape and conformed to the curved object that will be used.

One important issue in EBG/AMC research is designing miniaturized structures integrated with small antennas to achieve compact systems at a relatively low frequency band (1-10 GHz) and, in the same time, enhancing antenna's performance. Antenna designs have experienced enormous advances in the past decades and they are still under research and development. A series of design requirements, such as low profile, compact size, broad bandwidth, and multiple functionalities, keep on challenging antenna researchers in developing novel antennas. Many new technologies have emerged in the antenna design area and one exciting breakthrough is the development of EBG/AMC structures (to be combined or integrated in the antenna structure).

Many publications are focused on compact EBG/AMC structures combined with antennas [13, 14, 15, 16, 17]. Generally speaking, antennas can benefit from EBG/AMC structures in two ways. On one hand, the EBG structure could be used to surround an antenna in order to increase the bandwidth, the gain, to suppress undesired surface waves and to reduce the mutual couplings in the case of an array. On the other hand, the AMC structure allows the realization of more compact antenna designs and increases the radiation efficiency [18].

In [19] is applied the first EBG [11] structure that improves an aperture coupled microstrip antenna performance. The patch antenna is surrounded by three rows of EBG unit-cells and the measured data show an achievement of a more focused beam in the H plane with over 3 dB gain enhancement. The effect of two different kinds of EBG structures on a microstrip antenna is studied in [20]. The compact resonant cell on the feed line and the resonant cell etched on the ground plane assist to achieve good impedance matching, while successfully reducing the second harmonic. Mutual coupling between elements of a microstrip antenna array mostly results from the excited surface waves and it adversely affects the antenna radiation characteristics. The coupling directions in a microstrip antenna array and some coupling reduction techniques are presented in [21]. Compared to the other methods, the EBG structures are easy to apply and show superior performance in reducing mutual coupling. To obtain more compactness by reducing the patch separation, a multilayer dielectric structure is examined in [22]. Two different materials are integrated such that the antennas are on the top surface, whereas the EBG is sandwiched in between.

A dual band antenna placed over an AMC structure is investigated in [23]. Other low profile antennas with AMC structures are studied in [24].

### 1.2.3 Radio Frequency Identification Technology

The rapid increase on requirements of automatic identification in various areas such as item-level tracking, logistics, access control, electronic toll systems, vehicle security, patients' identification in hospitals, etc. accelerates the demand for Radio Frequency Identification (RFID). RFID systems consist of 3 major parts: a tag, associated with the object to be identified; a reader, used to extract the object's unique identifier from the tag; and an application system [25]. The tags and readers enable the automated identification of tagged objects, and the application system performs important tasks using this captured information. Based on the method of powering the tag, RFID systems are classified as passive (without battery), active (with battery) and semi-active. A passive RFID tag consists of an dipole type antenna and an integrated circuit chip attached at the center. Integrated circuit

chips have complex input impedances, and their impedances vary with frequency. In order to deliver maximum power from the tag antenna to the chip, the input impedance of the proposed tag antenna should be the complex conjugate of the RFID chip according to the complex conjugate matching concept [26, 27].

According to the frequency of operation, the RFID systems are generally divided into four frequency ranges: low frequency (LF) (125-134.2 KHz), high frequency (HF) (13.56 MHz), ultra high frequency (UHF) (433 MHz, 860-960 MHz) and super high frequency (SHF) (2.45 GHz, 5.8 GHz). In addition, the standards of the UHF RFID are different for each country: 866-869 MHz in Europe, 902-928 MHz in America and 950-956 MHz in Asia.

In recent years, passive UHF RFID systems are getting considerable attention because they can provide a long reading range, high data rate and small antenna size. Besides a miniaturized antenna size, the tag antenna should be easily mounted or embedded on any objects, be insensitive to the attached object to keep performance consistent, have a good impedance matching for receiving maximum signals from the reader to power up the chip and have a relative high gain in order to obtain high read range.

The RFID tag is the one that will be mounted on the object. When the RFID reader transmits the electromagnetic wave, any RFID tag within the area will receive the signal and become active. So they can re-transmit the electromagnetic wave back to the RFID reader. But one problem is that a dipole based antenna as the one used in UHF band cannot be attached directly to the metallic object due to the cancellation of currents (image theory) and also due to the change in the antenna's input impedance. Hence, the performance of the RFID tag will be reduced or may not work efficiently. In the worst case scenario, the tag may not be detected by the reader within its normal reading range.

The tag antenna problems for RFID systems are first reported by Prof. Foster and Prof. Burberry [28]. In [29] and [30] the effect of the metallic surface on the dipole antenna was simulated reporting changes in the tag antenna impedance and a decrease in tag's antenna gain when the tag is placed near the metallic plate. The effects of the antenna parameters when placed on paper and plastic are studied in [31], where a shift in the resonance frequency has been reported. In [32] a tag antenna that employs artificial magnetic conductor substrate is designed to have less sensitivity the environment, however the tag antenna parameters like the radiation pattern and impedance characteristics change when placed on metal or glass.

To overcome these problems and to obtain RFID tags usable with metallic objects, researchers have proposed different approaches. The first approach is to design novel antennas rather than dipole like antennas (with the inconvenient of large

thickness or with shorting planes). Patch antennas [33] could be used because they already have a metallic ground plane but they show some shortcomings such as narrow bandwidth. Another possibility that has been already explored is the use of tag antennas based on planar inverted-F structure [34]. Since they already have large ground planes they can operate well on metallic objects. Nevertheless, these type of structures present several important drawbacks such as high cost and difficulty in manufacturing. Other possibilities are to use dipoles separated $\lambda_0/4$ from the metallic object (for example using foam, which leads to thick antenna designs and more complex manufacturing process) or to adopt ferro-electric material as dielectric substrate to insulate the tag from metal (rather expensive). Moreover, Perfect Magnetic Conductors (PMCs) can be used to overcome RFID problems with metals as it will be explained in the Section 1.2.4 and to reduce the backward radiation towards the human body.

### 1.2.4 Perfect Electric Conductors / Perfect Magnetic Conductors

Dipole antennas do not operate efficiently if positioned very close to a Perfect Electric Conductor (PEC) ground plane. By image theory [35], the dipole antenna placed very close above the PEC surface will generate reverse image currents. The image currents in the conductive sheet cancel out the currents in the antenna, resulting in reduced radiation efficiency. This phenomenon can also be explained by considering the phase shift that occurs as the incident wave propagates and than reflects back from the PEC, finally adding with the incident wave. This sequence of operation is shown in Figure 1.2 for a $\lambda_0/4$ distance between the dipole antenna and PEC ground plane. When an electromagnetic wave travels a $\lambda_0/4$ distance, it undergoes a phase change of 90°.

When it impinges the PEC ground plane, it is reflected back and undergoes further 180° phase change. It than travels towards the dipole antenna (by traveling $\lambda_0/4$) and in the process its phase changes by further 90°. Now as shown in Figure 1.2 this wave and the incident wave are in phase. They add up constructively in the forward direction. However if this $\lambda_0/$ 4 spacing is not there, the reflected wave will be 180° out of phase with the incident wave and destructive interference will take place accordingly.

This destructive interference phenomenon is shown in Figure 1.3 for a dipole antenna placed very close to a PEC ground plane. Due to the destructive interference between reflected waves and original waves emitted directly by the radiating element (dipole antenna), the dipole antenna is effectively shorted out by the metal surface and the radiation efficiency is reduced significantly.

This problem can be solved by separating the dipole antenna from the ground

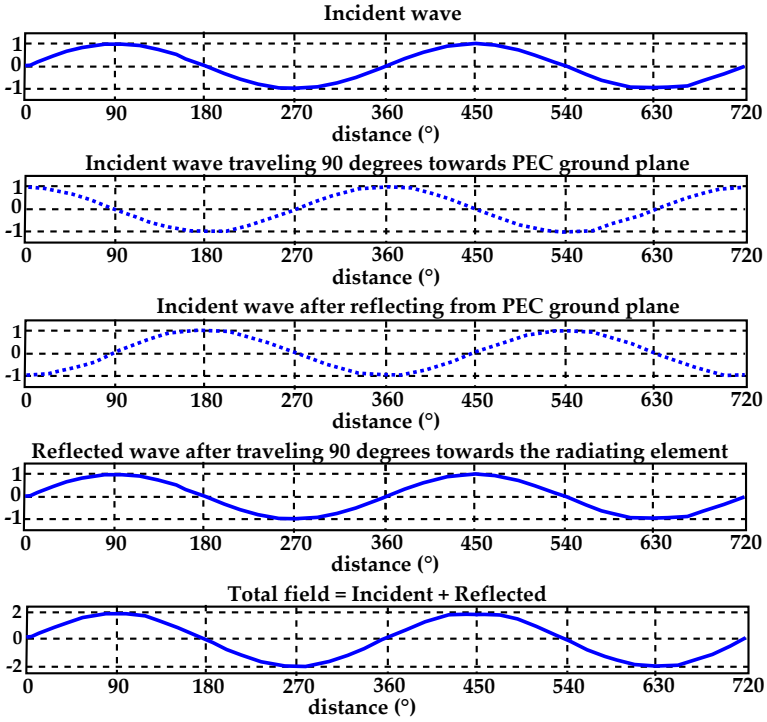


Figure 1.2: Phase change of incident wave for $\lambda_0/4$ spacing between the dipole antenna and PEC ground plane.

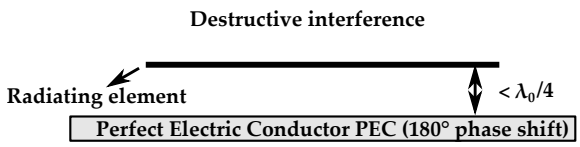


Figure 1.3: Radiating element (dipole antenna) lying parallel and close to the perfect electric conductor.

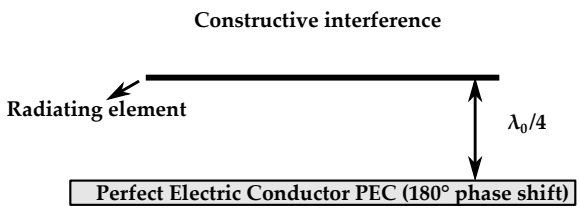


Figure 1.4: Radiating element (dipole antenna) separated $\lambda_0/4$ from the perfect electric conductor.

plane by at least $\lambda_0/4$ as explained in Figure 1.2. This situation is depicted in Figure 1.4, where the two waves will be in phase and will interfere constructively. In this way the antenna will radiate efficiently even when placed close to the perfect electric conductor. However the entire structure requires a minimum thickness of $\lambda_0/4$ which limits its application in low profile antenna designs. The low profile design usually refers to an antenna structure whose overall height is less than $\lambda_0/10$ at the operating frequency. Therefore this minimum thickness requirement is the limiting factor in reducing the antenna profile and also in achieving broadband design.

In contrast to PEC, a Perfect Magnetic Conductor (PMC) will generate in phase rather than out of phase image currents when a dipole antenna is placed above it [3]. This image current will reinforce the dipole antenna current and will increase the antenna's radiation efficiency. Because the reflected wave has no phase shift when returning from the PMC surface, the $\lambda_0/4$ minimum distance is no longer needed. A constructive interference occurs as shown in Figure 1.5. The dipole antenna profile is significantly reduced and the radiation efficiency is increased. However, no natural material has been found to realize such a magnetic conductive surface.

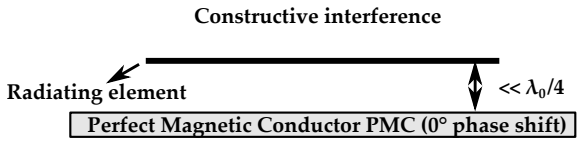


Figure 1.5: Radiating element (dipole antenna) lying parallel above a perfect magnetic conductor ground plane.

Much effort was therefore devoted to realize a PMC artificial surface. In Chapter 2 the artificially engineered AMC that can mimic PMC behavior will be discussed.

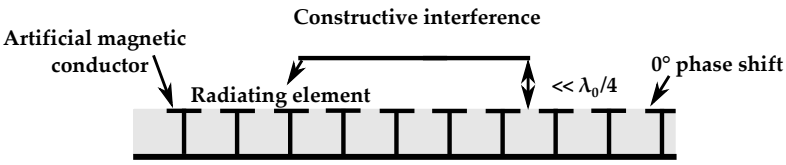


Figure 1.6: Radiating element (dipole antenna) lying parallel above an artificial magnetic conductor.

In Figure 1.6 a radiating element (dipole antenna) lying above an AMC is not shorted out as it would by on a normal metallic ground plane. The AMC reflection phase is 0° unlike 180° of a PEC, thus allows the radiating element to be placed directly above the surface.

## 1.3 Electromagnetic Simulation Methods

The analysis of electromagnetic problems implies solving the Maxwell equations in differential or integral form. The mathematical method used normally depends on parameters such as, required accuracy, simulation time, type of results required, etc. The methods used in this Thesis are Method of Moments (MoM) (an integral equation method) and Finite Element Method (FEM) (a differential equation method). Both of them are frequency domain methods.

In FEM, the tetrahedra cells used in the volume discretization allow for accurate geometrical representation of volumes with curved surfaces and the dielectric materials with arbitrary parameters can be treated easily. By using FEM, arbitrary shaped objects can be oriented arbitrarily in the computational domain. The unknowns of this problem are usually electric field vector components specified along cell edges. Although FEM is based on a volume mesh, the formulation results in a sparse matrix (contains many zero terms) which scales better, with the increase in frequency, than MoM. By using MoM, the matrix is dense (contains mostly non-zero terms). To guarantee adequate calculation accuracy, the largest size of a cell, triangles, polygons, tetrahedra (depending on the method used) has to be much smaller than the wavelength at the highest frequency of the design and even smaller to model sharp variations near corners.

A major advantage of MoM above differential equations based methods such as FEM is that only the structure (antenna, etc) has to be segmentized whereas for FEM the entire computational domain has to be segmentized. In MoM the surface currents are firstly estimated and once knowing the currents the scattered field is computed. MoM is suitable wire antennas, small structures, etc.

In this Thesis, HFSS electromagnetic simulator based on FEM has been used for the design of the AMC structures and for the combination antenna-AMC at 5.8 GHz whereas for the design of the antennas alone and antenna-AMC combinations at 2.4 GHz and 868 MHz and also for the filter design, the electromagnetic simulator ADS based on method of moments has been used.

## 1.4 Contributions of the Thesis

The design of electromagnetic band-gaps / artificial magnetic conductors for RFID and microwave applications is addressed in this Thesis. The main contributions of this Doctoral Thesis are:

- A novel design of a via less AMC unit-cell at 5.8 GHz is introduced in [36]. The design shows broad AMC operation bandwidth, polarization angle independency and

improved angular margin of stability using a thin low-relative dielectric permittivity commercial substrate. More details are discussed in Chapter 2. The same unit-cell is manufactured on a bendable substrate adding the advantage of flexibility to the resulting AMC structure as shown in [37], while preserving the design features remarked above.

- A novel miniaturized polarization dependence AMC unit-cell is introduced in [38] and thoroughly investigated in Section 2.1.2. It is shown that this type of structure, depending on the polarization of the wave, works in either 6.2 GHz or 8.5 GHz frequency bands. Taking as base the miniaturized polarization dependent AMC unit-cell, a polarization insensitive unit-cell made by 2x2 polarization dependent unit-cell has been created.
- An equivalent circuit model for designing artificial magnetic structures is introduced and the analytical results are compared to the electromagnetic simulations. This contribution is discussed in Section 2.3.
- It is demonstrated in Section 2.4 that by combining the dipole antenna with the AMC structure, the resulting prototype shows proper performance in the vicinity of metallic surfaces [39], surrounding a metallic can or being conformed around the human wrist. The work in [40] presents the actual functionality of antennas and AMCs at UHF RFID frequency in order to insulate the user's body from undesired exposure to electromagnetic radiation.
- The dispersion diagram together with the power transfer reduction band of the EBG structure are introduced and discussed in Chapter 3. The position of the band-gap and the frequency of propagating modes from the dispersion diagram depend on the unit-cell geometry and on the substrate's thickness and relative permittivity. A comparison between the EBG and AMC behavior is conducted in Section 3.1.
- Bandwidth enhancement of a microstrip patch antenna by means of EBG structures is introduced in [41] and presented in Section 3.3. Due to the suppressing surface wave effect of the EBG structure, the patch antenna combined with the EBG shows better radiation properties, without having to increase the prototype size or the thickness.
- By taking advantage of the predicted dispersion diagram of the EBG structure, a novel design of band-pass filter with small dimensions and second harmonic suppression is introduced in [42]. The filter presents high selectivity with sharp passband to stopband transition. More details are discussed in Section 3.4.

## 1.5 Outline of Contents

The Doctoral Thesis has been structured into four Chapters. The presented chapter is the first one and contains the motivation of the work that produced this Doctoral Thesis and a literature overview on the theoretical analysis and design of metamaterials such as artificial magnetic conductors and electromagnetic band-gaps using planar technology. Subsequently they have been applied to the design of antennas with enhanced properties for RFID and microwave applications.

In Chapter 2, artificial magnetic conductors and their applications are discussed. The discussion includes operation principle and limitations, full-wave electromagnetic simulation methods for design and analysis of artificial magnetic conductors on both rigid and flexible dielectric substrates and circuit models. In addition, a novel miniaturized polarization dependent AMC based on interdigital capacitors is proposed. Starting from the polarization dependent AMC, a new polarization insensitive AMC is created. The performance of the designed AMCs combined with antennas (bowtie, dipole) in order to obtain a low profile design and to perform on metallic environments and also in the proximity of human tissue is presented through full wave numerical analysis. Two commercial electromagnetic simulation packages (Advanced Design System and Ansoft HFSS) have been used. The prototypes are fabricated using laser micromachining and related measurements are presented to validate the analysis and simulation results.

Using the engineered periodic structure as in Chapter 2, its electromagnetic band-gap properties are studied in Chapter 3. The suspended microstrip method and the dispersion analysis are employed to identify the band-gap and the transfer reduction band of the periodic structure. Some interesting applications like the bandwidth enhancement of a microstrip patch antenna is shown together with a small sized band-pass filter.

Finally Chapter 4 presents some conclusions related to Doctoral Thesis and some issues to consider in future work.

# Bibliography


[1] N. Engheta R. and W. Ziolkowski, "Introduction, history and selected topics in fundamental theories of metamaterials," in Metamaterials: Physics and Engineering Explorations, N. Engheta and R. Ziolkowski, Eds., chapter 1, JohnWiley & Sons, New York, NY, USA, 2006.

[2] A. Alu, M. G. Silveirinha, A. Salandrino, and N. Engheta, "Epsilon-Near-Zero Metamaterials and Electromagnetic Sources: Tailoring the Radiation Phase Pattern," Physical Review B, vol. 75, no. 15, 2007.

[3] D. Sievenpiper, L. Zhang, R. F. J. Broas, N. G. Alexopolous, E. Yablonovitch,, "High-Impedance Electromagnetic Surfaces with a Forbidden Frequency Band," IEEE Transactions on Microwave Theory and Techniques, vol. 47, no. 11, pp. 2059-2074, 1999.

[4] G. Goussetis, A.P. Feresidis and J.C. Vardaxoglou, "Tailoring the AMC and EBG characteristics of periodic metallic arrays printed on grounded dielectric substrate," IEEE Trans. Antennas Propag., vol. 54, no. 1, pp. 82-89, 2006.

[5] Y. Toyota, A. E. Engin, T. H. Kim, and M. Swaminathan, "Stopband analysis using dispersion diagram for two-dimensional electromagnetic bandgap structures in printed circuit boards," IEEE Microwave and Wireless Components Letters, vol. 16, no. 12, pp. 645–647, 2006.

[6] F. Yang and Y. Rahmat-Samii, "Electromagnetic Band Gap Structures in Antenna Engineering," Cambridge University Press, Cambridge, UK, 2009.

[7] A. Ibanez Loinaz, C. de Rio, "EBG at microwave frequency range: Bragg and/or resonant effect?," Microwave and Optical Technology Letters, vol. 42, no. 5, 2004.

[8] A. Aminian, F. Yang, and Y. Rahmat-Samii, "In-phase reflection and EM wave suppression characteristics of electromagnetic band gap ground planes," in

Proceedings of the IEEE International Antennas and Propagation Symposium, pp. 430–433, 2003.

[9] F.R. Yang, Y. Rahmat-Samii, "Reflection phase characterization of an electromagnetic band-gap (EBG) surface," Proc. IEEE AP-S Int Symp., vol. 3, pp. 744-747, 2002.

[10] D. J. Kern, D. H. Werner, A. Monorchio, L. Lanuzza, and M. J. Wilhelm, "The design synthesis of multiband artificial magnetic conductors using high impedance frequency selective surfaces," IEEE Trans. Antennas Propag., vol. 53, no. 1, pp. 8–17, 2005.

[11] F.R. Yang, M. Kuang-Ping, Q. Yongxi, and T. Itoh, "A uniplanar compact photonic-bandgap (UC-PBG) structure and its applications for microwave circuit," Microwave Theory and Techniques IEEE Transactions, vol. 47, no. 8, pp. 1509 – 1514, 1999.

[12] D. Swanson, W. Hoefer, "Microwave Circuit Modeling Using Electromagnetic Field Simulation," Boston: Artech House, 2003.

[13] M. Mantash, A.-C. Tarot , S. Collardey, K. Mahdjoubi, "Investigation of Flexible Textile Antennas and AMC Reflectors," International Journal of Antennas and Propagation, 2012.

[14] K. Mahdjoubi, T.H.Vu, A.C. Tarot, S. Collardey, "An oveview on the design and properties of EBG antennas," 4th European Conference on Antennas and Propagation, EUCAP, pp. 1-3, 2010.

[15] T.H. Vu, K. Mahdjoubi, A.C.Tarot, S. Collardey, "Bandwidth enlargement of planar EBG antennas," LAPC Antenna and Propagation Conference, pp. 125-128, 2007.

[16] Y. Ranga, L. Matekovits, K. P. Esselle, A. R. Weily, "Multilayer Frequency Selective Surface Reflector for Constant Gain over Ultra Wideband," 5th European Conference on Antennas and Propagation, EUCAP, pp. 332-334, 2011.

[17] Y. Ranga, L. Matekovits, K. P. Esselle, A. R. Weily, "Design and analysis of frequency selective surfaces for ultra wideband applications," IEEE EUROCON - International Conference on Computer as a Tool, pp.1-4, 2011.

[18] J.M. Bell, M.F. Iskander, "A Low-Profile Archimedean Spiral Antenna Using an EBG Ground Plane," IEEE antennas and wireless propagation letters, vol. 3, pp. 223-226, 2004.

[19] R. Coccioli, F. R. Yang, K. P. Ma, and T. Itoh, "Aperture-coupled patch antenna on UC-PBG substrate," IEEE Transactions on Microwave Theory and Techiques," vol. 47, no. 11, pp. 2123–2130, 1999.

[20] Y. J. Sung and Y. S. Kim, "An improved design of microstrip patch antennas using photonic bandgap structure," IEEE Transactions on Antennas and Propagation, vol. 53, no. 5, pp. 1799–1804, 2005.

[21] F. Yang and Y. Rahmat-Samii, "Microstrip antennas integrated with electromagnetic band-gap (EBG) structures: a low mutual coupling design for array applications," IEEE Transactions on Antennas and Propagation, vol. 51, pp. 2936-2946, 2003.

[22] E. Rajo-Iglesias, O. Q. Quevedo-Teruel, and L. Inclan-Sanchez, "Mutual coupling reduction in patch antenna arrays by using a planar EBG structure and a multilayer dielectric substrate," IEEE Transactions on Antennas and Propagation, vol. 56, no. 6, pp. 1648–1655, 2008.

[23] M. Mantash, A.C Tarot, S. Collardey, K. Mahdjoubi, "Dual-band CPW-fed G-antenna using an EBG structure," Antennas and Propagation Conf. (LAPC), pp. 453–456, 2010.

[24] Z. Li and Y. Rahmat-Samii, "PBG, PMC and PEC ground planes: A case study of dipole antennas," IEEE Proc. Antennas Propagation Soc. Int. Symp., vol. 2, pp. 674–677, 2000.

[25] R.Want, "An introduction to RFID technology," IEEE Pervasive Computing, vol. 5, no. 1, pp. 25-33, 2006.

[26] Geyi, W., "Derivation of Equivalent Circuits for Receiving Antenna," IEEE Transactions on Antennas and Propagation, vol. 52, no. 6, pp. 1620-1623, 2004.

[27] K.V.S. Rao, V. Nikitin Pavel, F. Lam Sander, "Antenna Design for UHF RFID Tags: A Review and a Practical Application," IEEE Transactions on Antennas and Propagation, vol. 53, no.12, pp. 3870-3876, 2005.

[28] P.R. Foster, R.A. Burberry, "Antenna problems in RFID systems," IEE Colloquium an RFID Technology, pp. 3/1-3/5, 1999.

[29] D. M. Dobkin and S. M. Weigand, "Environmental effects on RFID tag antennas," in IEEE Microw. Symp. Dig., pp. 135–138, 2005.

[30] J. D. Griffin, G. D. Durgin, A. Haldi, and B. Kippelen, "RF Tag Antenna Performance on Various Materials Using Radio Link Budgets," IEEE Antenna and Wireless Propagation Letters, vol. 5, pp. 247-250, 2006.

[31] A.H. Rida, L. Yang, S. S. Basat, A. Ferrer-Vidal, S. Nikolaou, and M. M. Tentzeris, "Design, development and integration of novel antennas for miniaturized UHF RFID tags," IEEE Transactions Antennas and Propagation, vol. 57, no. 11, pp. 3450-3457, 2009.

[32] M. Stupf, R. Mittra, J. Yeo, and J.R. Mosig, "Some Novel Design for RFID Antennas and their Performance Enhancement with Metamaterials," IEEE Antennas and Propagation Society International Symposium, pp.1023-1026, 2006.

[33] L. Ukkonen, M. Schaffrath, D.W. Engels, L. Sydanheimo, M. Kivikoski, "Operability of Folded Microstrip Pach-Type Tag Antenna in the UHF RFID Bands within 865-928 MHz," IEEE Antennas and wireless Propagation Letters, vol. 5, pp. 414-417, 2006.

[34] H. Kwon, B. Lee, "Compact slotted planar inverted-F RFID tag mounted on metallic objects," Electronic Letters, vol. 41, pp. 1091-1092, 2005.

[35] C. A. Balanis, "Antenna Theory: Analysis and Design," $2^{nd}$ ed. New York, NY, USA: Wiley, 1997.

[36] M. E. de Cos, Y. Alvarez-Lopez, R.C. Hadarig and F. Las Heras Andres, "Novel SHF-Band Uniplanar Artificial Magnetic Conductors," IEEE Antennas and Wireless Propagation Letters, vol. 9, pp. 44-47, 2010.

[37] M. E. de Cos, Y. Alvarez-Lopez, R.C. Hadarig and F. Las Heras Andres,"Flexible Uniplanar Artificial Magnetic Conductor," Progress in Electromagnetic Research, vol. 106, pp. 349-362, 2010.

[38] R. C. Hadarig, M. E. de Cos, and F. Las-Heras, "Novel Miniaturized Artificial Magnetic Conductor," IEEE Antennas and Wireless Propagation Letters, vol. 12, pp.174-177, 2013.

[39] R.C. Hadarig, M.E. de Cos Gomez, Y. Alvarez, F. Las-Heras, "Novel Bowtie–AMC Combination for 5.8-GHz RFID Tags Usable with Metallic Objects," IEEE Anten Wirele Propag. Lett., vol. 8, pp. 1217- 1220, 2010.

[40] R.C. Hadarig, M.E. de Cos Gomez, and F. Las-Heras, "UHF Dipole-AMC Combination for RFID Applications," IEEE Anten Wirele Propag. Lett., vol. 12, pp. 1041- 1044, 2013.

[41] R. C. Hadarig, M. E. de Cos, and F. Las-Heras, "Microstrip patch antenna bandwidth enhancement using AMC/EBG structures," International Journal of Antennas Propagation, vol. 2012, 2012.

[42] R. C. Hadarig, M. E. de Cos, and F. Las-Heras, "A Compact Band-Pass Filter with High Selectivity and Second Harmonic Suppression," Materials, vol 6, pp. 5613-5624, 2013.

# Chapter 2

# Artificial Magnetic Conductor (AMC) Structures

## Contents


**2.1 Fundamental Concepts . . . . . 24**

2.1.1 AMC Design . . . . . 29

2.1.2 Miniaturized Polarization Dependent AMC Design . . . . . 37

**2.2 Characterization and Measurement Results in Anechoic Chamber . . . . . 49**

2.2.1 Characterization of the AMC Employing Rigid Substrate . 51

2.2.2 Characterization of the AMC Employing Flexible Substrate 54

2.2.3 Characterization of the Miniaturized Polarization Dependent AMC . . . . . 59

2.2.4 Characterization of the Miniaturized Polarization Insensitive AMC . . . . . 62

**2.3 AMC Analytical Model . . . . . 66**

2.3.1 Analytical Model of the Miniaturized Polarization Dependent AMC . . . . . 68

2.3.2 Analytical Model of the 5.8 GHz AMC . . . . . 77

**2.4 AMC Applications . . . . . 79**

2.4.1 Application in the 5.8 GHz SHF (Super High Frequency) RFID Band . . . . . 80

2.4.2 Application in the 2.48 GHz SHF (Super High Frequency) RFID Band . . . . . 89

2.4.3 Application in the 868 MHz UHF (Ultra High Frequency) RFID Band . . . . . 92

**2.5 Conclusions . . . . . 101**

## 2.1 Fundamental Concepts

Reflection coefficient is a popular parameter used to describe the reflection property of an object. It is defined as the ratio of the reflected field over the incident field at the reflecting surface. Usually, it has a complex value with the corresponding magnitude and phase.

As it is well known, when a plane wave is normally impinged upon a highly conductive flat surface like a Perfect Electric Conductor (PEC), the reflected E field and the incident E field have opposite signs (the tangential component of the total E field becomes zero on the reflecting surface) due to the very low surface impedance. The opposite sign of the reflected and incident E field make the reflection coefficient ($\Gamma$) to be $\Gamma$ = -1. The reflection phase is 180° [1].

However, if a structure is designed to have a very high impedance, the reflection coefficient would be $\Gamma = 1$. This means that the structure can act as a magnetic wall (Perfect Magnetic Conductor (PMC)) in contrast to the conventional PEC wall for which $\Gamma$ = -1. Since $\Gamma = 1$, the tangential component of the total H field is zero (the reflected H field and the incident H field have opposite signs whereas the reflected E field and the incident E field have the same sign and the tangential component of the electric field is significant on the reflecting surface). The corresponding reflection phase is 0°.

Since perfect magnetic conducting surfaces do not exist naturally, it is necessary to artificially create a surface with magnetic conduction properties within a certain band of frequencies. This can be achieved by using resonant inclusions on a host substrate layer over a conducting ground plane. In this way, Artificial Magnetic Conductors (AMCs) are synthesized and can offer interesting potential applications in antennas [2].

AMCs can be conceptualized as 2-dimentional periodic arrangement of small inclusions (also called unit-cells) on a host surface [3]. Electromagnetic properties of such surfaces which can indeed be regarded as a Frequency Selective Surface (FSS) over a ground plane, are influenced by the shape and geometry of these inclusions and also by the substrate's thickness and relative dielectric permittivity of the substrate which are build on [4].

The resonant nature of an AMC results in frequency dependence and generally narrow band operation. At low frequencies (when the dielectric losses are considered negligible) the AMC can be modeled as a parallel LC network [1] under the following conditions: the periodicity of the unit-cell should be much smaller than the

wavelength of operation and the grounded dielectric substrate has to be electrically thin.

Hence, the surface impedance may be represented as

$$Z = \frac{j\omega L}{1 - \omega^2 LC} \tag{2.1}$$

The resonance frequency of the AMC is given by:

$$f_0 = \frac{1}{2\pi\sqrt{LC}} \tag{2.2}$$

The AMC in-phase reflection bandwidth is proportional to:

$$BW \approx \sqrt{\frac{L}{C}} \tag{2.3}$$

The surface impedance of these structures is frequency dependent being inductive below the resonance frequency and supporting Transverse Magnetic (TM) waves and capacitive above it supporting Transverse Electric (TE) waves. As frequency approaches the resonance, the imaginary part of the impedance becomes very large, almost infinity, indicating a PMC (or AMC) behavior (see Figure 2.1).

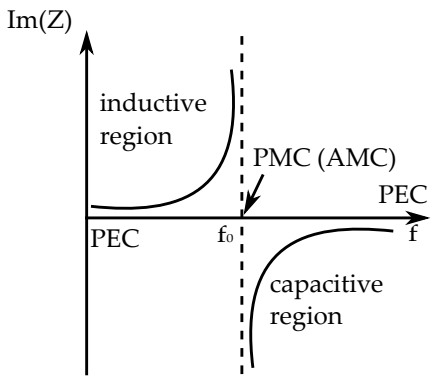


Figure 2.1: Impedance of a parallel resonant circuit.

Towards the goal of constructing an AMC, several geometries for periodic metallization patterns have been studied including mushroom structures [2], Hilbert-Peano curves [5], Jerusalem crosses [6] and dipole or slot arrays [7, 8]. Genetic algorithms (GAs) [3] and particle swarm (PS) [9] which fall under a category of optimization schemes can also be used, but they have the disadvantage of being time and resource consuming due to the need of many parameter optimization: substrate dielectric properties together with unit-cell size and geometry (the unit-cell being

divided into a n by n grid in which each grid element can be either metal or free space).

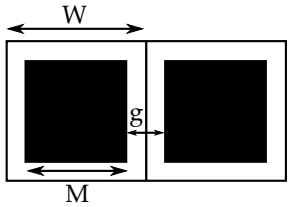


Figure 2.2: Simple square unit-cell.

When designing AMCs, there exist certain trade-offs related to the frequency response and unit-cell size (see Figure 2.2). For example, the bandwidth of the structure is strongly dependent on the substrate properties (such as the substrate thickness and relative dielectric permittivity) and the unit-cell geometry. By increasing the substrate thickness with respect to wavelength (the corresponding inductance increases), the bandwidth can be enlarged. Also by decreasing the relative permittivity of the dielectric substrate, the bandwidth can be further improved. Enlarging the gap between the metallization edge and unit-cell edge (and so the gap between adjacent unit-cells) the capacitance decreases which will enhance the overall bandwidth.

If compact size is required, a high relative permittivity dielectric substrate can be used but this reduces the AMC operation bandwidth and increases the cost. So, a compromise solution regarding relative dielectric permittivity has to be adopted when both compact size and broad AMC operation bandwidth are required. All the mentioned properties and design rules are valid under the consideration that the unit-cell is electrically small compared to the operating wavelength and the thickness of the grounded dielectric substrate is thin enough compared to the unit-cell periodicity.

The ability of the periodic structure to perform as an AMC at a given frequency (the resonance frequency of the structure has to remain invariable) as the incident angle ($\Theta_{inc}$) becomes increasingly oblique for a TE/TM polarized incident wave is defined as TE/TM angular margin of stability. The angular dependance will be determined by applying the methodology in [10].

The angular margin of stability can be improved by varying the gap width versus the unit-cell size ratio. However, the unit-cell size ( $W$), which contains the unit-cell metallization (M) and the gap (g) between adjacent unit-cells, is limited and must be small enough to avoid the appearance of grating lobes according to the formula below[11].

$$W_{max} \leq \frac{\lambda_0}{sin(\Theta_{inc}) + 1} \tag{2.4}$$

where $\lambda_0$ is free space wavelength and $\Theta_{inc}$ is the angle of incidence.

It can be observed that $W_{max}$ must be less than $\lambda_0$ to to make the grating lobe effect on frequency response negligible.

If the maximum allowed unit-cell size is reached, and the AMC angular margin of stability does not meet the requirements, the permittivity of the dielectric substrate should be increased. Moreover, by decreasing also the thickness of the dielectric substrate, the angular margin of stability increases. Choosing the correct gap width versus unit-cell size ratio, almost zero frequency shift of the AMC structure for an arbitrary incident angle can be achieved.

To illustrate the AMC condition, the reflection coefficient phase as a function of frequency is plotted. The reflection phase of the AMC varies with the frequency continuously from 180° to -180° and is 0° at the resonance frequency. At low frequencies, it reflects with a 180° phase shift just like a PEC surface. At higher frequencies, the phase continues to slope downward and approaches -180°. The useful bandwidth of AMC performance is generally defined in the range from 90° to -90° [12], since in this range, the phase values would not cause destructive interference between direct and reflected waves.

According to this, the percentage AMC bandwidth ($BW_{AMC}$) can be computed as:

$$BW_{AMC}(\%) = [(f_{up} - f_{lo}) / f_c] * 100 \tag{2.5}$$

Where $f_{up}$ is the frequency at which reflection phase equals -90°.

$f_{lo}$ is the frequency at which reflection phase equals +90°.

$f_c$ is the center frequency where reflection phase equals 0°.

To accurately identify the electromagnetic properties of the AMC structure, Finite Element Method (FEM) [13] and Bloch-Floquet theory [14] are used to analyze its performance. As the AMC structure is periodic, Bloch-Floquet's theory can be applied (the waves in a periodic structure can propagate without scattering, their behavior being governed by a periodic envelope function multiplied by a plane wave). Therefore, the characterization of the whole AMC structure can be reduced to the analysis of only a single unit-cell.

A single unit-cell of the structure with perfect electric conductor / perfect magnetic conductor Periodic Boundary Condition (PBC) on its four sides can be simulated in order to model an infinite structure (two adjacent sides of the unit-cell are assigned to be one PEC wall and respectively the other one PMC wall). The

electric and magnetic fields in all the unit-cells have the same amplitude and differ by a phase shift.

To obtain the AMC reflection coefficient, a wave port is placed at least half wavelength above the surface (to assure that the simulations are done in far field region) and normal plane waves are launched. As the observation plane and the AMC structure are in different locations, one has to restore the reflected phase exactly to the AMC structure plane of interest, so the reflection phase has to be translated to the AMC plane. To solve this problem, an ideal PEC surface using the same dielectric substrate and being located at the same height as the AMC structure is used as a reference (the observation plane stays the same). By knowing the reflection phase of the PEC simulation, the reflection phase of the AMC structure can be determined. Therefore, the propagation phase due to the distance between observation plane and AMC structure is canceled out.

Let us consider the following:

$\varphi_{\mathrm{AMC}}$ - the reflected phase of the periodic structure on its surface.

$\varphi_{\mathrm{PEC}}$ - the reflected phase of the PEC on its surface, which by definition is 180°.

$\rho_{\mathrm{AMC}}$ - the reflected phase provided by the simulator at the wave port position when the AMC unit-cell is simulated.

$\rho_{\mathrm{PEC}}$ - the reflected phase provided by the simulator at the wave port position when the PEC is simulated.

The reflected phase provided by the simulator at the wave port position when the AMC unit-cell or PEC surface is simulated is:

$$\rho_{AMC} = \varphi_{AMC} + \Delta\Phi \tag{2.6}$$

$$\rho_{PEC} = \varphi_{PEC} + \Delta\Phi = 180^\circ + \Delta\Phi \tag{2.7}$$

$$\Delta\Phi = \rho_{PEC} - 180^\circ \tag{2.8}$$

$\Delta\Phi$ - is the phase shift, equal for both AMC unit-cell and PEC, since they are situated at at the same distance from the wave port, which is where the simulator provides the result.

$$\rho_{AMC} = \varphi_{AMC} + \rho_{PEC} - 180^\circ \tag{2.9}$$

$$\varphi_{AMC} = \rho_{AMC} - \rho_{PEC} + 180^\circ \tag{2.10}$$

So, it is possible to compute the reflected phase of the AMC on its surface by

subtracting the phase value obtained in the first simulation the value obtained in the second and adding π to the result.

Another way to simulate AMC structures is to use master/slave PBC, which allows also to mimic the presence of the unit-cell in a periodic structure extending to infinity. There are two pairs of master/slave surfaces bordering the unit-cell. Two adjacent surfaces are firstly assigned to be master surfaces, and the surfaces opposite to them are then assigned as the corresponding slave for each master.

For normal incidence and polarization angle set to 0°, there is no phase delay between the master and slave boundaries so that the electric field distribution on the slave surface exactly follows that on the master surface. In this case a Floquet port is used and it has the ability to evaluate the AMC periodic structure in all directions of plane wave incidence. The methodology to compute the reflection phase on the AMC surface is the same, as the one previously presented.

### 2.1.1 AMC Design

In their first appearance, AMCs were introduced as periodic patches (or resonant inclusions) shorted to the ground plane via metallic pins. However, it was later shown that they can also be implemented by loading a grounded dielectric substrate with different FSS type periodic metallizations without using via holes.

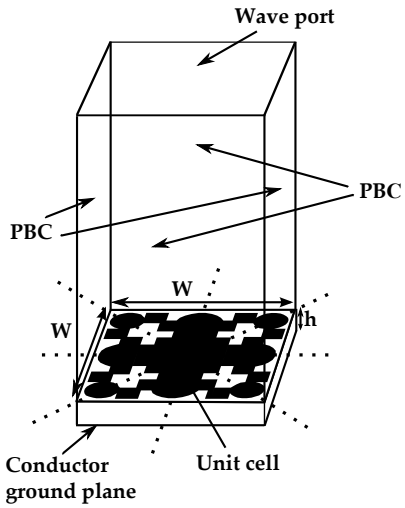


Figure 2.3: Simulation model for determining the reflection properties of the AMC.

To successfully design an AMC structure at a given frequency and in a desirable bandwidth which is typically very narrow, the design has to be optimized for a given dielectric substrate. A patch-type AMC unit-cell is modified and loaded by

slots in order to obtain the 5.8 GHz Super High Frequency (SHF) Radio Frequency Identification (RFID) resonance frequency. In this way the resonance frequency decreases without increasing the unit-cell size and also the bandwidth increases compared to a square shape patch due to the new inductive elements created as a consequence of the introduced slots.

The designed unit-cell geometry is shown in Figure 2.3. A dielectric substrate, ARLON25N, with relative dielectric permittivity $\varepsilon_r = 3.28$, tan $\delta = 0.0025$ and a thickness of $h = 0.762$ mm (30 mils), is used. Unit-cell dimensions are $W$ x $W$ = 11.52 mm x 11.52 mm and its geometry exhibits four symmetry planes. The metallization thickness is 18 µm. Such dimensions result in an AMC operating in the 5.8 GHz SHF RFID band. The gap between conducting parts of the two adjacent unit-cells is kept 0.1 mm to facilitate the fabrication process. It is desirable to have more compact unit-cells and the small the gap, the more compact the unit-cell.

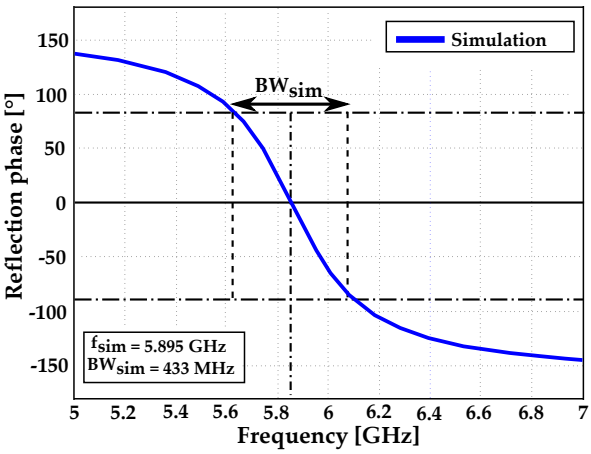


Figure 2.4: Phase of the reflection coefficient on the AMC surface.

Figure 2.4 and Figure 2.5 show the phase and magnitude of the reflection coefficient when the structure is illuminated by a normally incident plane wave. The phase of the reflection coefficient at 5.2 GHz is shown to be approximately 130°. As the frequency decreases, the phase approaches 180°. However, as the frequency increases, this phase passes through 0° and goes towards -180°.

At the frequency where the phase is 0° (5.89 GHz), the structure achieves an overall reflection coefficient $\Gamma$ of approximately 1 (due to the conductor and substrate losses, the reflection coefficient $\Gamma$ is not exactly 1) and has a very high impedance at the resonance frequency, therefore acting as an AMC (see Figure 2.6).

Far away from this resonance, the AMC structure acts as a traditional electric conducting ground plane. The surface impedance is more than 11000 Ω at 5.89 GHz,

a very high value if compared with the free space impedance (120π) or compared with PEC whose surface impedance is close to 0 Ω.

For unit-cell dimensions $W = 11.52$ mm and $h = 0.762$ mm (30 mils) the bandwidth of AMC performance is approximately 433 MHz (7.3%).

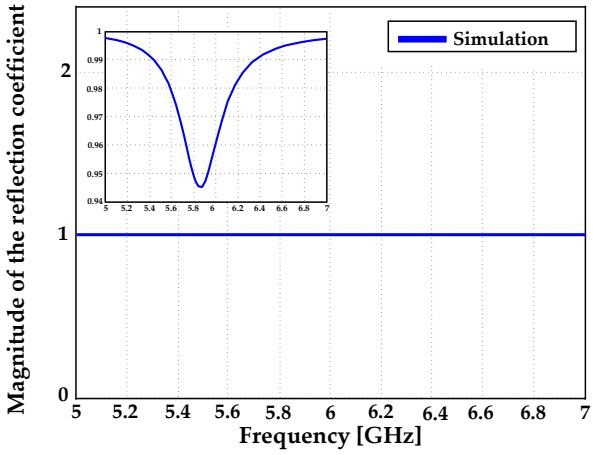


Figure 2.5: Magnitude of the reflection coefficient on the AMC surface.

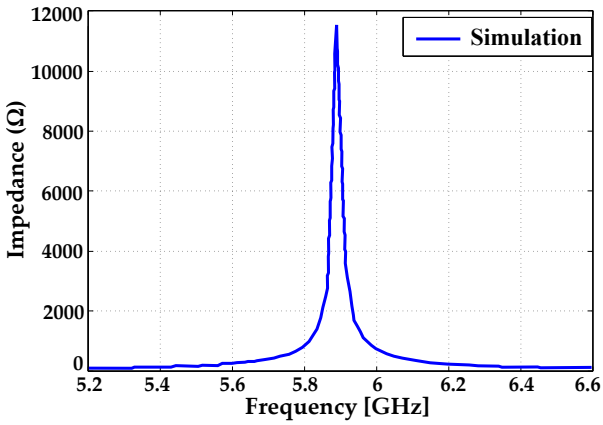


Figure 2.6: Simulated surface impedance of the AMC.

Next, the previously designed AMC unit-cell is rescaled to be used for European 868 MHz Ultra High Frequency (UHF) RFID and 2.48 GHz SHF RFID frequency bands using the MCT25, RO3010 and RO3003 dielectric substrates. The simulated reflection phase of the AMC structure using different dielectric substrates is presented in Figure 2.7.

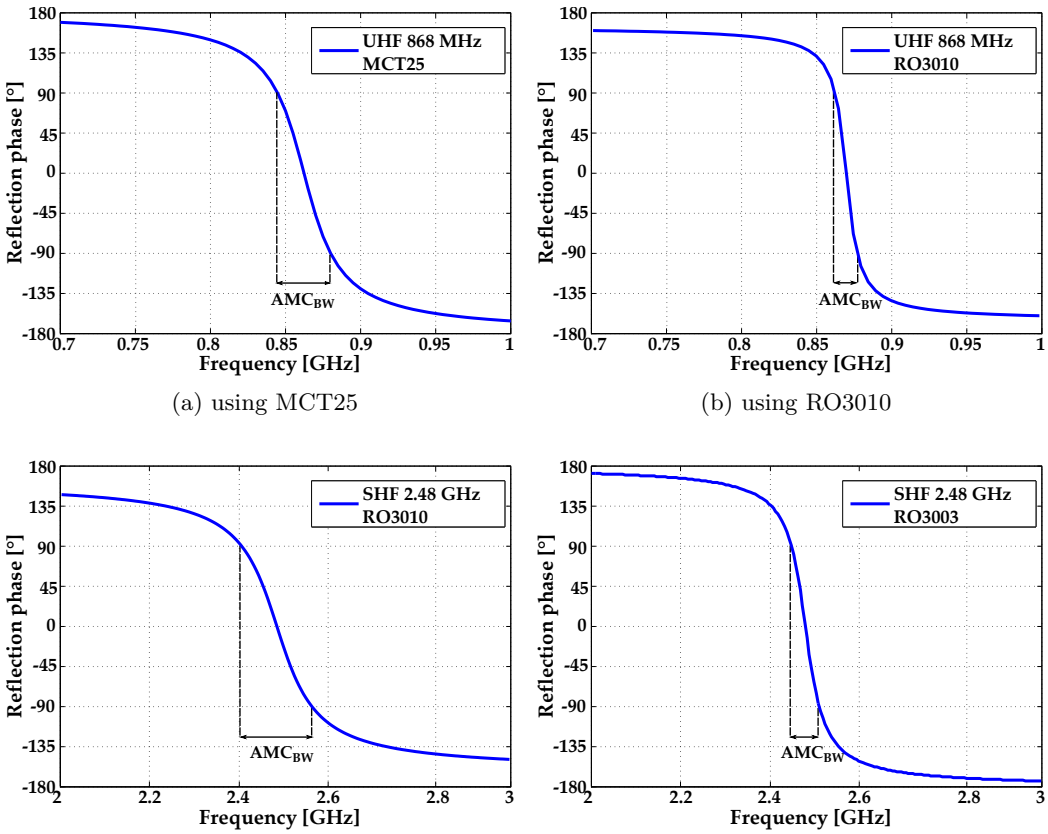


(a) using MCT25

(b) using RO3010

(c) using RO3010

(d) using R03003

Figure 2.7: Simulated reflection phase of the AMC structure using different dielectric substrates.

An adaptation of the AMC presented in the 5.8 GHz SHF RFID band is carried out substituting ARLON25N by RO4003C of the same thickness 0.762 mm (30 mils). As the only changes are the slightly higher substrate relative dielectric permittivity ($\varepsilon_r$= 3.38 for RO4003C compared to $\varepsilon_r$= 3.28 for ARLON25N) and loss tangent (tan $\delta$ = 0.0027 for RO4003C compared to tan $\delta$ = 0.0025 for ARLON25N), just a very small shift to a lower frequency is expected, together with a very slight reduction of the AMC operation bandwidth.

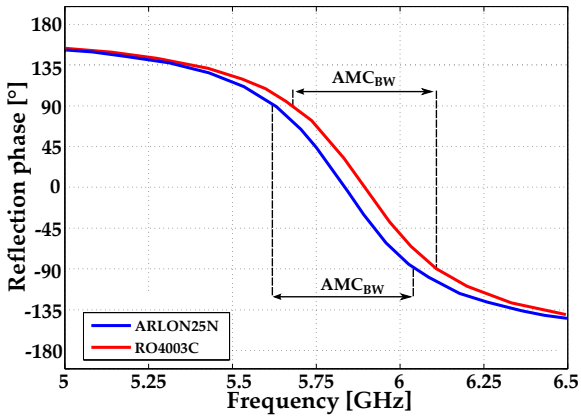


Figure 2.8: Reflection phase comparison for ARLON25N and RO4003C.

From Figure 2.8, it can be observed that the simulated AMC operation bandwidth is 433 MHz (7.3%) for ARLON25N and 420 MHz (7.2%) for RO4003C. In both cases, 5.8 GHz is inside the AMC operation bandwidth, which, as expected, is very similar for the two dielectric substrates.

| Unit-cell dimension [mm] | Reso. freq. [GHz] | Bandwidth [MHz / %] | Dielectric substrate | Dielectric thickness [mm] | Rel. perm. $\varepsilon_r$ |
|---|---|---|---|---|---|
| 23.4 ($\lambda_0$/15) | 0.868 | 35 / 4.0 | MCT25 | 2.54 ($\lambda_0$/136) | 25 |
| 49.2 ($\lambda_0$/7) | 0.868 | 15 / 1.7 | RO3010 | 1.27 ($\lambda_0$/272) | 10.2 |
| 16.93 ($\lambda_0$/7) | 2.48 | 130 / 5.2 | RO3010 | 1.27 ($\lambda_0$/95) | 10.2 |
| 31.2 ($\lambda_0$/3.9) | 2.48 | 65 / 2.6 | RO3003 | 0.762 ($\lambda_0$/159) | 3 |
| 11.52 ($\lambda_0$/4.5) | 5.89 | 433 / 7.3 | ARLON25N | 0.762 ($\lambda_0$/68) | 3.28 |
| 11.52 ($\lambda_0$/4.3) | 6.03 | 472 / 7.84 | RO3003 | 0.762 ($\lambda_0$/65) | 3 |
| 11.52 ($\lambda_0$/4.3) | 5.83 | 420 / 7.2 | RO4003C | 0.762 ($\lambda_0$/68) | 3.38 |

Table 2.1: Comparative study of the AMC unit-cell using different dielectric substrates (simulations).

From Table 2.1 it can be seen that for the same resonance frequency by increasing

the relative permittivity of the dielectric substrate, the dimension of the unit-cell decreases and the bandwidth of AMC operation also decreases. The thickness of the dielectric substrate has an important role in the bandwidth of the structure. The thicker the dielectric substrate, the wider the AMC bandwidth. Moreover, the AMC bandwidth decreases as the relative permittivity gets higher values.

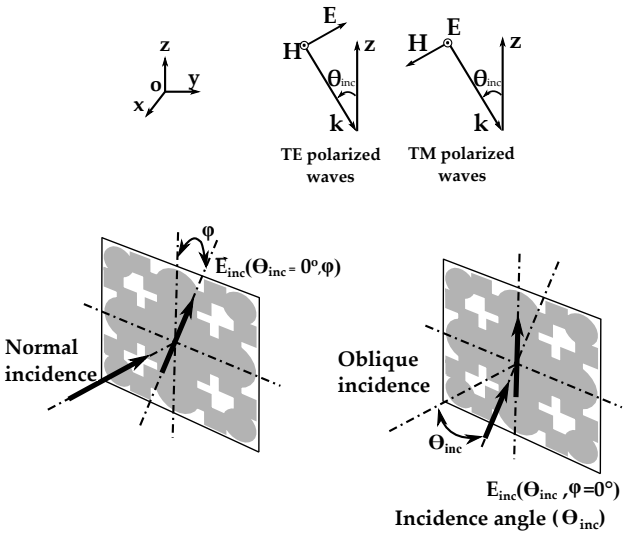


Figure 2.9: TE and TM polarized waves. Polarization and incidence angles variation schemes.

Furthermore, a study of the TE (Transverse Electric) and TM (Transverse Magnetic) polarized waves for different incident field polarization angles (assuming normal incidence) using ARLON25N dielectric substrate is presented. As the unit-cell is totally symmetric it will exhibit identical AMC performance (considering bandwidth and resonance frequency) for any polarization angles under normal incidence for TE and TM polarized waves. Figure 2.10 reveals the simulated reflection phase of the AMC structure for different incident field ($E_{\text{inc}}$) polarization angles ($\varphi$) assuming normal incidence.

The frequency domain solver is then used to apply incident waves at several incident angles in the range 0° - 55° for both TE and TM polarized waves and the resonance frequency is computed with the objective of determining the change in frequency and the deviation observed for the mentioned angular range.

In Figure 2.11, considering the TE polarized waves, the simulated reflection phase versus frequency of the unit-cell for oblique incident angles $\Theta_{\text{inc}}$ (polarization angle $\varphi = 0°$) is presented. Resonance conditions at 5.8 GHz are met as the incident angle $\Theta_{\text{inc}}$ increases from 0° and 55°. So, due to the symmetry of the unit-cell an

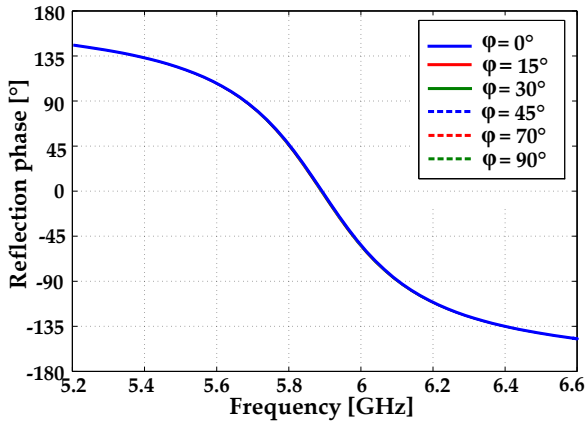


Figure 2.10: Simulated reflection phase of the AMC structure for different incident field ($E_{\text{inc}}$) polarization angles ($\varphi$).

angular margin of stability of ±55° is obtained. The AMC operational bandwidth decreases from 7.3% to 4.6% and the deviation of the resonance frequency is less than 1% as the incident angle increases to 55°. For incident angles greater than 55°, the resonance frequency shifts to another frequency band.

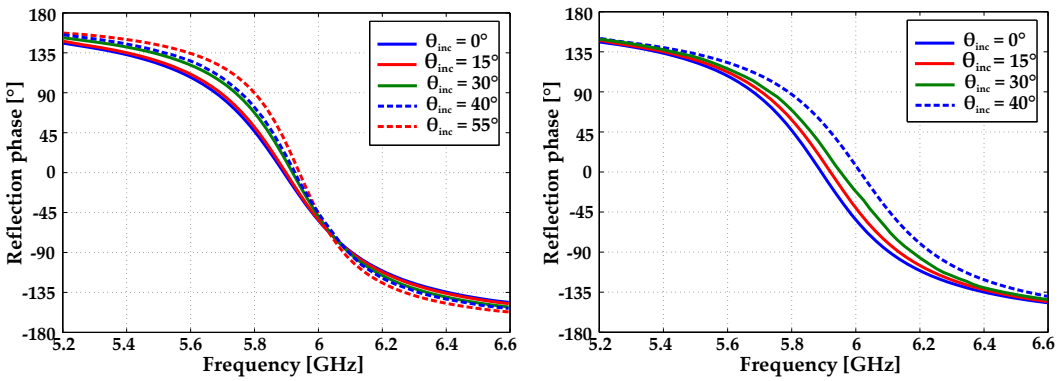


(a) TE polarized waves (b) TM polarized waves

Figure 2.11: Simulated reflection phase of the AMC structure for TE and TM polarized waves for different incident angles ($\Theta_{\text{inc}}$).

For TM polarized waves resonance conditions at 5.8 GHz are obtained only when the structure is illuminated with oblique incident angles up to 40°. As expected, the angular margin of stability reduces to ±40° due to the absence of via holes. In this case the AMC operational bandwidth is maintained and a deviation of 3.4% with respect to 5.8 GHz resonance frequency occurs. It is obvious that a considerable change in the reflection coefficient phase exists as the oblique incident angle gets

higher values, especially for TM polarized plane waves. The presented AMC design exhibits an angular margin of stability of ±40° for either TE and TM polarized waves which results in a highly stable AMC structure.

Owing to the merits of a single metal layer structure, compactness and good resonance stability performance with respect to different polarizations and incidence angles, the proposed 5.8 GHz AMC is promising in simulations and appropriate to practical applications.

#### 2.1.1.1 Flexible AMC Design

Flexible AMCs, as a part of flexible electronic circuits, may have a wide spectrum of applications in wireless communication but also they can be used in RFID tags over metallic objects [15], in RCS (Radar Cross Section) reduction [16, 17, 18] or combined with wearable antennas [19, 20, 21]. The last mentioned application allows humans to wear the combination antenna-AMC instead of carrying it. Thus, it is desirable to have AMCs adaptable (Figure 2.12) to the shape of the objects that will be used (AMC object-shape-adapted), the major concern being to obtain a flexible AMC structure (especially in the case of objects with curved surfaces) without loosing its functionality.

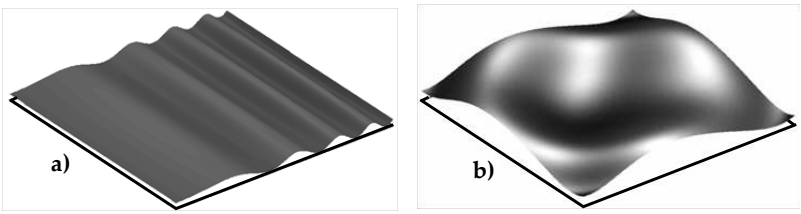


Figure 2.12: Possible bending patterns of a flexible AMC.

The same unit-cell as the one previously presented is used but with a different dielectric substrate, RO3003. The flexible RO3003 dielectric substrate compared to ARLON25N has the following characteristics: the same thickness ($h$ = 0.762 mm), a slightly lower relative dielectric permittivity ($\varepsilon_r$ = 3) and a lower loss tangent (tan $\delta$ = 0.0013). For the same unit-cell size ($W$ = 11.52 mm), a slight shift to a higher resonance frequency would be expected, due to the reduction in the relative dielectric permittivity value. If the resonance frequency is desired to be kept in the 5.8 GHz band (for example to be used for an RFID tag) using RO3003 with the aforementioned characteristics, the unit-cell size has to be slightly increased by using a 1.05 scale factor as shown in Figure 2.13.

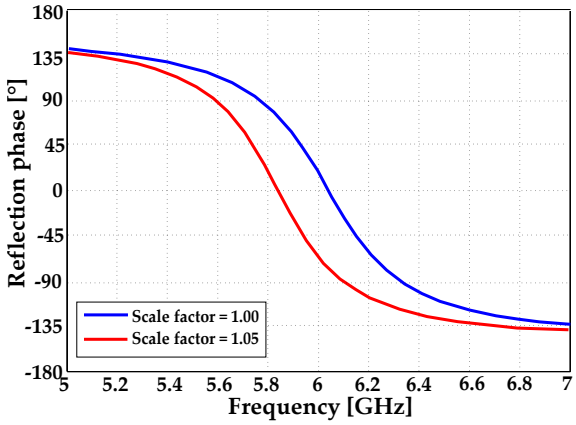


Figure 2.13: Reflection phase shifting versus scale factor of the unit-cell for the flat non-deformed RO3003 dielectric substrate.

### 2.1.2 Miniaturized Polarization Dependent AMC Design

In recent years miniaturization of microwave components and antennas has become increasingly important for applications where physical space is constrained [22]. Modern wireless communication terminals require small microwave elements, that are pertinent to high-level integration into compact light-weight systems. In this context, miniaturization of AMC structures is an important consideration for microwave engineers.

Traditionally, at microwave frequencies, the AMC structure has a unit-cell size of about half to quarter wavelength [1], making the overall AMC prohibitively large, if it is used as backing plane for antennas [23]. Designing AMC structures to operate at low frequencies is relatively challenging because in term of wavelength, the unit-cell can still be large.

Different methods are considered for the miniaturization of AMC structures. According to the first method, more electrical length is packed in fixed available space of the unit-cell in order to miniaturize the resonant elements [24]. Alternatively, another way to achieve miniaturization is the close coupling of two arrays in a double layer configuration, the size reduction being related to the thickness of the dielectric that separates the two layers. Moreover, to overcome size limitation, modified unit-cell geometries loaded with lumped capacitors have been discussed [25]. With this method the resonance frequency relies not only on the physical size of the periodic element but on the values of the lumped components. Another method used to obtain smaller unit-cells is to introduce a strong capacitive coupling, the element geometry selection being very important in order to maximize the coupling. As the

complexity of the fabrication process is reduced, the cost and the thickness of the resulting prototype are low, the last method is employed, therefore a miniaturized AMC using inter-digital capacitors and without via connections is presented in the following sections.

The starting point considering the metallization for the unit-cell design (henceforth referenced as AMC-1 unit-cell) consists of four rectangular metal pads placed on each corner of the unit-cell, four microstrip lines connecting each rectangle and in the middle of the unit-cell another microstrip line is placed perpendicularly. The four rectangular pads are responsible for the capacitive behavior (increasing the pad width, the resonance frequency and bandwidth decrease) whereas the other microstrip lines provide the inductive behavior (making the microstrip lines narrower the resonance frequency decreases and bandwidth increases). Moreover the gap between adjacent unit-cells introduces capacitive coupling and is a key factor for designing smaller unit-cells at lower frequency (decreasing the gap, the resonance frequency decreases and bandwidth becomes narrower). The central perpendicular narrow microstrip line is added in the geometry in order to enhance the unit-cell angular margin of stability for TE polarized waves. One could say that the central perpendicular narrow microstrip line confines the AMC operational bandwidth due to its parallel topology (for TE polarized waves) and a better solution would be to remove it. In that case, the angular margin of stability for TE polarized waves would decrease. Therefore, a compromise between the operational bandwidth and angular margin of stability has been taken.

With the purpose of minimizing the unit-cell size, a trade-off solution regarding the dielectric substrate relative permittivity $\varepsilon_r$ and thickness $h$ has to be adopted.

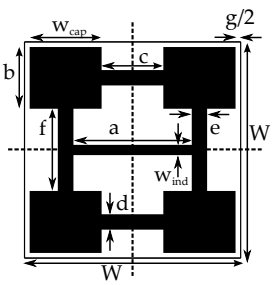


Figure 2.14: AMC-1 unit-cell geometry.

The AMC-1 unit-cell geometry which exhibits two symmetry planes is shown in Figure 2.14. For the unit-cell dimensions $W = \lambda_0/10 = 4.2$ mm ($\lambda_0$ is the free space wavelength, $\lambda_0$= 42 mm at 7.1 GHz) and dielectric substrate used R03010 ($\varepsilon_r$= 10.2, $h$ = 1.27 mm, metallization thickness = 18 µm and tan $\delta$ = 0.0023),

the simulated AMC-1 resonance frequency is 7.1 GHz and the bandwidth of the AMC-1 performance is 1.2 GHz (16.9%) (see Figure 2.15). The other geometrical parameters of the unit-cell are: $w_{\text{cap}} = 1.4$ mm, $a = 2.3$ mm, $b = c = 1.2$ mm, $d = e = 0.3$ mm, $f = 1.6$ mm, $g = 0.2$ mm and $w_{\text{ind}} = 0.2$ mm.

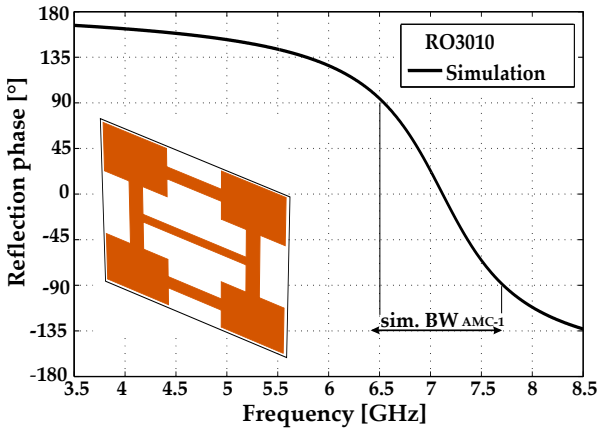


Figure 2.15: Simulated reflection phase of the AMC-1 design.

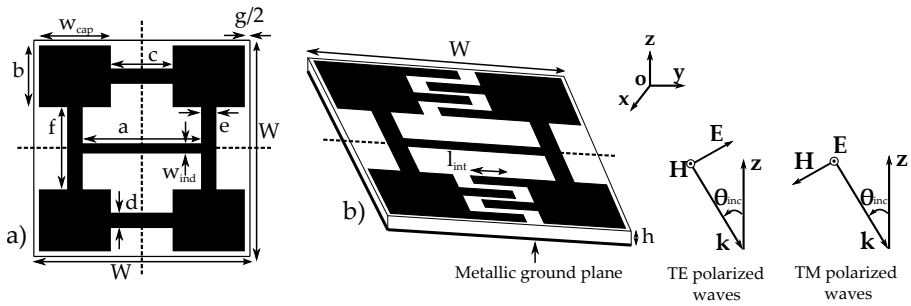


Figure 2.16: AMC-1 and AMC-2 unit-cell geometries.

The above presented AMC-1 unit-cell has been modified with the aim of decreasing the resonance frequency of the structure while maintaining the unit-cell dimension $W$ (design henceforth referenced as AMC-2 unit-cell) and using the same properties ($\varepsilon_r$ and $h$) of the dielectric substrate. Two of the thin inductive strip lines have been substituted by interdigital capacitors as illustrated in Figure 2.16. The new AMC-2 unit-cell will have a narrower bandwidth because of the strongly capacitive effect introduced by the interdigital capacitors (each unit-cell is strongly coupled with neighboring unit-cells), so the designer should ensure that the resulting bandwidth fulfills the application requirements (a trade-off solution between unit-cell size and bandwidth should be adopted considering the application). The AMC-2

unit-cell exhibits one symmetry plane.

From Figure 2.17 the simulation results show that by introducing interdigital capacitors, the operation bandwidth is 100 MHz (2.4%) and the resonance frequency decreases from 7.1 GHz to 4.15 GHz (42% decrease in frequency) keeping the parameter $W = 4.2$ mm of the unit-cell for RO3010 dielectric substrate.

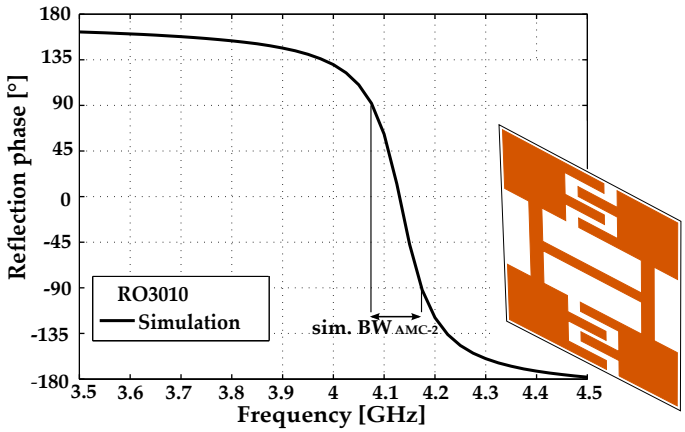


Figure 2.17: Reflection phase of the AMC-2 design using RO3010 dielectric substrate.

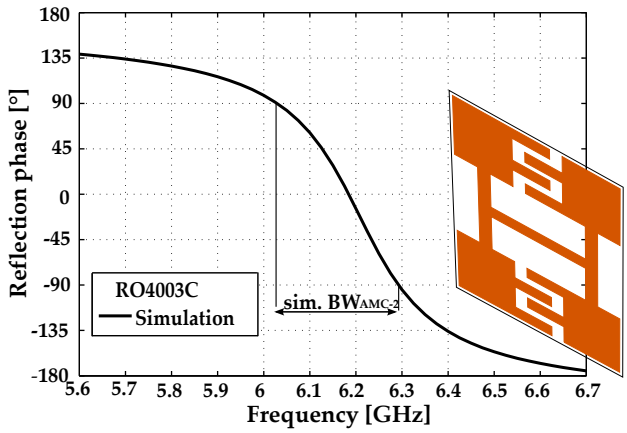


Figure 2.18: Reflection phase of the AMC-2 design using RO4003C dielectric substrate.

Another possibility to take into account is using RO4003C dielectric substrate. For RO4003C ($\varepsilon_r = 3.38$) of thickness $h = 1.524$ mm a resonance frequency of 6.2 GHz and 275 MHz (4.4%) AMC-2 unit-cell operation bandwidth is obtained (see Figure 2.18). As it is expected the simulated bandwidth of AMC-2 unit-cell decreases

to 2.4% for RO3010 and 4.4% for RO4003C, but it is still sufficient for the intended applications. At 6.2 GHz the structure presents high impedance (see Figure 2.19). In terms of wavelength the AMC-2 design has a dimension of $W = \lambda_0/17$ at 4.15 GHz using RO3010 dielectric substrate and $W = \lambda_0/12$ at 6.2 GHz using RO4003C dielectric substrate (see Table 2.2).

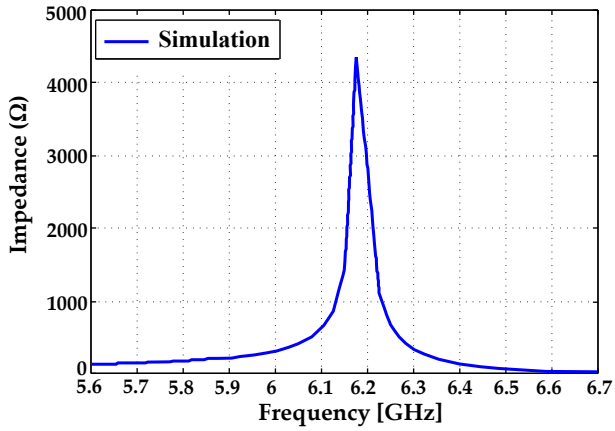


Figure 2.19: Simulated surface impedance of the AMC-2 design using RO4003C dielectric substrate.

| | AMC-1 | AMC-2 | AMC-2 |
|---|---|---|---|
| Unit-cell size [mm] | 4.2 ($\lambda_0/10$) | 4.2 ($\lambda_0/17$) | 4.2 ($\lambda_0/12$) |
| Dielectric substrate | RO3010 | RO3010 | RO4003C |
| Relative permittivity $\varepsilon_r$ | 10.2 | 10.2 | 3.38 |
| Dielectric thickness [mm] | 1.27 ($\lambda_0/33$) | 1.27 ($\lambda_0/57$) | 1.52 ($\lambda_0/32$) |
| Reso. freq [GHz] * | 7.10 | 4.15 | 6.20 |
| Bandwidth [MHz/%] | 1200/16.9 | 100/2.4 | 275/4.4 |
| Ang. Stab [°] ** | 75 | 75 | 65 |
| * Computed for normal incidence and 0° polarization angle<br>** Angular margin of stability computed for different incident angles assuming 0° polarization angle | | | |

Table 2.2: Analysis of presented miniaturized unit-cells (simulations).

Next, a comparative study in terms of dimensions and operational bandwidth of the presented AMC-2 unit-cell and and the most well known unit-cells from the literature will be conducted.

In Table 2.3 a comparison between the dimension of different unit-cells working

in 2.45 GHz frequency band and using RO TMM6 dielectric substrate ($\varepsilon_r = 6$ and thickness $h = 2.54$ mm) is performed. The dimension of the UC-EBG unit-cell [5] is 21 mm, for the first-order Peano curve the unit-cell [5] dimension is 20.5 mm, whereas for the presented AMC-2 design the dimension is 8.5 mm, which is approximately 2.4 times smaller. Compared to the second-order Hilbert curve unit-cell [5], the AMC-2 unit-cell has a reduction of 34% in size. The measured bandwidths of the unit-cells referenced in [5] are similar with the simulated bandwidth of the AMC-2 unit-cell for RO TMM6 dielectric substrate, so miniaturization is obtained without loosing operational bandwidth.

| Ref. | Unit-cell size [mm] | Reso. freq. [GHz] | | Bandwidth [%] | |
|---|---|---|---|---|---|
| | | Sim. | Mea. | Sim. | Mea. |
| [5] | 19.2 ($\lambda_0/6.4$) | 2.45 | 2.52 | 12 | 3.46 |
| | 21 ($\lambda_0/5.8$) | 2.45 | 2.45 | 4.88 | 2.95 |
| | 20.5 ($\lambda_0/6$) | 2.45 | 2.51 | 6.30 | 3.14 |
| | 12.9 ($\lambda_0/9.5$) | 2.45 | 2.51 | 4.69 | 1.93 |
| AMC-2 | 8.5 ($\lambda_0/14.4$) | 2.45 | - | 2.85 | - |

Table 2.3: Unit-cell size comparison for 2.45 GHz and RO TMM6 dielectric substrate ($\varepsilon_r = 6$, dielectric thickness $h = 2.54$ mm).

For the RO3010 dielectric substrate as it can be seen from Table 2.4, the split ring resonator unit-cell [26] has a size of 10 mm, which is more than twice the dimension of the AMC-2 for resonance frequency around 4 GHz. Furthermore, for similar bandwidths, the dimension of the novel AMC-2 design is smaller ($\lambda_0/17$ compared to $\lambda_0/15$ of [6] and $\lambda_0/11.4$ of [27]).

| Ref. | Unit-cell size [mm] | Dielectric thickness [mm] | Reso. freq. [GHz] | | Bandwidth [%] | |
|---|---|---|---|---|---|---|
| | | | Sim. | Mea. | Sim. | Mea. |
| [26] | 10 ($\lambda_0/7.5$) | 1.27 ($\lambda_0/59$) | 4 | - | 6.5 | - |
| [6] | 8.3 ($\lambda_0/15$) | 1.27 ($\lambda_0/98$) | 2.4 | 2.47 | 4.5 | 2.5 |
| [27] | 11 ($\lambda_0/11.4$) | 1.27 ($\lambda_0/98$) | 2.4 | - | 1.6 | - |
| AMC-2 | 4.2 ($\lambda_0/17$) | 1.27 ($\lambda_0/57$) | 4.15 | 4.25 | 2.4 | 1.6 |
| square | 9.45 ($\lambda_0/7.6$) | 1.27 ($\lambda_0/57$) | 4.15 | - | 10.5 | - |

Table 2.4: Unit-cell size comparison for RO3010 dielectric substrate ($\varepsilon_r = 10.2$, dielectric thickness $h = 1.27$ mm).

For $\varepsilon_r = 2.2$ and $h = 1$ mm, the novel design AMC-2 presents a miniaturization of

about 37% compared to the size of the double spiral unit-cell from [28], respectively a 4.5 times reduction compared to the dipole array design from [7] (see Table 2.5). Last but not least, from Table 2.6, the novel design AMC-2 presents similar bandwidths and the unit-cell is more than twice smaller than [29].

| Ref. | Unit-cell size [mm] | Dielectric thickness [mm] | Reso. freq. [GHz] | | Bandwidth [%] | |
|---|---|---|---|---|---|---|
| | | | Sim. | Mea. | Sim. | Mea. |
| [1] | 7.5 ($\lambda_0/3.3$) | 1 ($\lambda_0/25$) | 12 | - | 9.7 | - |
| [28] | 3.75 ($\lambda_0/6.1$) | 1 ($\lambda_0/23$) | 13.1 | - | 9.16 | - |
| [7] | 10.6 ($\lambda_0/2.2$) | 1.1 ($\lambda_0/21$) | 12.6 | - | 8.4 | - |
| AMC-2 | 2.35 ($\lambda_0/10$) | 1 ($\lambda_0/23.5$) | 12.65 | - | 7.1 | - |

Table 2.5: Unit-cell size comparison for $\varepsilon_r = 2.2$, dielectric thickness $h = 1$ mm.

| Ref. | Unit-cell size [mm] | Dielectric thickness [mm] | Reso. freq. [GHz] | | Bandwidth [%] | |
|---|---|---|---|---|---|---|
| | | | Sim. | Mea. | Sim. | Mea. |
| [29] | 26.25 ($\lambda_0/7.2$) | 5.08 ($\lambda_0/37$) | 1.575 | - | 4.2 | - |
| | 21 ($\lambda_0/10.6$) | 7.5 ($\lambda_0/30$) | 1.344 | - | 6.3 | - |
| | 21 ($\lambda_0/20$) | 13 ($\lambda_0/32$) | 0.712 | - | 7.1 | - |
| AMC-2 | 8.4 ($\lambda_0/22.6$) | 5.08 ($\lambda_0/37$) | 1.575 | - | 3.7* | - |
| | 8.6 ($\lambda_0/26$) | 7.5 ($\lambda_0/30$) | 1.575 | - | 6.1* | - |
| | 17.4 ($\lambda_0/23.6$) | 13 ($\lambda_0/30$) | 1.575 | - | 5* | - |
| * ±45°bandwidth criteria | | | | | | |

Table 2.6: Unit-cell size comparison between [29] and AMC-2 design for $\varepsilon_r = 13$.

Furthermore a study of the TE (Transverse Electric) and TM (Transverse Magnetic) polarized waves for different incident field ($E_{\text{inc}}$) polarization angles ($\varphi$) of the miniaturized AMC-2 unit-cell (assuming normal incidence, $\Theta_{\text{inc}} = 0°$) using RO4003C dielectric substrate is presented (see Figure 2.16(b)). Since the unit-cell is not symmetric, the AMC-2 structure is not dual-polarized at the same frequency.

The unit-cell has only one plane of symmetry so it will behave the same (considering bandwidth and resonance frequency) only for 0° and 180° polarization angles under normal incidence for TE polarized waves (according the symmetry axes indicated in Figure 2.16(b)). Taking into account the unit-cell geometry, if the polarization angle is varied from 0° to 45° and from 135° to 180° a deviation of 1% with respect to 6.2 GHz resonance frequency occurs whereas the AMC-2 operational bandwidth decreases from 4.4% to 2% (see Figure 2.20). Outside the previously men-

tioned angular intervals, the resonance frequency for the TE polarized waves shifts to 8.5 GHz.

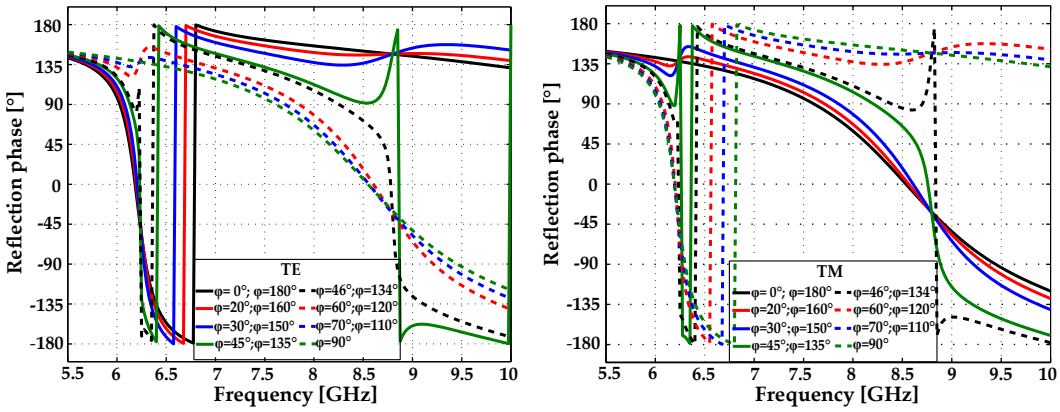


(a) TE polarized waves (b) TM polarized waves

Figure 2.20: Simulated reflection phase of the AMC-2 for different incident field ($E_{\text{inc}}$) polarization angles ($\varphi$) for TE/TM polarized waves under normal incidence.

For the TM polarized waves the resonance frequency of the AMC-2 is shifted to 8.5 GHz and operates identically (considering bandwidth and resonance frequency) for 0° and 180° polarization angles assuming normal incidence. When the structure is illuminated with incident plane wave with polarization angles up to 45° and from 135° to 180°, resonance conditions at 8.5 GHz are met. The operational bandwidth decreases from 22% to 10% as the polarization angle increases to 45°. For polarization angles between 46° and 134°, the AMC-2 resonates at 6.2 GHz.

In Figure 2.21 the simulated reflection phase of the unit-cell for different oblique incident angles reveals an angular margin of stability of 65° for TE polarized waves at 6.2 GHz under a polarization angle of 0° and behaves as an artificial magnetic conductor for frequencies between 7.9 GHz and 9.4 GHz for TM polarized waves.

A similar analysis for a polarization angle of 45° (since the structure is stable from 0° up to 45° and from 135° to 180° polarization angle) renders an angular margin of stability of 50° for TE polarized waves and behaves as an artificial magnetic conductor for frequencies between 8.2 GHz and 8.7 GHz for TM polarized waves (see Figure 2.22).

The running time of the electromagnetic simulations for both normal and oblique incidence is an important issue that has to be taken into consideration when designing AMC structures.

All the simulation were carried out using a PC with Intel i7-2640M CPU (2 cores with 4 threads) and 8 GB RAM. The CPU frequency is 2.8 GHz. A frequency

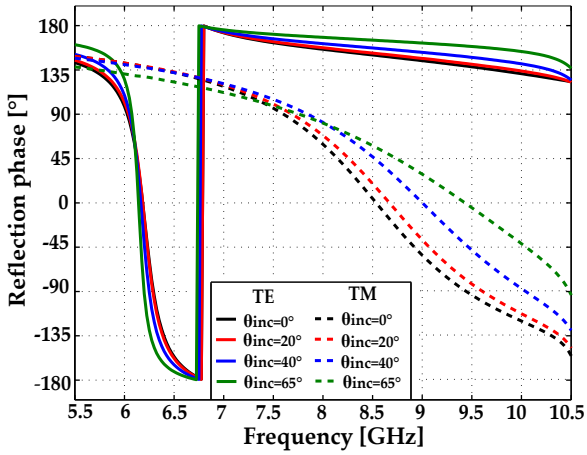


Figure 2.21: Simulated reflection phase of the AMC-2 for different oblique incident angles ($\Theta_{\text{inc}}$) for both TE/TM polarized waves under 0° polarization angle.

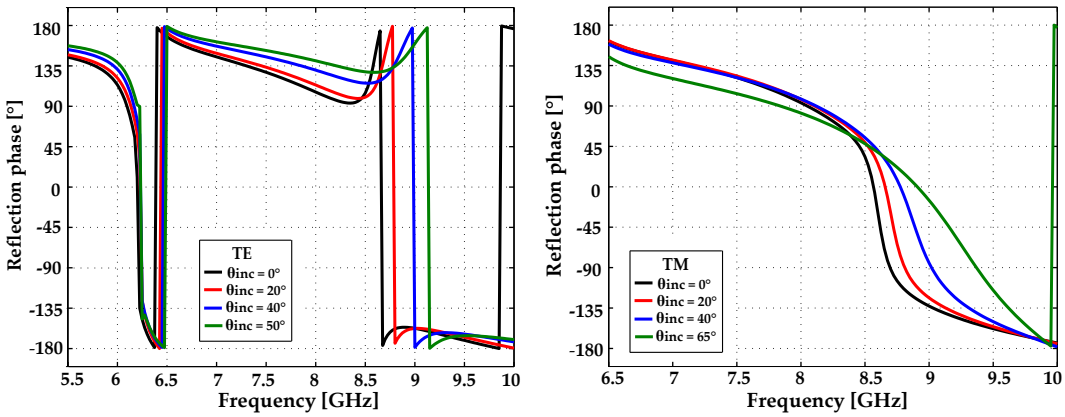


(a) TE polarized waves

(b) TM polarized waves

Figure 2.22: Simulated reflection phase of the AMC structure for different oblique incident angles ($\Theta_{\text{inc}}$) and 45° polarization angle for TE/TM polarized waves.

sweep is carried between 5 GHz and 11 GHz with a step of 0.025 GHz, meaning 240 points. For normal incidence the computational time is 30 minutes whereas for oblique incidence the computational time for each variation of the incident angle is also 30 minutes.

One of the applications of AMCs is the possibility to be used as planar antenna ground plane [23],[30] for which the AMC-2 angular margin of stability is a major concern. Thus, depending on the fields radiated by the antenna, the radiation properties can be enhanced in either 6.2 GHz or 8.5 GHz frequency band.

For example, as the fundamental mode of a rectangular patch antenna is a TM mode, under normal incidence the AMC-2 combined with the patch antenna will radiate properly at 6.2 GHz only when the polarization angle is varied from 46° to 134° (according to Figure 2.20b). However the presented AMC-2 could be combined with a patch antenna operating at any frequency included in the 7.9 GHz to 9.4 GHz band (see Figure 2.21).

#### 2.1.2.1 Miniaturized Polarization Insensitive AMC Design

As shown in Figure 2.20 obvious differences exist between the phase response of the reflection coefficient under TE and TM polarized plane waves. In order to eliminate the polarization dependence of the presented AMC the later technique is followed: based on the original unit-cell a new 2 by 2 unit-cell is created.

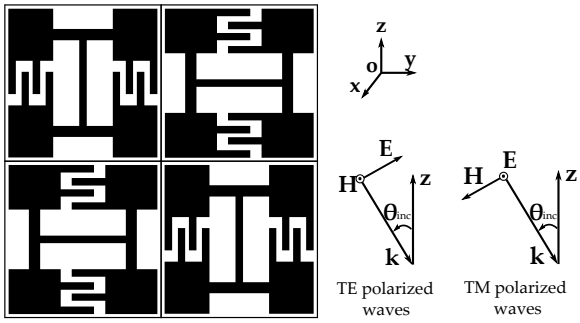


Figure 2.23: AMC unit-cell formed by 2x2 AMC-2 unit-cells.

One diagonal contains the original elements whereas the other diagonal elements in this new 2 by 2 unit-cell are clockwise rotated 90° (see Figure 2.23) such that the reflection coefficient phase becomes identical for TE and TM polarized waves. In this manner, these structures may have multiple resonances, independent on the wave polarization [31, 32].

The phase of the reflection coefficient for the new periodic structure of infinite extent, for both TE and TM polarized plane waves is shown in Figure 2.24. As it

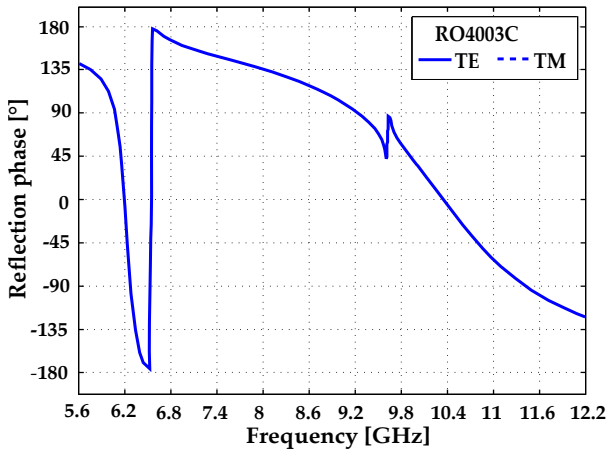


Figure 2.24: Simulated reflection phase of the polarization insensitive AMC structure for normal incidence and 0° polarization angle.

can be seen, the phase is completely independent of the wave polarization. The 6.2 GHz resonance frequency occur no matter what polarization is used to excite the structure. However, instead of 8.5 GHz the second resonance frequency shifts to 10.4 GHz.

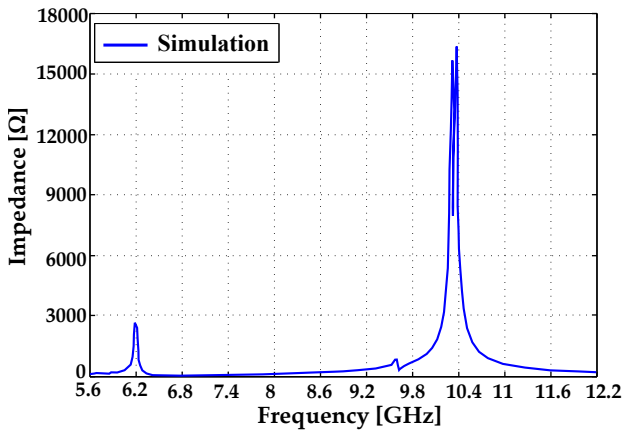


Figure 2.25: Simulated surface impedance of the polarization insensitive AMC structure for normal incidence and 0° polarization angle.

Moreover, the surface impedance of the infinite periodic structure presented in Figure 2.25 renders high values at 8.5 GHz resonance frequency and 10.4 GHz resonance frequency. The high impedance resonant condition leads to a reflection phase that passes through 0°.

The overall size of the new AMC structure is obviously now larger with respect

to the resonant wavelengths, twice the size of the initial structure, however since the individual unit-cells are electrically small, the increase in size may be considered acceptable, depending upon the application considered.

The new AMC is polarization independent not only for 0° polarization angle but also for any angle under normal incidence, the curve of the reflection coefficient phase presenting the same shape (see Figure 2.26).

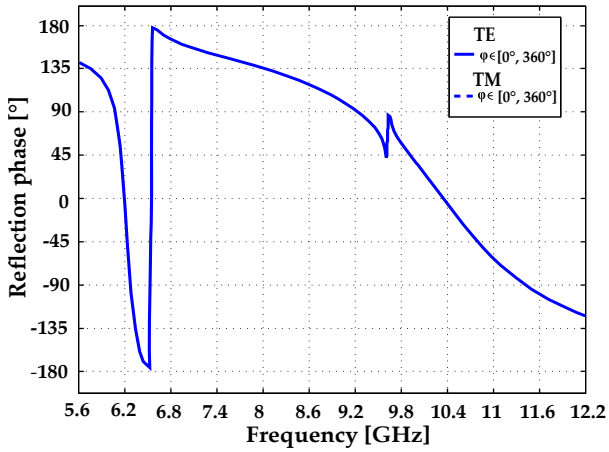


Figure 2.26: Simulated reflection phase of the polarization insensitive AMC structure for different incident field ($E_{\text{inc}}$) polarization angles ($\varphi$) for both TE and TM polarized waves under normal incidence.

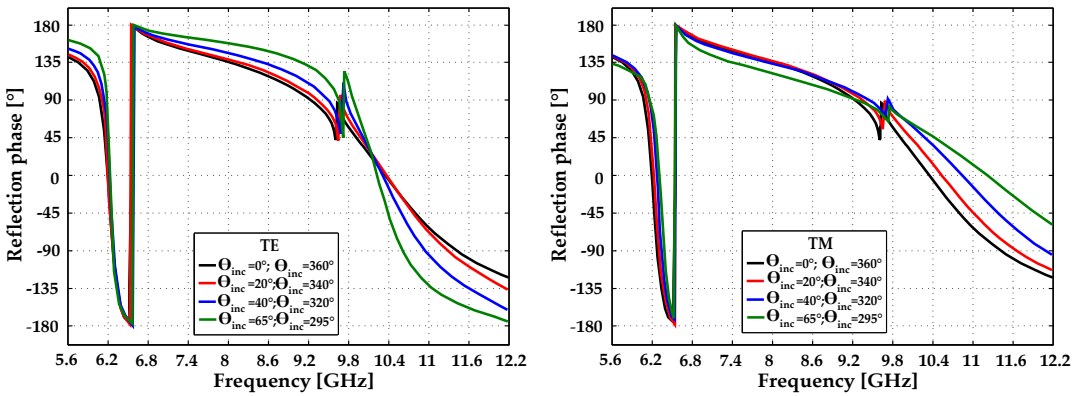


(a) TE polarized waves

(b) TM polarized waves

Figure 2.27: Simulated reflection phase of the polarization insensitive AMC structure for different oblique incident angles ($\Theta_{\text{inc}}$) for both TE and TM polarized waves under 0° polarization angle.

To study the angular margin of stability, the reflection coefficient phase versus

frequency for incident angles $\Theta_{\text{inc}}$ swept between 0° and 65° has been simulated (for both TE and TM polarized waves) and presented in Figure 2.27. Considering the TE polarized waves, the operational bandwidth decreases from 22% to 10% as the incident angle increases to 65° for the upper frequency band. A counter performance is found for the TM polarized waves. By progressively incrementing the incident angle, the operational bandwidth raises from 22% to 33%. For the lower frequency band, the resonance frequency (6.2 GHz) and the operational bandwidth (4.4%) is kept practically the same regardless the incident angle.

## 2.2 Characterization and Measurement Results in Anechoic Chamber

The TSC-UNIOVI spherical range anechoic chamber (8 m x 5 m x 4.5 m) was designed to operate from hundred of megahertzs up to 40 GHz. The upper frequency is limited by the operating frequency of the vector network analyzer (VNA), signal amplifiers, and RF cables while the lower frequency limit is due to the size of the pyramidal absorbers. The roof, walls and floor of the anechoic chamber are covered by pyramidal absorbers whereas positioners and antenna supporting structures are covered by flat radiation absorbing material. In general, when antennas are measured, two antenna positioners which are found inside the anechoic chamber are used: one for positioning the antenna under test (AUT) and the other one for positioning the probe antenna.

In order to measure the reflection coefficient phase of an AMC two horn probe antennas working in the same frequency band as the AMC are required: a receiving horn antenna (Rx) to measure the field scattered of the periodic structure and a transmitting horn antenna (Tx) for radiating the incident field onto the AMC structure (see Figure 2.28). The receiving horn antenna is placed at the probe antenna's position whereas the transmitting horn antenna is placed next to the receiving horn antenna, using a portable tripod. In order to reduce the mutual coupling between the transmitting and receiving horn antennas, a minimum distance between them is kept.

The object under test, in this case the AMC, is placed at the AUT positioner. The dimension $D$ of the AMC prototype is known. In order to ensure that the scattered field is acquired in the far-field region, the far-field distance is estimated being $RFF = 2D^2/\lambda_0$ [33]. For measuring the AMC structure in far field conditions, the separation between each horn antenna and AMC should be greater than the far field distance. To calculate the reflection coefficient of the AMC structure, a flat metallic plate (PEC) is used as reference for normalization of the measured reflection

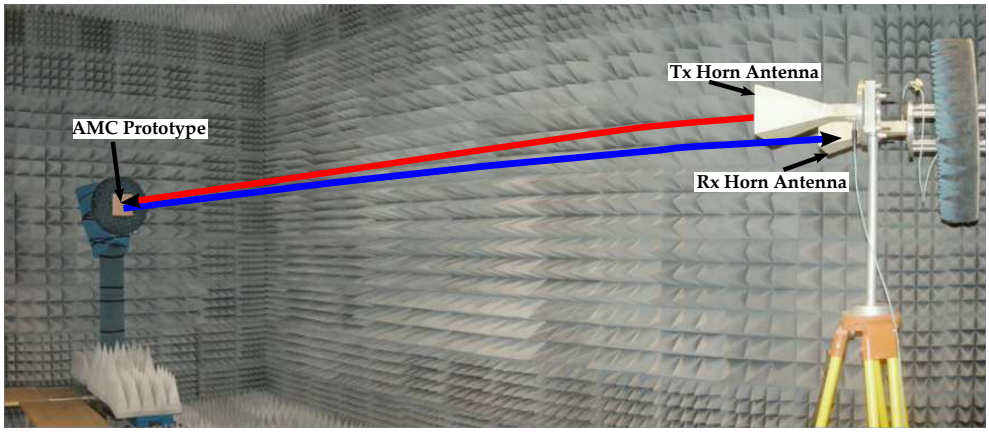


Figure 2.28: Reflection coefficient measurement setup in anechoic chamber.

coefficient of the AMC [2].

In order to manufacture all the prototypes, the LPKF Proto Laser-S machine is used (Figure 2.29). The laser micro-machining has a very high precision (the laser beam diameter is 25 µm). Lines as low as 50 µm (depending on the substrate used) in width can be fabricated, while slots/apertures as low as 25 µm in width can be etched.

Figure 2.29: LPKF Proto Laser-S machine.

### 2.2.1 Characterization of the AMC Employing Rigid Substrate

An AMC prototype of 12 x 12 unit-cells using ARLON25N dielectric substrate has been manufactured (Figure 2.30) and the prototype is characterized in terms of its reflection coefficient phase.

The separation between each horn antenna working in the 5 - 7 GHz and the object-under-test is 5 m. The object-under-test size is $D$ = 13.82 cm. Taking into account the upper limit of the frequency band (7 GHz, $\lambda_0$= 4.28 cm) and the object-under-test size ($D$ = 13.82 cm), the far field distance is $RFF$ = 0.89 m. Thus, the prototype has been measured in far field conditions.

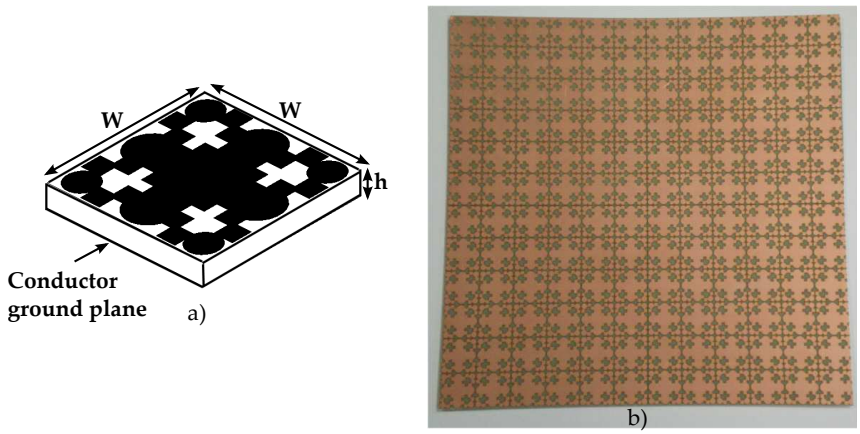


Figure 2.30: Unit-cell geometry. a) side view, b) planar AMC manufactured prototype.

#### 2.2.1.1 Reflection Phase Measurement for AMC Band Determination

The measured reflection phase for the AMC prototype is represented in Figure 2.31 together with the simulation results. The manufactured prototype has the resonance frequency at 5.72 GHz which means a 2.8% deviation with respect to the simulation (5.89 GHz). The AMC operation bandwidth is 440 MHz, in good agreement with the simulated value. The slight frequency shift between the measured AMC resonance frequency and simulated value is typically due to the variation of relative dielectric permittivity $\varepsilon_r$ with respect to its nominal value used in the simulations and to the manufacturing process tolerances as justified in [34]. Compared to [35] which uses the same dielectric substrate, the presented AMC design has a bandwidth of operation three times broader.

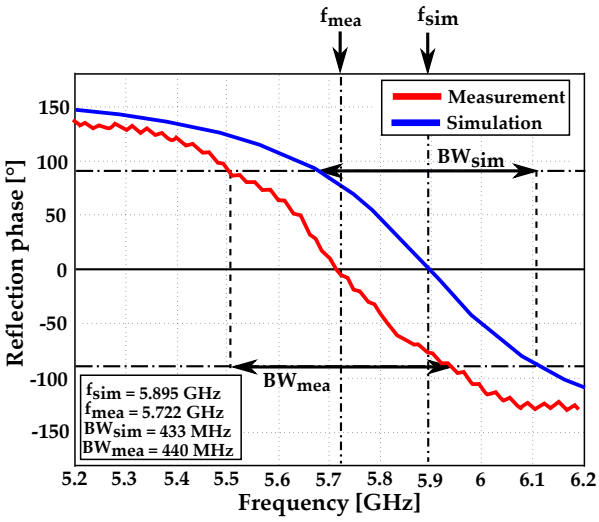


Figure 2.31: Reflection phase of the simulated and manufactured AMC prototype.

#### 2.2.1.2 Reflection Phase Characterization for Different Field Polarization Angles

The reflection phase of the manufactured AMC structure has been measured for different incident field ($E_{\text{inc}}$) polarization angles ($\varphi$). The structure is illuminated with incident plane wave and resonance conditions are met for any polarization angle ($\varphi$) of the incident field (assuming normal incidence), as shown in Figure 2.32. As expected the structure exhibits identical AMC performance for all the polarization angles.

#### 2.2.1.3 Reflection Phase Characterization for Different Incident Angles

The angular margin of stability under oblique incidence for the AMC structure has also been analyzed. For the 13.82 x 13.82 cm$^2$ manufactured prototype, it was obtained an angular margin of stability $\Theta_{\text{inc}}= \pm 8.5°$ (see Figure 2.33), the resonance frequency being in the 5.5 GHz - 5.95 GHz band.

The discrepancy between the simulated and measured angular margin of stability can be attributed to the small and finite size of the manufactured prototype, which leads to some nulls in the scattered field amplitude, depending on the incident angle and the distance between the prototype and horn probe antennas. The nulls appear due to the diffraction of the excited wave incident on the edges of the prototype. The same happens when characterizing a finite-size PEC following the same procedure.

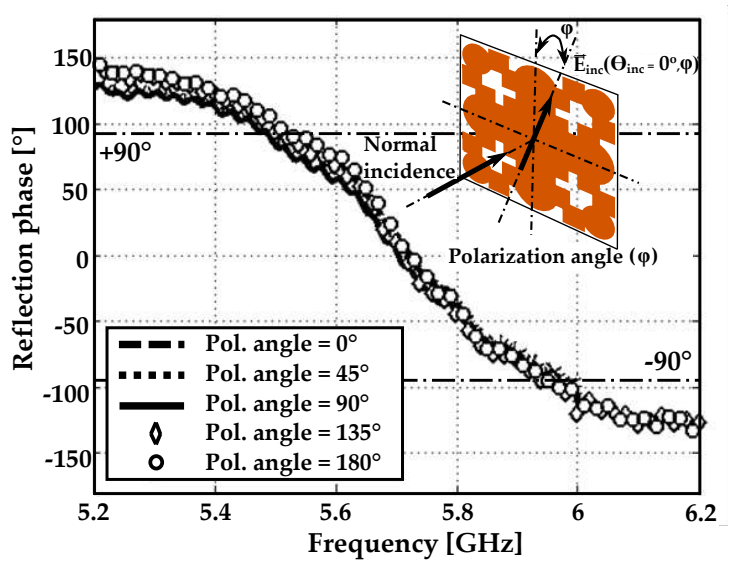


Figure 2.32: Reflection phase of the manufactured AMC prototype for different incident field ($E_{\text{inc}}$) polarization angles ($\varphi$).

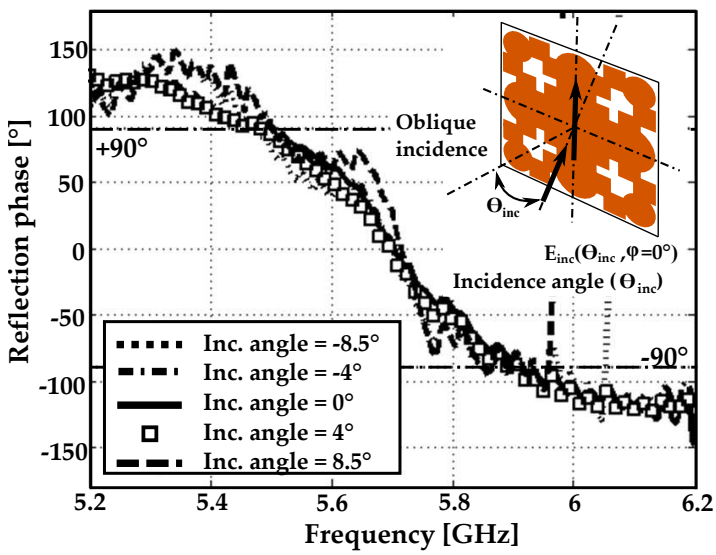


Figure 2.33: Reflection phase of the manufactured AMC prototype for different incident angles ($\Theta_{\text{inc}}$).

### 2.2.2 Characterization of the AMC Employing Flexible Substrate

Neither the methodology nor the measurement setup in the anechoic chamber is changed with respect to the characterization of the AMC implemented on a rigid dielectric substrate. In the case of the flexible AMC even if the measurement distance is different due to the bending depth $h$ of the flexible AMC structure (compared to the non-deformed AMC) it can be considered negligible with respect to the distance of 5 m between the object-under-test and the probe horn antennas. Measurements of the flat (i.e., not bent) AMC prototype have been firstly carried out. Then, the prototype has been bent (see Figure 2.34) and measured (Figure 2.35).

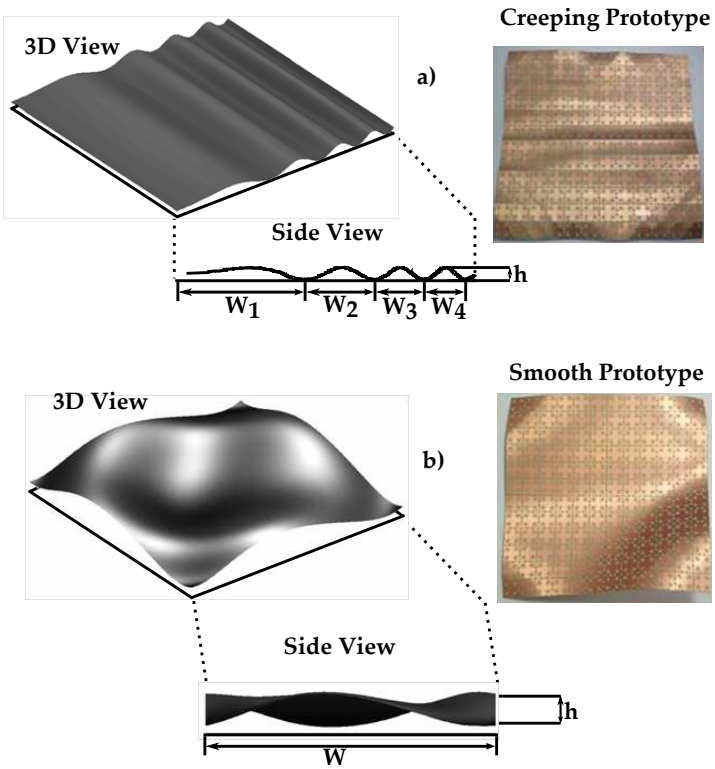


Figure 2.34: Bending patterns. (a) Creeping prototype with $W_1$ = 56.6 mm, $W_2$ = 30.0 mm, $W_3$ = 21.5 mm, $W_4$ = 18.3 mm and $h$ = 5mm, (b) smooth prototype with $W$ = 120 mm, and $h$ = 10 mm.

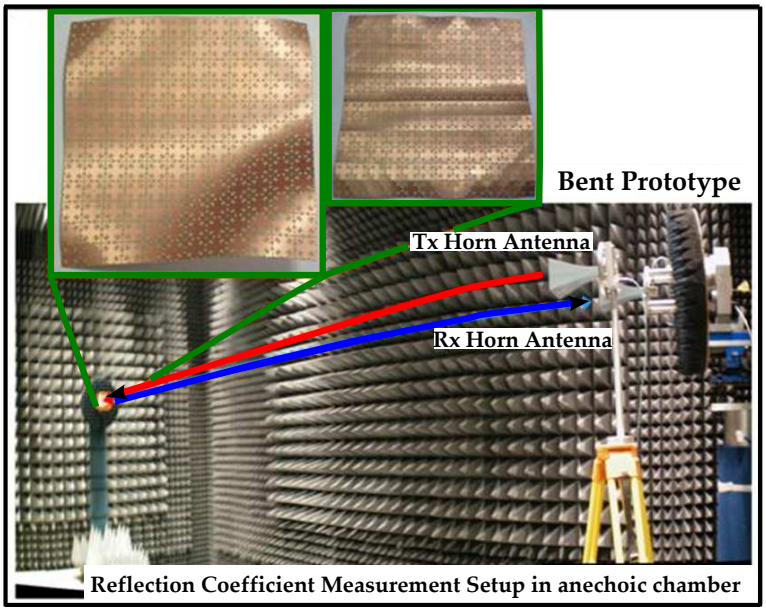


Figure 2.35: Reflection coefficient measurement setup in anechoic chamber.

#### 2.2.2.1 Reflection Phase Measurement for AMC Band Determination

Since the AMC is expected to be bent or conformed during operation, flexibility tests are conducted. A flexible AMC can be bent in many arbitrary ways. Between the multiple possible ways of bending, two typical different possibilities have been selected and tested (see Figure 2.34): a "creeping" pattern (henceforth referred as creeping prototype) which can be caused in textile AMC integrated in the garment when the arm is bent at the elbow and a "smooth" pattern (henceforth referred as smooth prototype) which can be caused in the shoulder or in the torso. The ratio between the minimum bending radius of curvature and the AMC size is 0.43 for the creeping prototype and 0.86 for the smooth prototype. This minimum bending radius of curvature corresponds to $0.1\lambda_0$ for the creeping prototype and $0.21\lambda_0$ for the smooth prototype.

Figure 2.36 renders the measured reflection phase of the bent and flat manufactured prototypes together with the simulation results of the flat AMC structure under normal incidence conditions. The resonance frequency and bandwidth are evaluated since the bent AMC is prone to frequency shift. The flat prototype has the resonance frequency at 6.23 GHz which means a deviation of 3.3% with respect to 6.03 GHz resonance frequency obtained in simulations. The reason of the frequency shift between the measured AMC resonance frequency and simulated value is typically attributable to the manufacturing process tolerances as justified in [34].

Considering the manufactured creeping bent prototype, there is no frequency shift between its behavior and the flat prototype. However, the smooth bent prototype has the resonance frequency at 6.27 GHz, which means a 0.6% shift in frequency with respect to the flat prototype. The bandwidth of AMC performance for the flat prototype is 392 MHz (6.29%) in good agreement with the simulated value (7.84%) (see Figure 2.36). The creeping bent prototype has an AMC operation bandwidth of 387 MHz (6.19%) whereas the AMC operation bandwidth of the smooth bent prototype is 416 MHz (6.63%), even slightly wider than the operation bandwidth of the flat prototype.

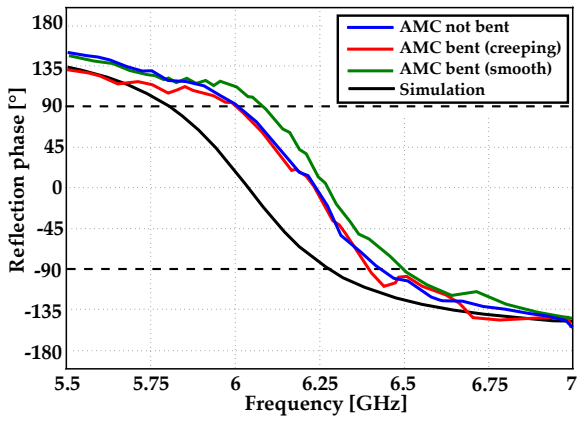


Figure 2.36: Reflection phase of the flat (simulation and measurement) and bent (measurements) prototypes.

| Prototype | Measured resonance frequency | Measured bandwidth [MHz / %] | Frequency deviation with respect to flat [%] |
|---|---|---|---|
| Flat | 6.23 | 392 / 6.29 | 0 |
| Creeping | 6.23 | 387 / 6.19 | 0 |
| Smooth | 6.27 | 416 / 6.63 | 0.6 |

Table 2.7: Prototypes' comparison

As the smooth prototype presents a variation in the AMC operation bandwidth and a slight shift in frequency with respect to the flat prototype, the influence of the incident field ($E_{inc}$) polarization angle ($\varphi$) and the angular margin of stability under oblique incidence ($\Theta_{inc}$) has been analyzed for this prototype taking advantage of the measurement setup capabilities.

#### 2.2.2.2 Reflection Phase Characterization for Different Field Polarization Angles

The reflection phase of the manufactured AMC prototypes has been measured for different incident field ($E_{\text{inc}}$) polarization angles ($\varphi$). The unit-cell design symmetry makes possible the AMC to operate identically for any polarization of the incident field (assuming normal incidence) for the flat prototype. The same behavior is found for the smooth bent prototype, as shown in Figure 2.37.

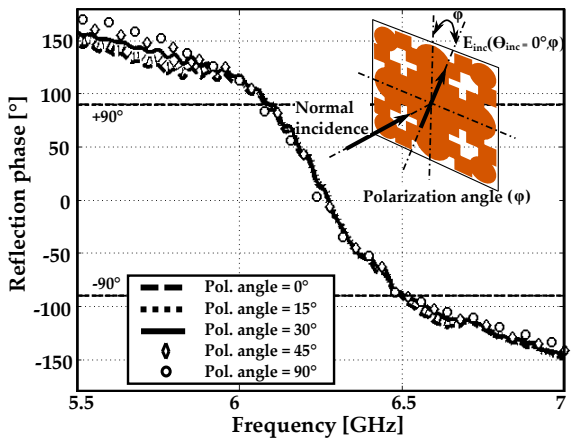


Figure 2.37: Reflection phase of the manufactured smooth AMC prototype for different incident field ($E_{\text{inc}}$) polarization angles ($\varphi$).

#### 2.2.2.3 Reflection Phase Characterization for Different Incident Angles

To obtain comprehensive information about the angular margin of stability of the presented structure under both flat and smooth bent conditions, the reflection coefficient phase versus frequency, for different oblique incident angles $\Theta_{\text{inc}}$ has been measured. Resonance conditions are met within an angular margin of stability $\Theta_{\text{inc}}$ = ±9° for the flat prototype (see Figure 2.38) whereas the obtained angular margin of stability for the smooth bent prototype is $\Theta_{\text{inc}} = \pm 8°$ (see Figure 2.39).

From the study conducted it can be concluded that it it possible to obtain a flexible AMC without reducing the bandwidth of AMC performance with respect to a rigid AMC that uses the same unit-cell design. The prototype has been manufactured using a thin and low relative dielectric permittivity commercial substrate and it shows polarization angle-independence under normal incidence and hardly

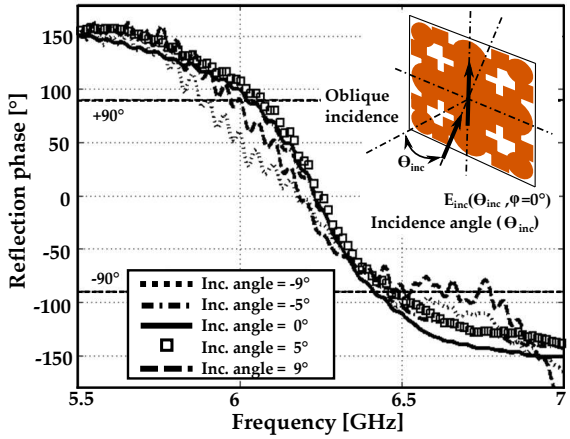


Figure 2.38: Reflection phase of the manufactured flat AMC prototype for different incident angles ($\Theta_{\text{inc}}$).

reduces its angular margin of stability when operates under oblique incidence.

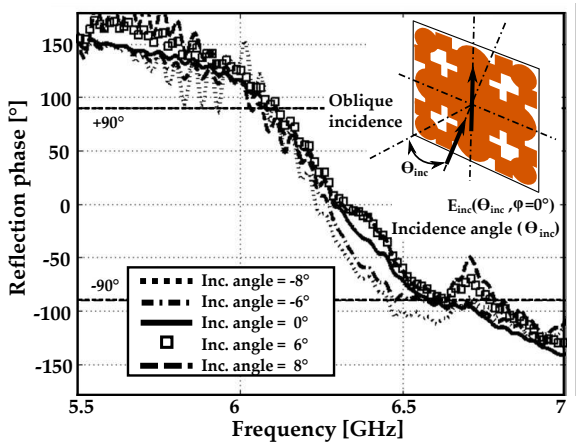


Figure 2.39: Reflection phase of the manufactured smooth AMC prototype for different incident angles ($\Theta_{\text{inc}}$).

### 2.2.3 Characterization of the Miniaturized Polarization Dependent AMC

Two planar AMC-2 prototypes of 30 x 30 unit-cells (12.6 x 12.6 $cm^2$) using RO3010 and RO4003C dielectric substrates have been manufactured (see Figure 2.40). Two horn probe antennas working in the band 4 - 9 GHz have been chosen as Tx and Rx. For the RO3010 dielectric substrate, $f = 4.15$ GHz and object-under-test size ($D = 12.6$ cm), the far field distance $RFF = 0.44$ m whereas for the RO4003C dielectric substrate, $f = 6.21$ GHz and the same size of the object-under-test ($D = 12.6$ cm), $RFF = 0.65$ m. In the anechoic chamber the separation between each probe and the object-under-test is 3 m, so the prototypes have been measured in the far field conditions.

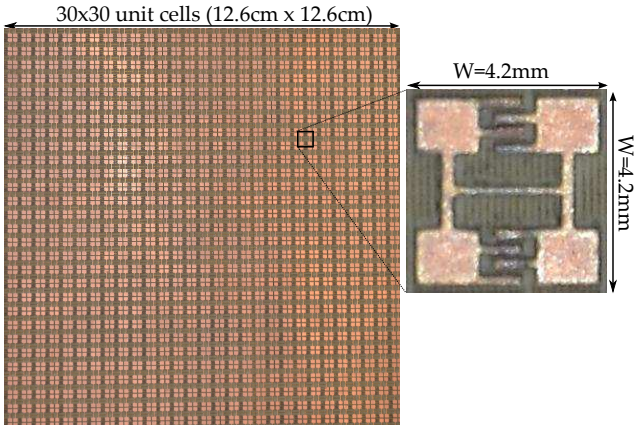


Figure 2.40: Manufactured AMC-2 prototype.

#### 2.2.3.1 Reflection Phase Measurement for AMC-2 Band Determination

The measured reflection phase for the AMC-2 prototype using RO3010 dielectric substrate is represented in Figure 2.41 together with the simulation results. The manufactured prototype has the resonance at 4.25 GHz which means a 2.4% deviation with respect to the simulation (4.15 GHz). The AMC-2 operation bandwidth is 67 MHz (1.6%), in good agreement with the simulated value.

For the RO4003C dielectric substrate, the measured resonance frequency is 6.3 GHz (having a variation with respect to the simulations of 1.45%) whereas the obtained bandwidth is 206 MHz (3.33%). The slight frequency shift between the measured AMC-2 resonance frequency and simulated value on the two different dielectric substrates is typically due to the variation of relative dielectric permittivity,

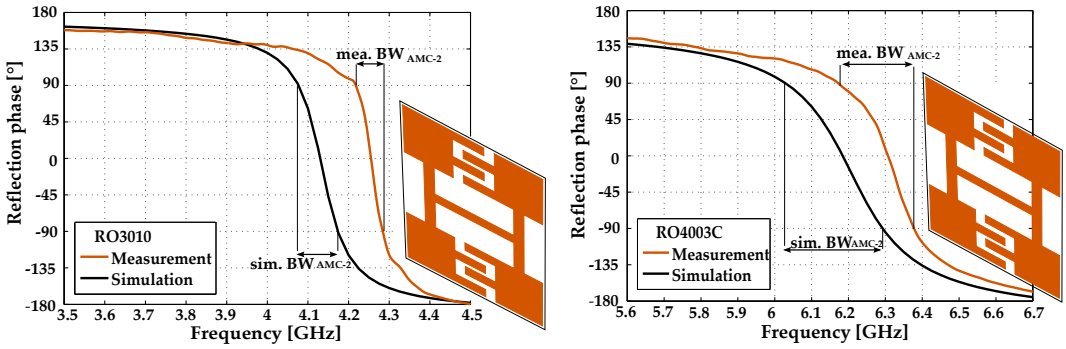


(a) using RO3010 (b) using RO4003C

Figure 2.41: Reflection phase of the AMC-2 design using RO3010 and RO4003C dielectric substrates.

$\epsilon_r$ with respect to its nominal value used in the simulations and to the manufacturing process tolerances.

In Table 2.8 an analysis between the simulated and measured results is presented. The thicker the dielectric substrate, the less angular margin of stability, according to the comparison done in Table 2.8. As the relative permittivity increases the angular margin of stability increases also.

| | | AMC-2 | AMC-2 |
|---|---|---|---|
| Unit-cell size [mm] | | 4.2 ($\lambda_0$/17) | 4.2 ($\lambda_0$/12) |
| Relative permittivity $\varepsilon_r$ | | 10.2 | 3.38 |
| Dielectric thickness [mm] | | 1.27 ($\lambda_0$/57) | 1.52 ($\lambda_0$/32) |
| Reso. freq [GHz] (Sim)* | TE/TM | 4.15/6 | 6.2/8.5 |
| Reso. freq [GHz] (Mea)* | TE/TM | 4.25/- | 6.3/- |
| Bandwidth [%] (Sim)* | TE/TM | 2.4/12.5 | 4.4/22 |
| Bandwidth [%] (Mea)* | TE/TM | 1.6/- | 3.33/- |
| Ang. Stab [º] (Sim)** | TE/TM | 75/- | 65/- |
| Ang. Stab [º] (Mea)*** | TE/TM | -/- | 10/- |
| * Computed for normal incidence and 0° polarization angle<br>** Angular margin of stability computed for different incident angles assuming 0° polarization angle<br>*** Angular margin of stability for the 12.6 x 12.6 cm$^2$ manufactured prototype | | | |

Table 2.8: Analysis of presented miniaturized AMC-2 unit-cell.

#### 2.2.3.2 Reflection Phase Characterization for Different Field Polarization Angles

The reflection phase of the manufactured AMC-2 structure has been measured for different incident field ($E_{\text{inc}}$) polarization angles ($\varphi$) using RO4003C. Resonance conditions are met when the structure is illuminated with incident plane wave with polarization angles that vary from 0° to 22° as shown in Figure 2.42.

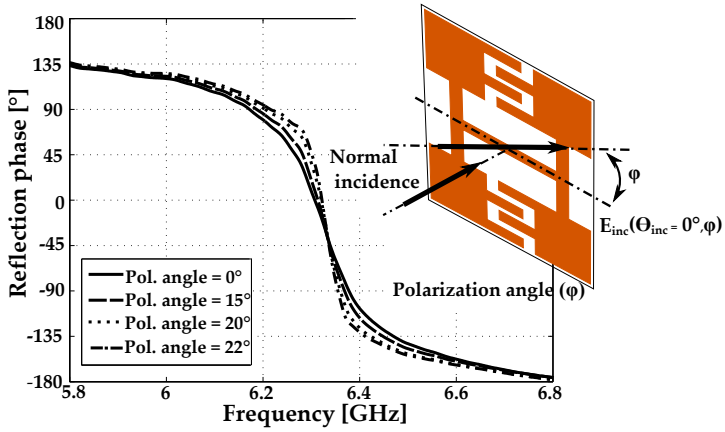


Figure 2.42: Reflection phase of the manufactured AMC-2 structure for different incident field ($E_{\text{inc}}$) polarization angles ($\varphi$) under normal incidence.

#### 2.2.3.3 Reflection Phase Characterization for Different Incident Angles

The angular margin of stability under oblique incidence of AMC-2 structure has also been analyzed. For the 12.6 cm x 12.6 cm manufactured prototype it was obtained an angular margin of stability $\Theta_{\text{inc}}= \pm 10°$ (see Figure 2.43). The differences between the simulated and measured angular margin of stability can be attributed to the small and finite size of the manufactured prototype, which leads to some nulls in the scattered field amplitude, depending on the incident angle and the distance between the prototype and horn probe antennas. The same happens when characterizing a finite-size PEC following the same procedure.

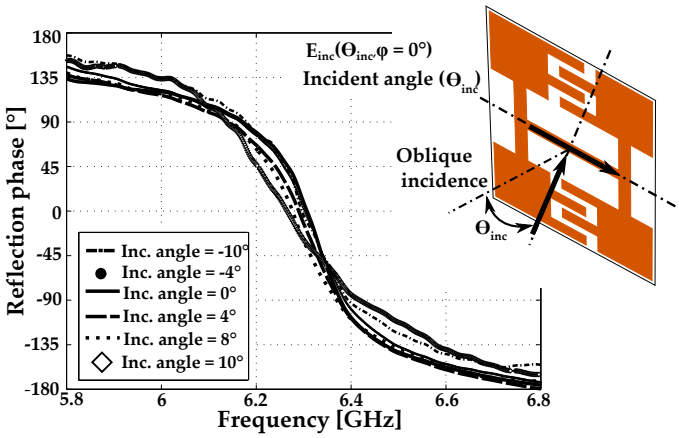


Figure 2.43: Reflection phase of the manufactured AMC-2 structure for different oblique incident angles ($\Theta_{\text{inc}}$) under 0° polarization angle.

### 2.2.4 Characterization of the Miniaturized Polarization Insensitive AMC

An AMC prototype of 15 x 15 unit-cells (12.6 x 12.6 cm$^2$) using RO4003C dielectric substrate has been manufactured (Figure 2.44). The prototype has the same size (12.6 x 12.6 cm$^2$) as the miniaturized polarization dependent AMC and it is characterized in terms of its reflection coefficient phase.

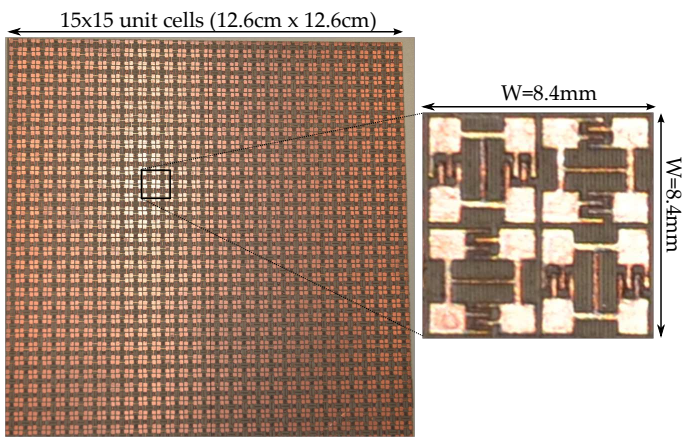


Figure 2.44: Manufactured polarization insensitive AMC prototype.

Two horn antennas working as Tx and Rx in the 5.4 - 12.4 GHz frequency band have been chosen for the measurement setup. The separation between each horn antenna and the object-under-test is 3 m. The polarization insensitive AMC works

in two different frequency bands, therefore if the upper limit of the frequency band (10.4 GHz, $\lambda_0$= 2.88 cm) is considered and the object-under-test size is $D = 12.6$ cm, the resulted far field distance is $RFF = 1.10$ m. Furthermore, for the lower frequency band (6.2 GHz, $\lambda_0$= 4.83 cm) and the same object-under-test size $D = 12.6$ cm, $RFF$ = 0.65 m. Hence, the prototype has been measured in far field conditions.

#### 2.2.4.1 Reflection Phase Measurement for AMC Band Determination

The measured reflection phase for the polarization insensitive AMC prototype is represented in Figure 2.45 together with the simulation results. The manufactured prototype has the lower resonance at 6.5 GHz which means a 5% deviation with respect to the simulation (6.2 GHz). The polarization insensitive AMC operation bandwidth is 185 MHz (2.9%), in good agreement with the 275 MHz (4.4%) simulated bandwidth.

Regarding the upper frequency band, the measured polarization insensitive AMC operation bandwidth is 2.03 GHz (19%) at 10.7 GHz, whereas the simulated one is 2.29 GHz (22%) at 10.4 GHz. The resonance frequency variation between measurements and simulations is about 3%. In measurements, both resonance shift upwards in frequency due to the variation of the relative permittivity of the dielectric substrate. This means that the relative permittivity of the RO4003C substrate used for manufacturing the AMC is lower than the nominal value 3.38 used in simulations.

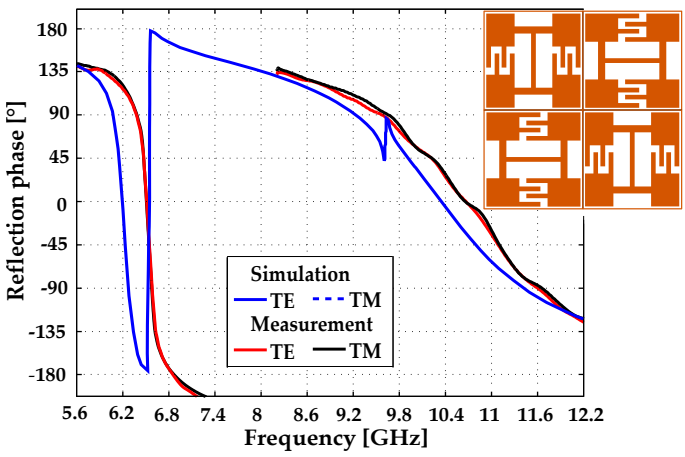


Figure 2.45: Reflection phase of the manufactured polarization insensitive AMC prototype.

#### 2.2.4.2 Reflection Phase Characterization for Different Field Polarization Angles

The reflection phase of the manufactured polarization insensitive AMC structure has been measured for different incident field ($E_{\text{inc}}$) polarization angles ($\varphi$). According to simulation results shown in Figure 2.46, the AMC is polarization independent and resonance conditions are met no matter what polarization angle of the incident field is used to illuminate the structure.

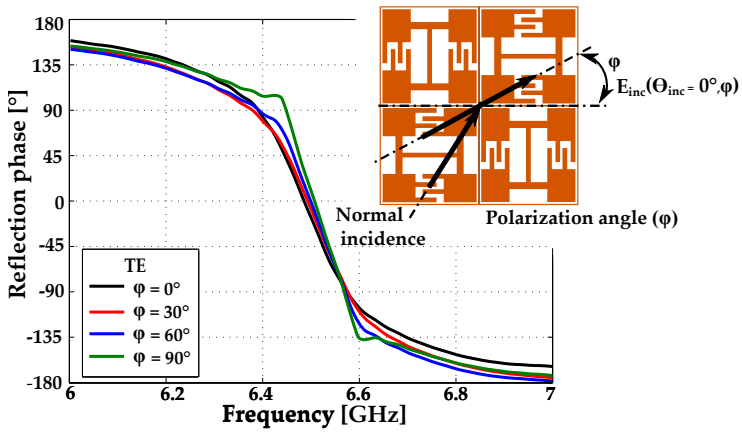


Figure 2.46: Lower frequency band. Reflection phase of the manufactured polarization insensitive AMC prototype for different incident field ($E_{\text{inc}}$) polarization angles ($\varphi$) under normal incidence.

#### 2.2.4.3 Reflection Phase Characterization for Different Incident Angles

The angular margin of stability under oblique incidence of the polarization insensitive AMC structure has also been analyzed. For the 12.6 cm x 12.6 cm manufactured prototype it was obtained an angular margin of stability $\Theta_{\text{inc}}= \pm 12°$ for TE polarized waves whereas for the TM polarized waves $\Theta_{\text{inc}}= \pm 10°$ (see Figure 2.47 and Figure 2.48). In the absence of vias, the angular margin of stability for the TM polarized waves is slightly smaller than for the TE case, the structure being less stable.

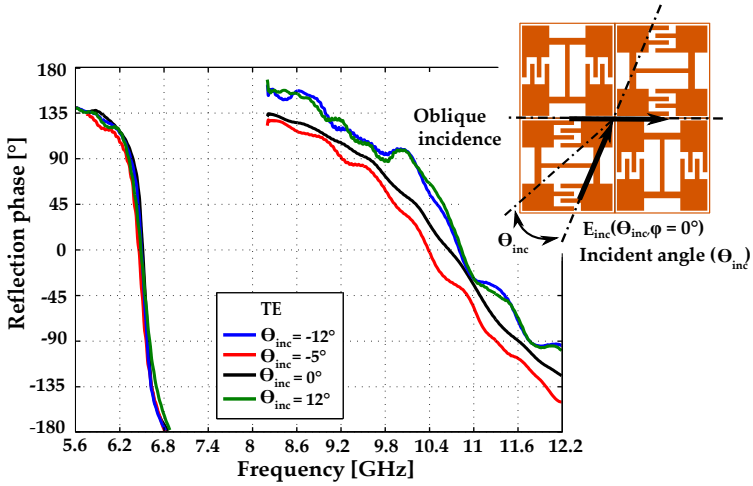


Figure 2.47: TE polarized waves. Reflection phase of the manufactured polarization insensitive AMC prototype for different incident angles ($\Theta_{\text{inc}}$).

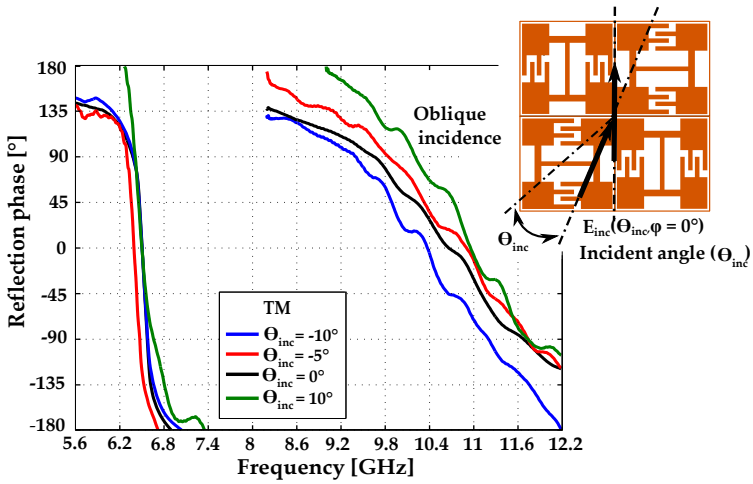


Figure 2.48: TM polarized waves. Reflection phase of the manufactured polarization insensitive AMC prototype for different incident angles ($\Theta_{\text{inc}}$).

## 2.3 AMC Analytical Model

The characteristics of the AMC structures can be described by either employing electromagnetic simulations or by using analytical models.

Several analytical AMC models have been proposed [1, 10, 36, 37, 38, 39, 40, 41]. When the periodicity of the unit-cell is small compared to the operating wavelength, the effective medium model with simple lumped LC elements can be used. In this model, the capacitance is calculated using the electrostatic field distribution for a gap between two semi-infinite strips (see Figure 2.49) whereas the value of the inductance results from the current loop between the metallization and the ground plane. Other AMC analytical models are based on transmission line model either for surface waves or plane waves. The transmission line model for plane waves is more general since it takes into consideration the incident angle of an arbitrary plane wave and provides accurate results.

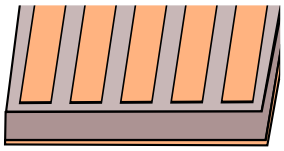

Figure 2.49: Semi-infinite strips.

The AMC analytical equivalent circuit model based on transmission line theory for TE and TM polarized plane waves is proposed and validate by comparing it with full-wave electromagnetic simulation results. Based on the model, several parameters are tuned, showing how to control the operational bandwidth and resonance frequency.

In order to model each unit-cell, the structure should be divided into a metallo-dielectric Frequency Selective Surface (FSS) and a grounded dielectric slab which acts as a separation medium between the FSS and ground plane (Figure 2.50).

The AMC surface impedance $Z_{\mathrm{s}}$ can be expressed as a parallel connection of the grid impedance $Z_{\mathrm{g}}$ and the dielectric impedance $Z_{\mathrm{d}}$ of the substrate slab backed by an ideally conducting plane (Figure 2.51).

$$\frac{1}{Z_s^{TE/TM}} = \frac{1}{Z_g^{TE/TM}} + \frac{1}{Z_d^{TE/TM}} \tag{2.11}$$

The grid impedance $Z_{\mathrm{g}}$ depends on the specific geometry used in the design of the unit-cell and also on the orientation of the electric field vector.

The dielectric impedance of the grounded dielectric substrate, considering TE and TM polarizations of the incident wave, can be written as:

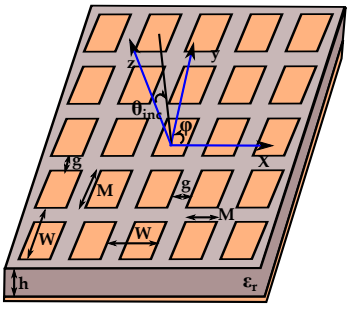


Figure 2.50: Surface impedance of an AMC.

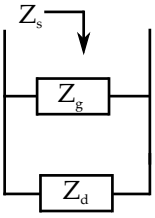


Figure 2.51: Surface impedance of an AMC.

$$Z_d^{TE} = j\omega\mu_0 h \tag{2.12}$$

$$Z_d^{TM} = j\omega\mu_0 h cos^2(\Theta_{inc}) \tag{2.13}$$

where $\mu_0$ is the free space permeability, $h$ is the thickness of the dielectric substrate and $\Theta_{\mathrm{inc}}$is the incident angle.

When vertical vias are absent, the $Z_{\mathrm{d}}{}^{\mathrm{TE}}$ dielectric impedance remains unchanged but $Z_{\mathrm{d}}{}^{\mathrm{TM}}$ strongly depends on the incident angle.

The surface impedances $Z_{\mathrm{s}}{}^{\mathrm{TE}}$ and $Z_{\mathrm{s}}{}^{\mathrm{TM}}$ lead to their corresponding reflection coefficients $\Gamma^{\mathrm{TE}}$ and $\Gamma^{\mathrm{TM}}$with the following expressions:

$$\Gamma^{TE/TM} = \frac{Z_s^{TE/TM} - Z_0^{TE/TM}}{Z_s^{TE/TM} + Z_0^{TE/TM}} \tag{2.14}$$

$$Z_0^{TE} = \frac{\eta_0}{cos(\Theta_{inc})} \tag{2.15}$$

$$Z_0^{TM} = \eta_0 cos(\Theta_{inc}) \tag{2.16}$$

$$\Gamma^{TE} = \frac{Z_s^{TE} cos(\Theta_{inc}) - \eta_0}{Z_s^{TE} cos(\Theta_{inc}) + \eta_0} \tag{2.17}$$

$$\Gamma^{TM} = \frac{Z_s^{TM} - \eta_0 cos(\Theta_{inc})}{Z_s^{TE} + \eta_0 cos(\Theta_{inc})} \tag{2.18}$$

where $\eta_0$ is the free space impedance (120π) and $\Theta_{\text{inc}}$ is the incident angle.

In order to estimate the phase of the reflection coefficient the following expression is used:

$$\Phi = Im[ln(\Gamma^{TE/TM})] \tag{2.19}$$

The relative error between the resonance frequency obtained from the analytical model and from the electromagnetic simulation is:

$$Error(\%) = |\frac{f_{r,analytical.model} - f_{r,elect.simulation}}{f_{r,elect.simulation}}| * 100 \tag{2.20}$$

### 2.3.1 Analytical Model of the Miniaturized Polarization Dependent AMC

Let us consider the miniaturized polarization dependent AMC-2 which was previously presented in Section 2.1.2 (see Figure 2.52).

In general, the AMC structure should preserve its resonance frequency under oblique incidence for all angles for both TE and TM polarized waves. However, if the unit-cell presents an asymmetrical geometry, like the unit-cell replicated to form the polarization dependent AMC-2, the structure does not exhibit the same resonance frequency, so it behaves differently for TE and TM polarized waves [10]. Moreover, in the absence of via holes a larger angular spectrum for TE polarized waves compared to TM polarized waves is expected.

Determining the grid impedance of a unit-cell whose geometry is different from a patch is not trivial at all. For normal incidence the $Z_g{}^{TE}$ $(\omega,0°)$ and $Z_g{}^{TM}(\omega,0°)$ grid impedances can be computed using the circuits presented in Figure 2.52. The grid impedance of the structure for TE polarized waves under oblique incident angles is the multiplication between the grid impedance for normal incidence $Z_g{}^{TE}(\omega,0°)$ and a $\Theta_{\text{inc}}$dependent factor ($F^{TE}(\Theta_{inc})$).

$$Z_g^{TE}(\omega, \Theta_{inc}) = F^{TE}(\Theta_{inc}) Z_g^{TE}(\omega, 0^{\circ}) \tag{2.21}$$

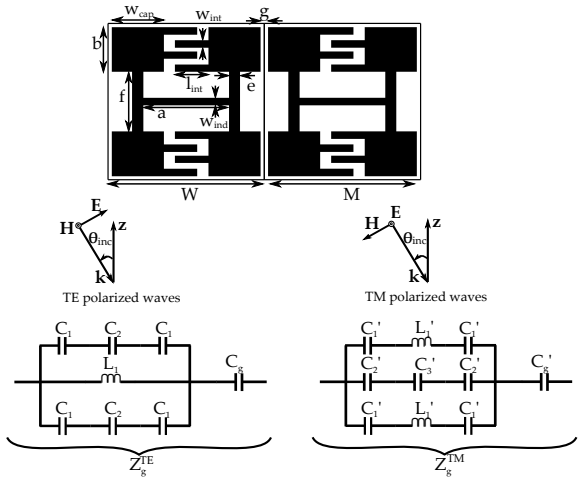


Figure 2.52: AMC-2 unit-cell - Equivalent circuit model of the grid impedance for TE and TM polarized waves.

$$F^{TE}(\Theta_{inc}) = \frac{1}{\varepsilon_r + 1} cos(\Theta_{inc})^{1/2} \tag{2.22}$$

Taking into account the polarized wave, for each circuit, the inductors $L_1$ and $L_1$' model the straight line from the middle of the unit-cell geometry, the capacitors $C_1$ and $C_1$' represent the metallic pads from the corners of the unit-cell whereas $C_2$ and $C_2$' define the interdigital capacitors. The capacitors $C_{\mathrm{g}}$ and $C_{\mathrm{g}}$' represent the coupling and the gap between each unit-cell [42].

The inductance $L_{\mathrm{l}}$ (for TE polarized waves), $L_{\mathrm{l}}$' (for TM polarized waves) of a straight wire on top of a ground plane can be written as follow [43]:

$$L_1 = F_l \frac{\mu_0}{4\pi} ln \left\{ 1 + \frac{32h^2}{F_w^2} \left[ 1 + \sqrt{1 + \left( \frac{\pi F_w^2}{8h^2} \right)^2} \right] \right\} \tag{2.23}$$

where, for TE polarized waves:

$$F_l = a, F_w = w_{ind} \tag{2.24}$$

where, for TM polarized waves:

$$F_l = f, F_w = e \tag{2.25}$$

The capacitance $C_{\mathrm{g}}$ (for TE polarized waves), $C_{\mathrm{g}}$' (for TM polarized waves) for the narrow gap is given by the following equation [1]:

$$C_g = F_g \frac{M\varepsilon_0(1+\varepsilon_r)}{\pi} cosh^{-1}\left(\frac{M+g}{g}\right) \tag{2.26}$$

where, for TE polarized waves:

$$F_g = 10^3 d\sqrt{2} \tag{2.27}$$

where, for TM polarized waves:

$$F_g = 1 \tag{2.28}$$

where $M$ is the dimension of the unit-cell metallization and $g$ is the gap.

The capacitance $C_1$ (for TE polarized waves), $C_1$' (for TM polarized waves) due to metallic pads is obtained by [42] and [44]:

$$C_1 = \frac{1}{2}(\frac{\sqrt{\varepsilon_{re}}}{cZ_0} - \varepsilon_0\varepsilon_r\frac{F_{cap}}{h}) \tag{2.29}$$

$$\varepsilon_{re} = \frac{\varepsilon_r+1}{2} + \frac{\varepsilon_r-1}{2}F_{\varepsilon_{re}} \tag{2.30}$$

$$F_{\varepsilon_{re}} = (1+\frac{12h}{F_{cap}})^{-\frac{1}{2}} \tag{2.31}$$

$$Z_0 = \frac{\eta_0}{\sqrt{\varepsilon_{re}}}[\frac{F_{cap}}{h} + 1.393 + 0.667ln(\frac{F_{cap}}{h} + 1.444)]^{-1} \tag{2.32}$$

where, for TE polarized waves:

$$F_{cap} = w_{cap} \tag{2.33}$$

where, for TM polarized waves:

$$F_{cap} = b \tag{2.34}$$

where $\eta_0$ is the free space impedance, $c$ is the velocity of light in free space, $Z_0$ is the characteristic impedance and $\varepsilon_{\mathrm{re}}$ is the effective permittivity reported by Wheeler and Schneider.

The last capacitance $C_2$ (for TE polarized waves), $C_2$' (for TM polarized waves) is evaluated by [42]:

$$C_2 = F_{int}(\varepsilon_r+1)[(N-3)A1 + A2] \tag{2.35}$$

$$A_1 = 4.409e^{-6}tanh[0.55(\frac{h}{F_w})^{0.45}] \tag{2.36}$$

$$A_2 = 9.92e^{-6}tanh[0.52(\frac{h}{F_w})^{0.5}] \tag{2.37}$$

where, for TE polarized waves:

$$F_{int} = l_{int}, F_w = w_{int} \tag{2.38}$$

where, for TM polarized waves:

$$F_{int} = w_{int}, F_w = w_{int} \tag{2.39}$$

where $w_{\text{int}}$ represents the width of the interdigital capacitor's finger, $\text{l}_{\text{int}}$ represents the length of the interdigital capacitor's finger and $N$ is the number of fingers, in this case $N = 4$.

As it can be found also in Section 2.1.2 , from electromagnetic simulations, the structure weakly depends on $\Theta_{\text{inc}}$ , therefore only the analytical model of the TE angular margin of stability has been considered.

Similar formulas for TM polarized plane waves can be used in order to determine the phase of the reflection coefficient varying the angle of incidence.

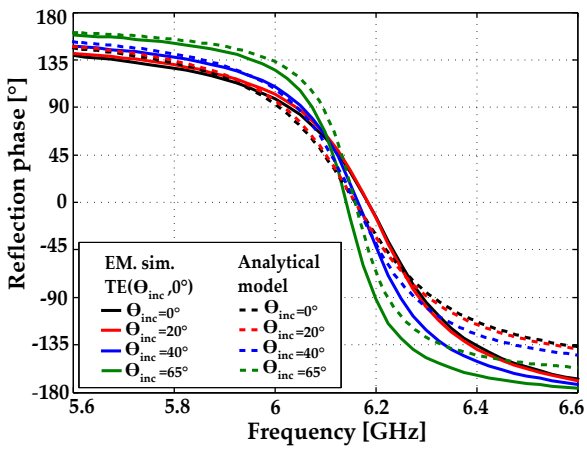


Figure 2.53: Simulated reflection phase of the AMC-2 resulted from the electromagnetic simulation and analytical model when $\Theta_{\text{inc}}$ is varied for TE polarized plane waves.

In Figure 2.53, for TE polarized plane waves, the electromagnetic simulation of the reflection phase for different oblique incident angles and 0° polarization angle

(*TE(Θ$_{inc}$,0°)*) reveals an angular stability of 65° at 6.2 GHz using RO4003C dielectric substrate.

By employing the analytical model for TE polarized plane waves, resonance conditions are met and accurate results are obtained when the structure is illuminated with oblique incident angles that vary from 0° to 65°. For normal incidence, the relative error is 0.6%.

Considering the analytical model for TM polarized waves under normal incidence and 0° polarization angle (*TM(0°,0°)*) and compared to the *TM(0°,0°)* electromagnetic simulation, the shape of both curves representing the reflection coefficient phase matches. The same resonance frequency (8.5 GHz) and bandwidth (22%) occurs (see Figure 2.54).

After presenting the comparison between the analytical model and the electromagnetic simulation when the incident angle $\Theta_{\text{inc}}$ is varied and the polarization angle is set to 0° for the given miniaturized polarization dependent AMC-2, the next step is to discuss the effects of the unit-cell geometry on the resonant frequency and operational bandwidth.

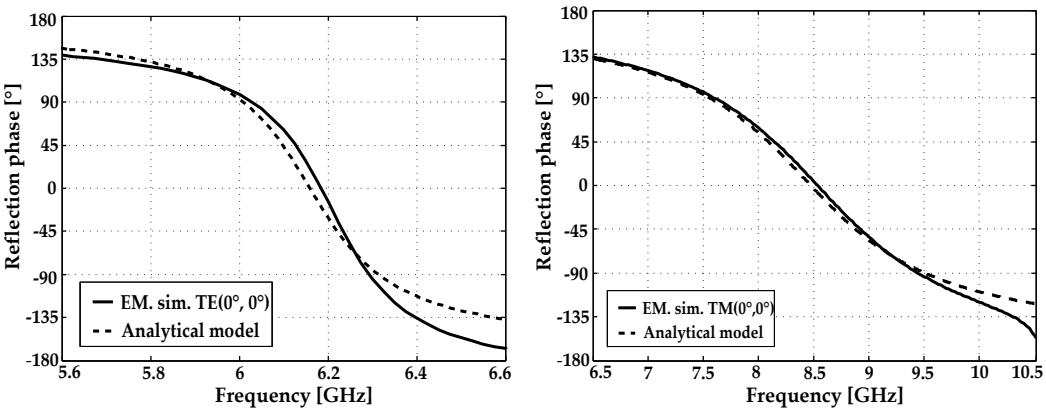


(a) TE(0°, 0°) (b) TM(0°, 0°)

Figure 2.54: Simulated reflection phase of the AMC-2 resulted from the electromagnetic simulation and analytical model for normal incidence.

The reflection phase and bandwidth of the AMC-2 structure are mainly determined by the following parameters: capacitive interdigital fingers' length ($l_{\text{int}}$), inductive component width ($w_{\text{ind}}$), gap width ($g$), substrate dielectric permittivity ($\varepsilon_{\text{r}}$) and dielectric substrate thickness ($h$).

The equivalent circuit model and the electromagnetic simulation results are found to be accurate within 1% over the following range of parameters: $1 \leq \varepsilon_{\text{r}} \leq 6$ (if $6 < \varepsilon_{\text{r}} \leq 10$ the accuracy obtained is within 5%), 0.76 mm $\leq h \leq$ 2.52 mm (if 2.52 <

$\varepsilon_r \leq 3.52$ the accuracy obtained is within 5%), 0.1 mm $\leq g \leq$ 0.5 mm, 0.1 mm $\leq w_{\text{ind}} \leq$ 0.5 mm.

#### 2.3.1.1 Capacitive Interdigital Finger Effect

The interdigital capacitor plays an important role in determining the characteristics of the structure. In order to see the effect of the interdigital capacitor, the length of its fingers is decreased from $l_{\text{int}}$= 0.9 mm to $l_{\text{int}}$= 0.7 mm and all the other parameters are not changed. As it is expected, by decreasing the $l_{\text{int}}$ to 0.7 mm, the resonance frequency increases to 6.575 GHz as well does the bandwidth, increasing from 4.4% to 6.84% compared to the results of the reference *TE(0°, 0°)* electromagnetic simulation for $l_{\text{int}}$= 0.9 mm. .

One can observe that the fingers' length of the interdigital capacitor has the same effect as increasing the unit-cell size. It should be noted that by increasing the fingers' length, the dimension of the whole unit-cell stays the same, down shifting the resonance frequency. Hence, interdigital capacitors are useful for obtaining smaller unit-cells at lower frequency without increasing the unit-cell size.

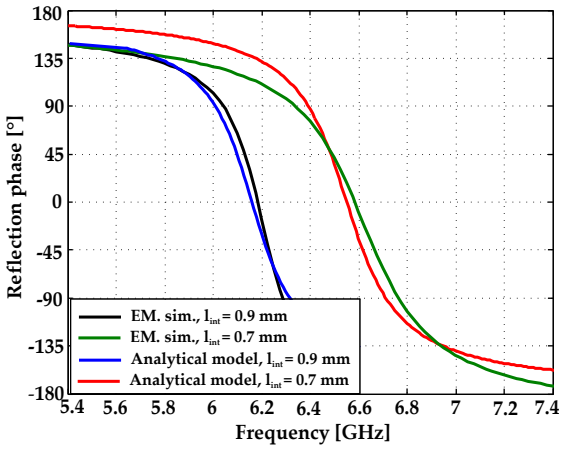


Figure 2.55: The effect of the capacitive interdigital fingers' length for *TE (0°, 0°)*.

The reflection phases resulting from the proposed model and electromagnetic simulations in the case of $l_{\text{int}}$= 0.7 mm are presented in Figure 2.55. The resonance frequency of 6.55 GHz is predicted by the equivalent circuit model, respectively 6.575 GHz using HFSS. The relative error of predicted resonance frequency is 0.38%.

#### 2.3.1.2 Inductive Component Width Effect

The resonance frequency and bandwidth of the AMC-2 are affected by the variation of the inductive component width. In this study, $w_{\text{ind}}$ parameter is doubled and set to 0.4 mm, all other parameters being kept the same. As the inductive width increases, the resonance shifts to a higher frequency 6.75 GHz, whereas the bandwidth gets larger, reaching 5.92%.

The resonance frequencies from the analytical model and electromagnetic simulations in the case of $w_{\text{ind}}$= 0.4 mm are 6.73 GHz, respectively 6.75 GHz (see Figure 2.56). The relative error of predicted resonance frequency is 0.3%.

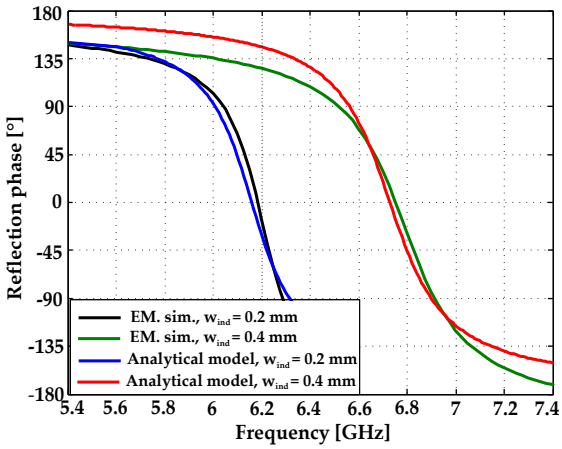


Figure 2.56: The effect of inductive component width for *TE (0°, 0°)*.

#### 2.3.1.3 Gap Width Effect

The gap width influences the distance between the metallization edge and the unit-cell edge, therefore the distance between the metallization of two adjacent unit-cells. The variation of the gap width affects the resonance frequency and bandwidth. The gap width is changed from $g$ = 0.2 mm to $g$ = 0.4 mm whereas the other parameters of the structure are kept the same.

From Figure 2.57, it can be extracted that as the gap width increases to 0.4 mm, the resonance frequency increases also to 6.35 GHz. A slight bandwidth enhancement from 4.4% to 4.5% is reported. Moreover, the resonance frequency predicted by the analytical model is 6.31 GHz compared to 6.35 GHz of the reference *TE(0°,0°)* electromagnetic simulation for $g$ = 0.4 mm. The relative error obtained is 0.62%.

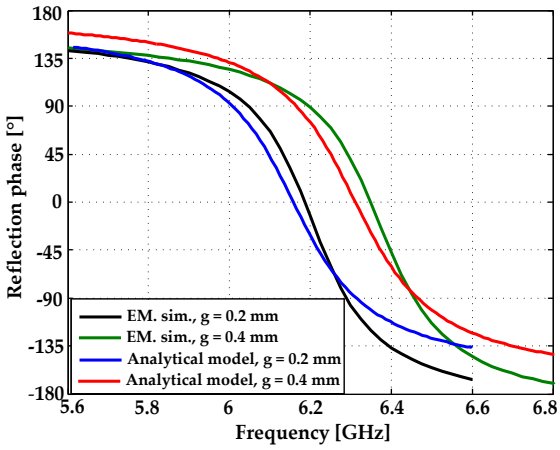


Figure 2.57: The effect of gap width for *TE(0°, 0°)*.

#### 2.3.1.4 Dielectric Substrate Thickness Effect

Nowadays AMC designs on thin substrates are very attractive for applications regarding planar antennas and microwave devices. The substrate thickness has a primary role in tuning the bandwidth of the structure. The substrate thickness is increased from $h = 1.52$ mm to $h = 2.52$ mm.

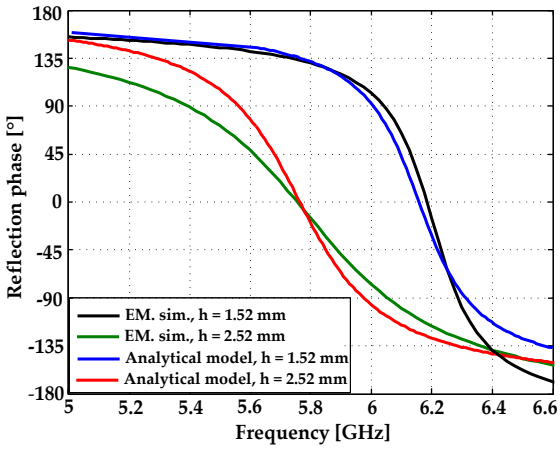


Figure 2.58: The effect of dielectric substrate thickness for *TE(0°, 0°)*.

Figure 2.58 shows that, when the dielectric substrate thickness is increased, the resonance frequency decreases from 6.2 GHz to 5.75 GHz and at the same time the bandwidth is enlarged from 4.4% to 11.30%. The predicted resonance frequency of the equivalent circuit model and HFSS electromagnetic simulation when $h = 2.52$ mm are 5.77 GHz and 5.75 GHz. The relative error of prediction is 0.34%. De-

pending on the application requirements, a trade-off solution between the substrate characteristics, bandwidth and unit-cell size should be adopted.

#### 2.3.1.5 Substrate Dielectric Permittivity Effect

In order to vary the resonance frequency, the dielectric substrate permittivity can be modified. The structure has the same parameters except that the dielectric permittivity $\varepsilon_r$ is changed from 3.38 to 5.38.

In Figure 2.59, it is shown that by increasing the dielectric permittivity to $\varepsilon_r$= 5.38, the resonance frequency shifts downwards from 6.2 GHz (of the reference *TE(0°,0°)* electromagnetic simulations using $\varepsilon_r$= 3.38) to 4.9 GHz for $\varepsilon_r$= 5.38. The bandwidth is slightly reduced from 4.4% to 4.08%. In addition, the comparison between the reflection phases of the equivalent circuit model and electromagnetic HFSS simulations for $\varepsilon_r$= 5.38 is plotted. The resonance frequencies predicted by the equivalent circuit model and electromagnetic simulations are 4.93 GHz and 4.9 GHz meaning a relative error of 0.61%.

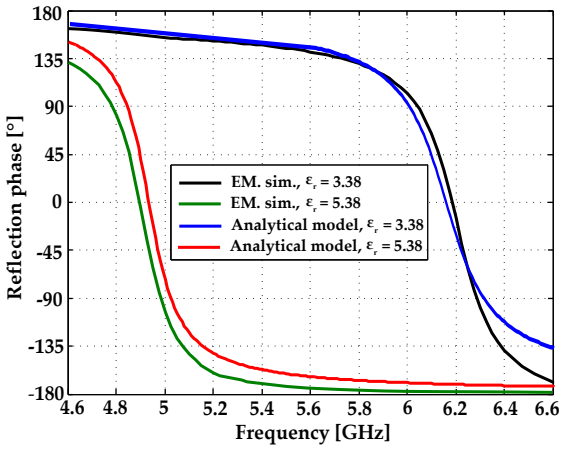


Figure 2.59: The effect of dielectric substrate permittivity.

### 2.3.2 Analytical Model of the 5.8 GHz AMC

Due to the complexity of the AMC unit-cell presented in Section 2.1.1, a simplified version of the equivalent circuit model will be used.

For decreasing and obtaining the 5.8 GHz resonance frequency, the patch-type unit-cell is modified and loaded by slots. In each bigger slot of the unit-cell a capacitor (having the same capacitance) is formed. Besides the new slots, new inductive elements (chamfers) are created. The chamfers are designed to have continuity in the unit-cell metallization and to strengthen the inductive unit-cell behavior (to enlarge the unit-cell bandwidth).

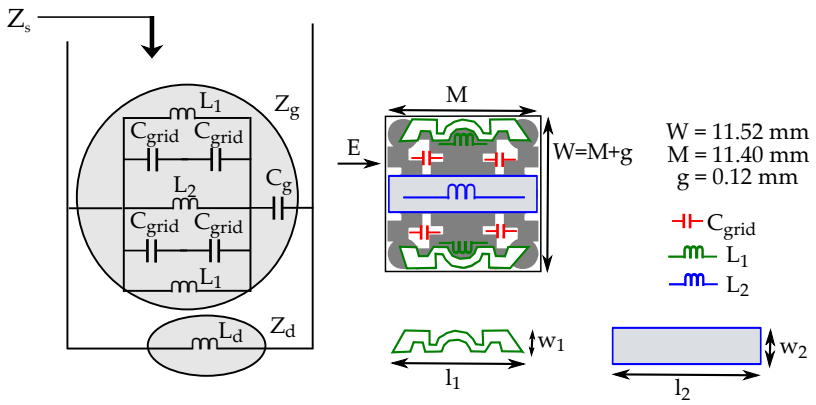


Figure 2.60: Equivalent circuit model.

The inductances $L_1$ and $L_2$ are influenced by the width, the length of the metallic track and the height of the dielectric substrate and are given by the following equations.

$$L_1 = l_1 \frac{\mu_0}{4\pi} ln \left\{ 1 + \frac{32h^2}{w_1^2} \left[ 1 + \sqrt{1 + \left( \frac{\pi F w_1^2}{8h^2} \right)^2} \right] \right\} \tag{2.40}$$

$$L_2 = l_2 \frac{\mu_0}{4\pi} ln \left\{ 1 + \frac{32h^2}{w_2^2} \left[ 1 + \sqrt{1 + \left( \frac{\pi w_2^2}{8h^2} \right)^2} \right] \right\} \tag{2.41}$$

where $l_1$= 10 mm, $w_1$= 1.42 mm, $l_2$= 11.3 mm, $w_2$= 2.85 mm and the height of the dielectric substrate is $h$ = 0.762 mm.

The capacitance $C_g$ and $C_{grid}$ are given by the following equations.

$$C_g = \frac{M\varepsilon_0(1+\varepsilon_r)}{\pi} cosh^{-1}\left(\frac{M+s}{g}\right) \tag{2.42}$$

$$C_{grid} = F\frac{M_1\varepsilon_0(1+\varepsilon_r)}{\pi}cosh^{-1}\left(\frac{M_1+s}{s}\right) \tag{2.43}$$

where $M$ is the dimension of the unit-cell metallization, $g$ is the gap between two adjacent unit-cells, $M_1$ is the dimension of the metallization around the slot and $s$ is the dimension of the slot. $F$ is a scale factor $F$=0.175(W/g). For ARLON25N $\varepsilon_r$ = 3.28.

The inductance $L_d$ is given by the following equation.

$$L_d = \mu_0 h \tag{2.44}$$

The grid impedance $Z_g$ is connected in parallel with the dielectric impedance $Z_d$ (see Figure 2.60).

From Figure 2.61 it can be seen that when $L_1$= 3.25 nH, $L_2$= 3.13 nH, $L_d$= 0.96 nH, $C_g$= 0.72 pF, $C_{grid}$= 0.76 pF, the phase of the reflection coefficient using the electromagnetic simulator and analytical model matches.

The metallic track from the middle of the unit-cell is wider and shorter compared to the metallic track from the border of the unit-cell that´s why the inductance $L_2$ has a lower value than the inductance $L_1$ .

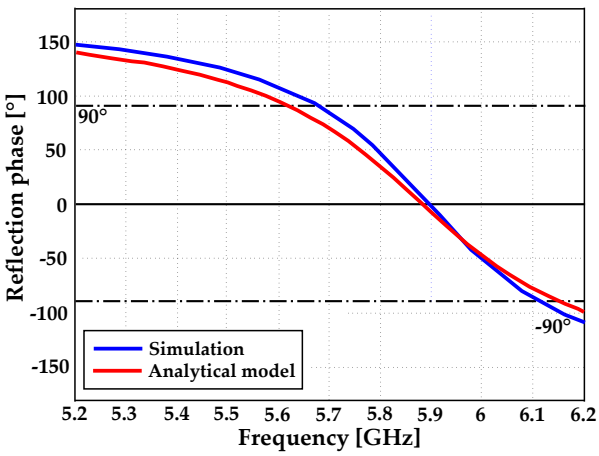


Figure 2.61: Comparison between the simulation results and the analytical model of the AMC.

## 2.4 AMC Applications

Dipole antennas perform properly in free space but they suffer from performance degradation when placed on or close to different materials such as metals or human tissue. The performance degradation of tag antennas is a critical problem that is hindering global deployment of passive UHF and SHF RFID systems. This loss of performance is due the material characteristics affecting antenna properties such as input impedance, radiation pattern and radiation efficiency [45, 46, 47, 48]. The electromagnetic wave is greatly reflected by the conductor surface yielding a significant reduction of the RFID tag operating distance or its total malfunctioning. Therefore, obtaining stable antenna in terms of matching and radiation characteristics when placed on various metallic platforms and also in the presence of user's body is desirable and worth developing.

Several approaches have been proposed to achieve uniform performance: to design an antenna that is electrically separated ($\lambda_0/4$) from the metallic object or to use a shorting plane or a stack of multiple layers. However, it will lead to an unacceptable increase in the antenna's height improper for flexible purposes and it will complicate the manufacturing process. Furthermore, the antenna can be electromagnetically insulated from the metal using ferro-electric materials with the disadvantage of being expensive.

Another possibility to overcome antenna's problems with metals is to use an Artificial Magnetic Conductor (AMC) since it has 0° reflection phase. So, the image current of the AMC will be in phase rather than out of phase with the original antenna current (as opposed to PEC ground plane that causes the antenna's current and its image to cancel each other, being out of phase). This is a proper solution to the destructive interference issue when the antenna is placed very close to the metallic surface, the AMC acting like a barrier between the antenna and metallic plate [1, 3, 12].

In this Doctoral Thesis, the antenna will be electromagnetically insulate from the object by using the artificial magnetic conductor, making possible the placement of the antenna in the metallic object's vicinity and in the presence of human body without loosing performance.

In order to validate the simulated results, the measurements are done in an anechoic chamber. The inter-comparison method is employed for measuring the gain.

Two identically reference probe antennas working in the same frequency band as the antenna under study are needed. The gain of the probe antenna depending on the working frequency is known as $G_{\text{probe}}$.

The radiation field level of the antenna under study is measured. The maximum field value is determined as being: $E_{\text{antenna}}$. In the end, the antenna under study is changed by the probe antenna and the radiation field level of the probe antenna is measured. The maximum field value is determined as being: $E_{\text{probe}}$. Knowing these 3 values, the peak realized gain of the antenna under study can be computed using the following formula.

$$G_{antenna}[dB] = G_{probe}[dB] + (E_{antenna}[dB] - E_{probe}[dB]) \tag{2.45}$$

The directivity is computed by integrating the radiation pattern. Both the gain and directivity are measured at the resonance frequency of each prototype. The measured gain is the peak realized gain. It takes into account the reflection losses at the input of the antenna, the losses of the cables, etc.

Knowing the directivity and the gain of the antenna under study, the radiation efficiency can be computed.

$$G_{antenna}[dB] = \eta_{rad}(\%) D_{dipole}[dB] \tag{2.46}$$

$$\eta_{rad}(\%) = 100 * 10^{[G_{dipole}[dB] - D_{dipole}[dB]]/10} \tag{2.47}$$

### 2.4.1 Application in the 5.8 GHz SHF (Super High Frequency) RFID Band

The design of a coplanar waveguide (CPW)-fed double bow-tie slot antenna at 5.8 GHz is firstly shown, followed by an adaptation of the AMC presented in Section 2.1.1. Then, both structures are combined, yielding a CPW-fed double bow-tie slot antenna–AMC structure combination (henceforth referenced as Bow-tie–AMC). Return loss, gain and radiation patterns of a Bow-tie–AMC prototype are investigated based on measurements in an anechoic chamber. In addition, a comparison between radiation characteristics of the Bow-tie–AMC prototype alone and the Bow-tie–AMC prototype on a metallic plate is carried out based on measurements to show that the presented design is proper to be used for RFID tags on metallic objects.

#### 2.4.1.1 Bow-tie Design at 5.8 GHz

The CPW-fed bow-tie slot antenna [49, 50, 51] is a broadband design. The antenna has been designed to be suitable for RFID tags at 5.8 GHz using RO4003C, with relative dielectric permittivity $\varepsilon_r = 3.38$ , tan $\delta = 0.0027$, and a thickness $h =$ 1.524 mm (60 mils). The geometry of the proposed CPW-fed slot double bow-tie

antenna with its dimensions are shown in Figure 2.62. The characteristic impedance of the CPW line is 50 Ω. This antenna has a simple structure with only one layer of dielectric substrate. There is no ground below the dielectric substrate, that is, ungrounded CPW.

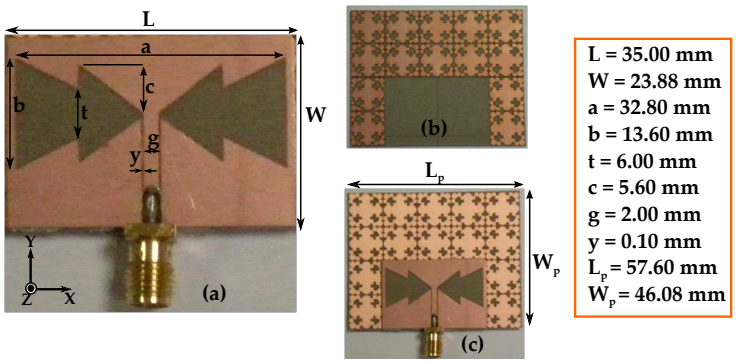


Figure 2.62: Elements of the manufactured prototype: (a) double bow-tie antenna; (b) AMC unit-cell arrangement; (c) Bow-tie-AMC prototype.

The antenna design has been carried out using method of moments simulator of Advanced Design System (Momentum) [52]. 2.5D electromagnetic simulators such as Momentum are primarily the same as 2D simulators except the extra half-dimension which means that the solver can calculate currents in the vertical direction (usually for substrates with vias) as well as in the horizontal direction.

Under the condition of 50 Ω feed line at the 5.8 GHz desired frequency, the tapering of the CPW bow-tie slot antenna is designed (since increasing $y$ results in shifting the resonating frequency with a slight reduction in the return loss value). The antenna resonance frequency is given by the parameter $a$ (increasing $a$ shifts the operating band to a lower frequency range) whereas the parameter $b$ controls the bandwidth and the level of the return loss at the main resonance frequency. Figure 2.63 shows the parametric study of $y$, $c$, $t$ and $b$. Only one parameter is changed at a time during the analysis. The double structure parameters $c$ and $t$ are opposite in behavior, so a trade-off is adopted. Increasing the value of $c$ results in a reduction of both the frequency of operation as well as the impedance matching.

From Figure 2.64, where the simulated return loss is shown, it can be extracted that the operating bandwidth of the CPW-fed slot double bow-tie antenna is 1.15 GHz (20.10%).

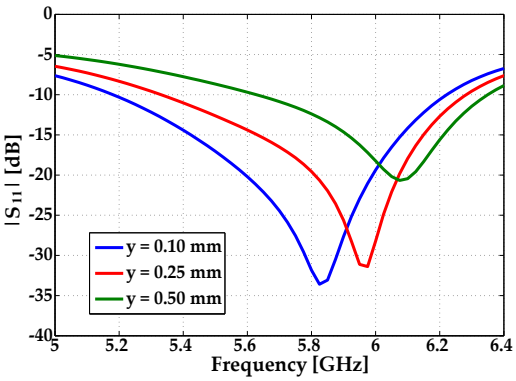


(a) Influence of the $y$ parameter

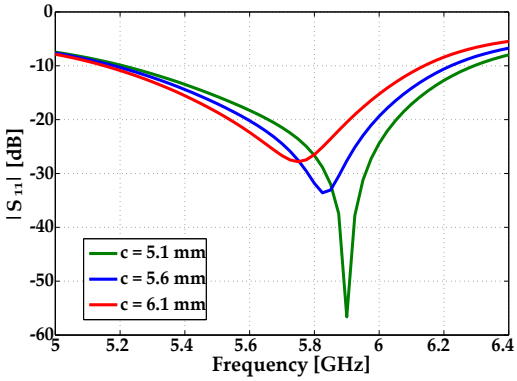


(b) Influence of the $c$ parameter

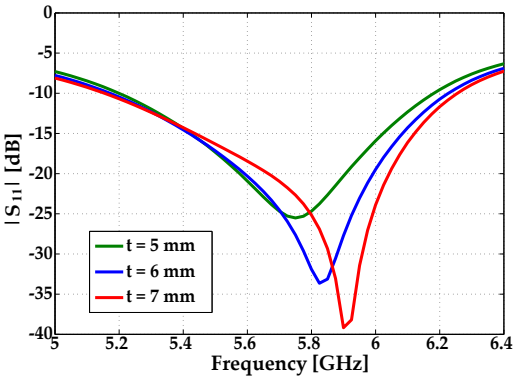


(c) Influence of the $t$ parameter

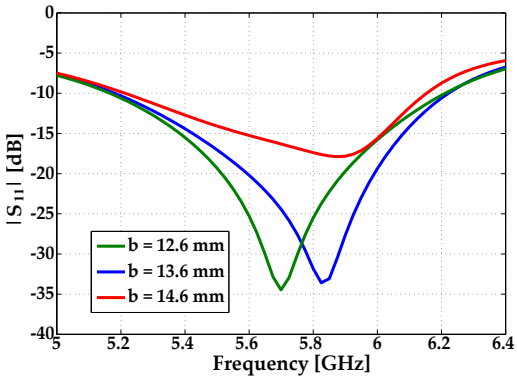


(d) Influence of the $b$ parameter

Figure 2.63: Return loss of CPW-fed double bow-tie antenna versus geometry dimensions.

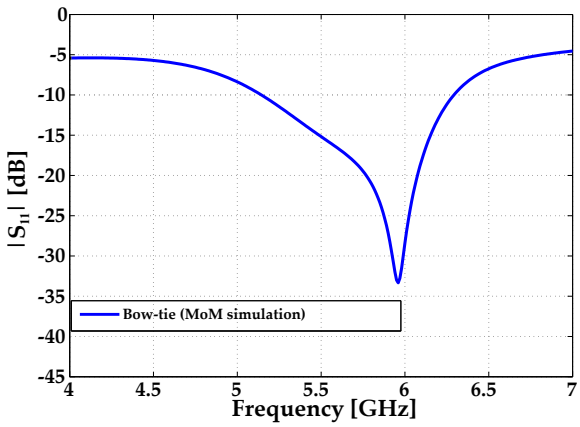


Figure 2.64: Simulated return loss of the CPW-fed double bow-tie antenna.

#### 2.4.1.2 Bow-tie-AMC Combination

Several ideas concerning the AMC arrangement with respect to the antenna have been considered. The first one is that the AMC would electromagnetically insulate the antenna from the metallic object without disturbing the antenna performance. However, as the CPW-fed slot double bow-tie antenna has no ground plane below the dielectric substrate, the AMC unit-cells below the antenna have been removed. The selected AMC arrangement in terms of a trade-off between performance and size is the one shown in Figure 2.65. The antenna is fixed to the AMC structure by a 0.1 mm double-sided non-conducting adhesive tape. The dimensions of the final structure, Bow-tie–AMC (see Figure 2.62), are $L_{\mathrm{p}}$= 57.60 mm and $W_{\mathrm{p}}$= 46.08 mm.

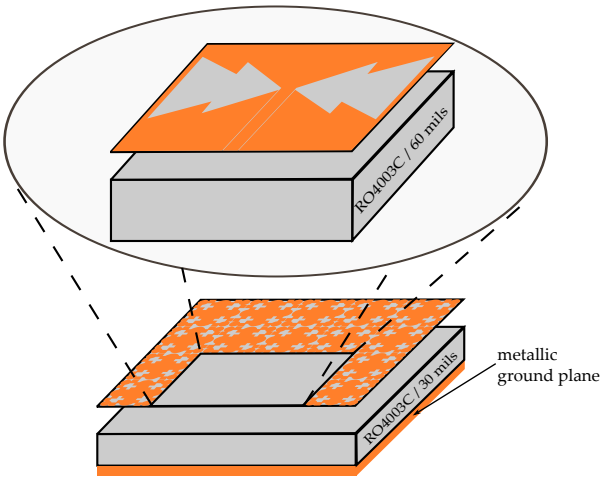


Figure 2.65: Bow-tie-AMC prototype layout.

#### 2.4.1.3 Measurement Results

Prototypes of the CPW-fed slot double bow-tie antenna and three different AMC unit-cells arrangements combined with the double bow-tie antenna (see Figure 2.67) Bow-tie–AMC, Bow-tie–AMC-#2, and Bow-tie–AMC-#3 have been manufactured. The return losses of each manufactured prototype have been measured. As it can be observed in Figure 2.66, the measured operating bandwidth of the CPW-fed slot double bow-tie antenna is 1.49 GHz (25.00%), which is wider than 1.15 GHz (20.10%) obtained in simulation. The difference in bandwidth could be due to the fact that the commercial MoM software considers infinite extension for the dielectric substrate or even more likely to manufacturing tolerances or to the variation of the relative permittivity with respect to its nominal value used in simulations.

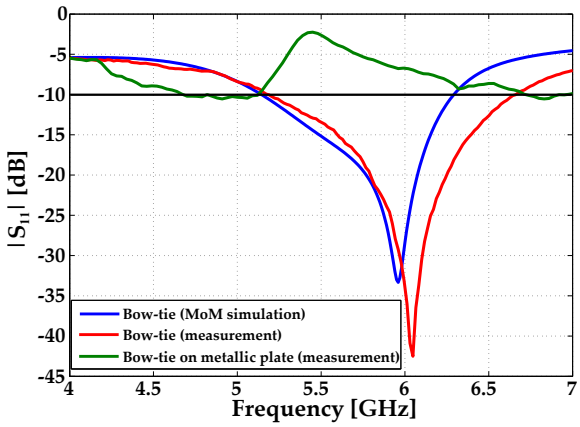


Figure 2.66: Return loss of the CPW-fed double bow-tie antenna.

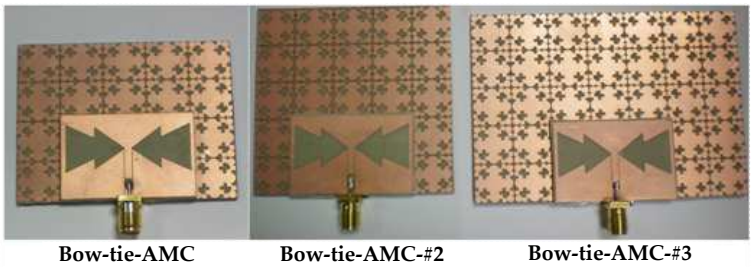


Figure 2.67: Different AMC unit-cells arrangements combined with the double bow-tie antenna: (Left to right) Bow-tie-AMC, Bow-tie-AMC-#2 and Bow-tie-AMC-#3.

When resonances of the bow-tie antenna and AMC unit-cells arrangement are combined, depending on the number of unit-cells in the AMC arrangement, the antenna resonance frequency is shifted down to a different extent. As it can be observed in Figure 2.68, compared to the prototype Bow-tie–AMC, the prototypes Bow-tie–AMC-#2 and Bow-tie–AMC-#3 lead to narrower bandwidths, and the resulting operation band is shifted downwards. Prototype Bow-tie–AMC-#2 is dismissed as it does not show optimal performance at 5.8 GHz. The performance of the Bow-tie–AMC-#3 prototype is proper for 5.8 GHz RFID applications, but it shows narrower bandwidth than prototype Bow-tie–AMC despite requiring larger size. Therefore, prototype Bow-tie–AMC is the one selected in terms of a trade-off between performance and size.

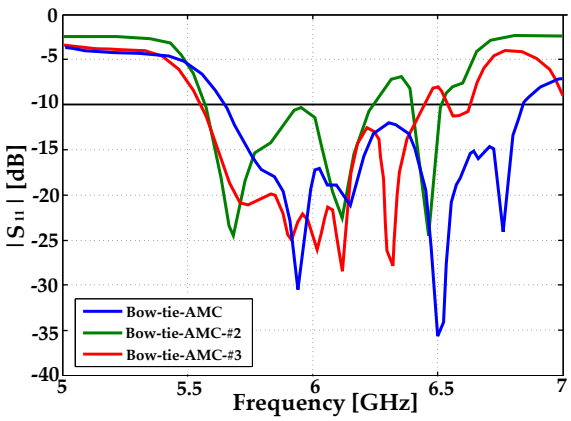


Figure 2.68: Measured return loss for the Bow-tie-AMC, Bow-tie-AMC-#2 and Bow-tie-AMC-#3 prototypes.

As it could be expected, when placed on a metallic plate, the antenna resonance frequency has been shifted out of the SHF RFID band, leading to its total malfunctioning (see Figure 2.66).

However, from Figure 2.69, it can be extracted that the Bow-tie–AMC combination keeps the antenna operating properly in the whole antenna bandwidth, even when placed on a metallic plate, as the AMC electromagnetically insulates the antenna from the metallic plate.

The measured return loss for the Bow-tie–AMC prototype shows two resonances: the first one is due to the joint operation of the antenna and the AMC since the AMC operation bandwidth starts at 5625 MHz (see Figure 2.8), whereas the second resonance is due to an antenna resonance out of the AMC operation bandwidth since there is an additional RO4003C metal-backed layer below the original antenna.

To show how the antenna current distribution is affected by the AMC, four

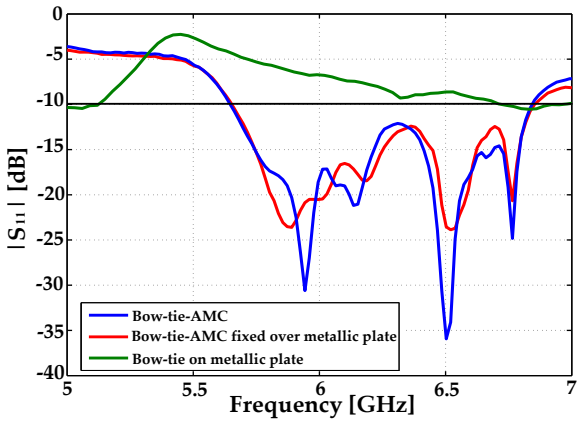


Figure 2.69: Measured return loss for the Bow-tie-AMC design and for the Bow-tie and Bow-tie-AMC designs on a metallic plate.

simulations at 5.8 GHz have been carried out, and the results are presented in Figure 2.70. The normalized surface current distribution on the bow-tie antenna alone shows that currents are mainly concentrated at the edges of the antenna's slots. Placing the antenna on a metallic plate (Figure 2.71), its current distribution varies due to antenna mismatch. When the bow-tie antenna is combined with the AMC (prototype Bow-tie–AMC), surface currents on the antenna are reduced. Finally, when the combined structure Bow-tie–AMC is placed on a metallic plate, the current distribution on the bow-tie is not affected, so it is possible to affirm that the AMC electromagnetically insulates the bow-tie antenna from the metallic plate.

Measured radiation pattern cuts in the E and H planes of each manufactured prototype are plotted in Figure 2.72 and Figure 2.73. Bow-tie–AMC prototype exhibits co-polarization–cross-polarization (CP–XP) ratio better than 20 dB. Radiation pattern properties of the Bow-tie–AMC for RFID application are still preserved even when placed on a metallic plate. In Table 2.9, the measured gain of each prototype is listed. The AMC increases the antenna gain. The obtained gain for the Bow-tie–AMC centered on a metallic plate (see Figure 2.71) agrees with theoretical justification of the 6 dB increase when image currents are constructively added. The measured radiation efficiency of the bow-tie antenna alone is 54% whereas by combining the antenna with the AMC the radiation efficiency obtained is 57%.

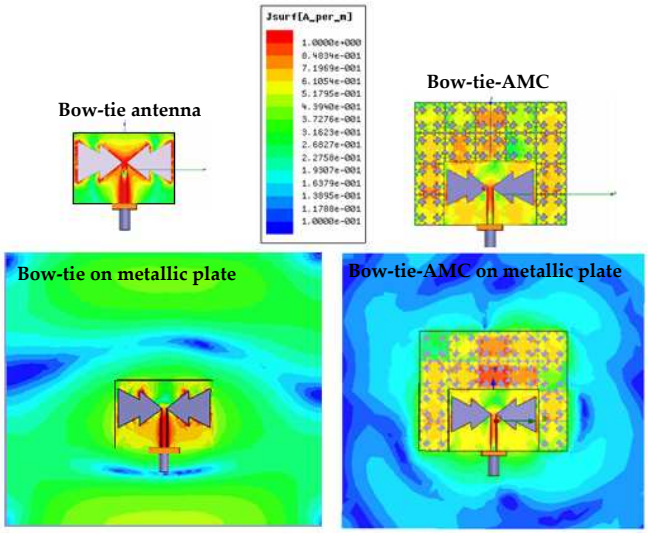


Figure 2.70: Simulated surface currents distribution (normalized).

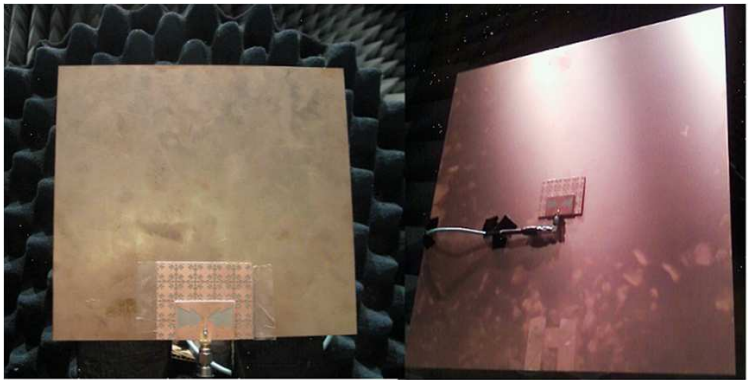

Figure 2.71: Measurement setup in anechoic chamber for Bow-tie-AMC at (Left) the edge and (Right) centered on a metallic plate.

| Prototype | Gain [dB] |
|---|---|
| Bow-tie | 2.7 |
| Bow-tie-AMC | 3.5 |
| Bow-tie-AMC on metallic plate | 6.1 |
| Bow-tie-AMC on metallic plate (centered) | 9.2 |

Table 2.9: Manufactured protototypes' gain.

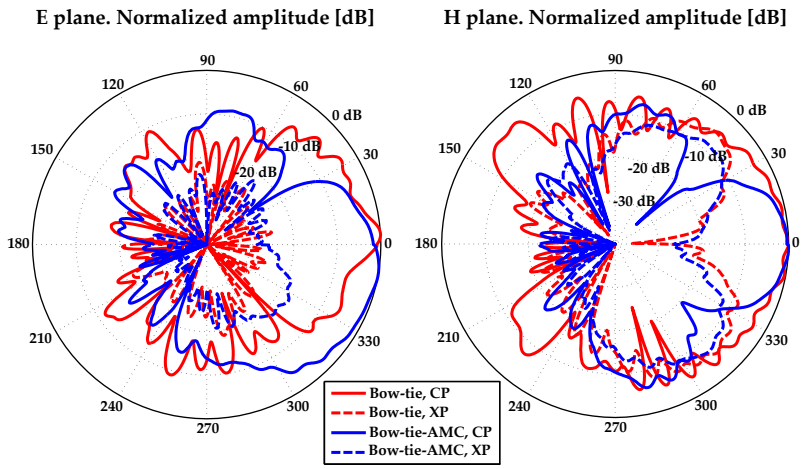


Figure 2.72: Bow-tie and Bow-tie-AMC measured radiation pattern (normalized in dB) (Left) E plane and (Right) H plane without metallic plane.

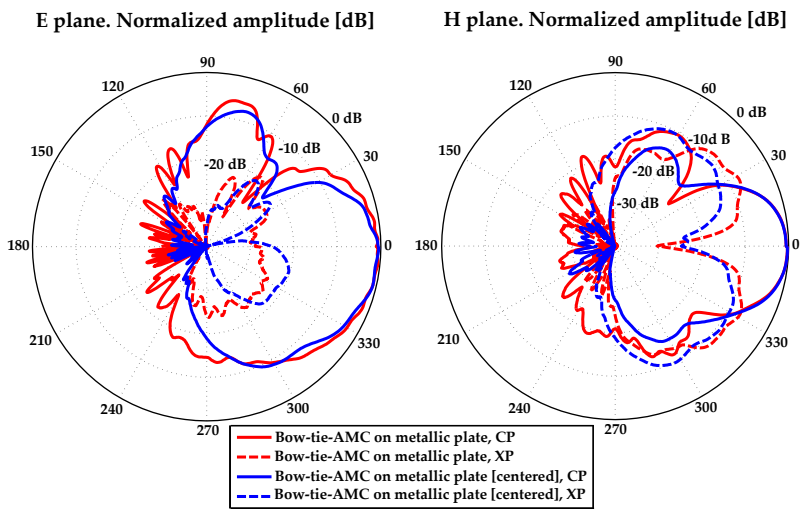


Figure 2.73: Bow-tie-AMC measured radiation pattern when placed on a metallic plate (normalized in dB) (Left) E-plane and (Right) H-plane.

### 2.4.2 Application in the 2.48 GHz SHF (Super High Frequency) RFID Band

#### 2.4.2.1 Antenna Design at 2.48 GHz

Furthermore, for the 2.48 GHz SHF band a slot antenna with coplanar feed line (CPW) using the conformable Rogers RO3003 dielectric (with relative dielectric permittivity $\varepsilon_r = 3$ , tan $\delta = 0.0013$, and a thickness $h = 0.762$ mm (30 mils)) has been designed . This antenna has a simple structure with only one layer of dielectric substrate and metallization. The antenna dimensions together with the simulated return loss are shown in Figure 2.74. The simulated operating bandwidth of the antenna (range of frequencies within $S_{11} \leq$ -10 dB) is 1.48 GHz (22.0%). The simulated antenna gain at 2.48 GHz is 2.9 dB with very small variation along the antenna bandwidth.

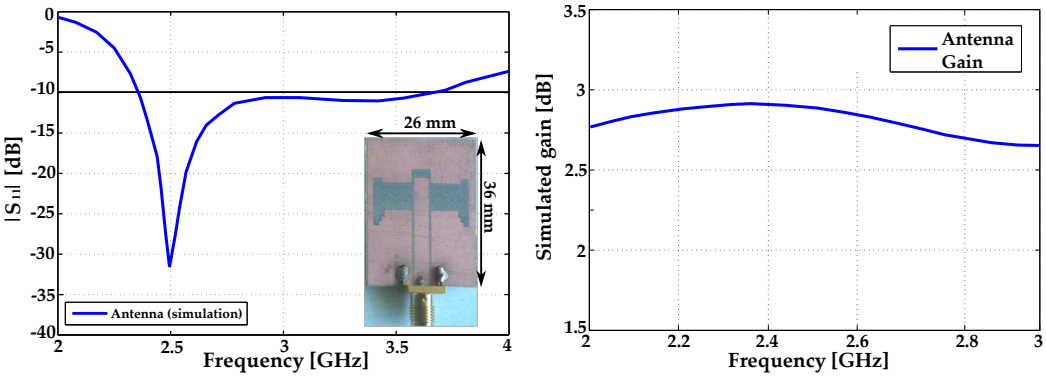


(a) Reflection coefficient of the antenna. Manufactured prototype.

(b) Simulated antenna gain.

Figure 2.74: Simulated antenna bandwidth and gain.

#### 2.4.2.2 Antenna-AMC Combination

The antenna has been combined with a 3×3 AMC unit-cell arrangement with an overall size of 93.6 × 93.6 mm$^2$. The unit-cell geometry designed in Section 2.1.1 is taken as reference for the antenna-AMC combination. By using a foam layer, the antenna is placed 3 mm away from the AMC structure (Figure 2.75). Hence the overall thickness of the antenna-AMC combination is 4.5 mm. The antenna's connector is not touching the AMC structures. The antenna dimensions haven´t been re-optimized for obtain resonance conditions at 2.48 GHz.

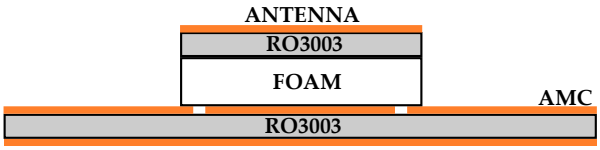


Figure 2.75: Antenna-AMC layout.

#### 2.4.2.3 Measurement Results

In Figure 2.76 the manufactured prototypes are shown. The comparison between the simulated and measured reflection coefficient for the antenna alone in free space is presented in Figure 2.77(a). As it can be observed the measured operating bandwidth of the antenna is 1.1 GHz (42%), which is about 19% narrower than 1.3 GHz (52%) obtained by employing electromagnetic simulations. The difference in bandwidth and the frequency shift could be due to manufacturing tolerances and also due to the variation of the relative permittivity with respect to the nominal value used in simulations.

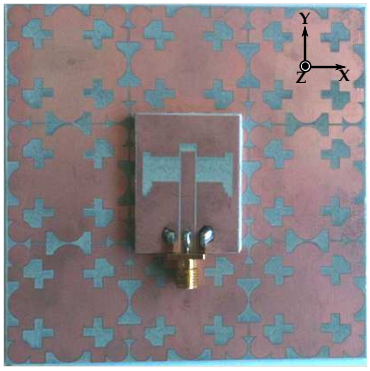


(a) Antenna-AMC

(b) Antenna-AMC surrounding a metallic can

Figure 2.76: Manufactured prototypes.

After loading the antenna with the 3x3 AMC unit-cell arrangement, the operational bandwidth strongly decreases. The AMC has a narrow bandwidth which means the quality factor of the AMC structure is higher compared to the antenna´s. Therefore, the combined prototype presents a compressed bandwidth around the resonance frequency 2.48 GHz. It can be noted also that when the antenna-AMC surrounds the metallic can, the AMC will electromagnetically insulate the antenna from the metallic object without loosing functionality.

Apart from the good performance next to metallic environments, an obvious

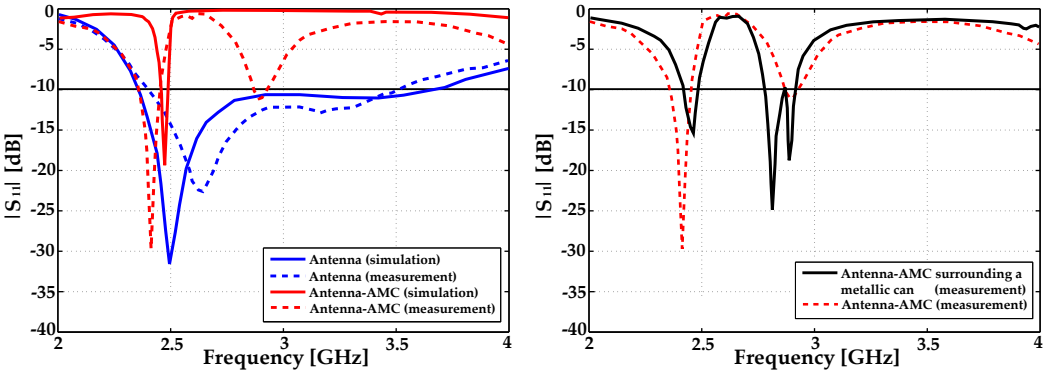


(a) Antenna alone and antenna-AMC (b) Antenna-AMC near metallic objects

Figure 2.77: Reflection coefficient of the prototypes.

improvement obtained can be seen from the antenna-AMC radiation patterns diagrammed in Figure 2.78. The main lobe becomes more directive in both E and H planes when the AMC structure is used. Moreover, the simulated gain of the antenna over the 3x3 unit-cells array attains 7.3 dB; 4.4 dB enhancement if compared with the antenna alone, whereas the directivity increases from 3.1 dB to 7.8 dB. The directivity could be further enhanced by using more unit-cells. Unfortunately, more resources concerning the computational tools are needed to simulate such structure with high accuracy.

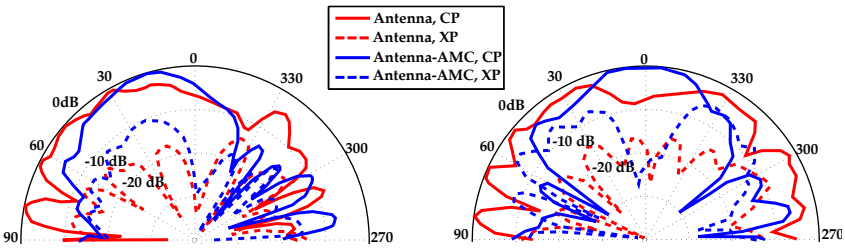


Figure 2.78: Antenna and antenna-AMC measured radiation pattern (normalized in dB) (Left) E-plane and (Right) H-plane.

| Prototype | Gain (dB) | Directivity (dB) | Radiation efficiency (%) |
|---|---|---|---|
| Antenna | 2.7 | 4 | 50 |
| Antenna-AMC | 3.5 | 5.8 | 49 |

Table 2.10: Measured gain, directivity and radiation efficiency of the manufactured prototypes.

### 2.4.3 Application in the 868 MHz UHF (Ultra High Frequency) RFID Band

#### 2.4.3.1 Dipole Design at 868 MHz

The proposed configuration of the dipole antenna (henceforth referenced as Dipole), suitable for RFID tags at 868 MHz, is depicted in Figure 2.79. Two folded wires (vertical and horizontal stubs) are used to replace the straight wires of a conventional half-wavelength ($\lambda_0/2$) dipole antenna in order to shorten the physical length of the design. The symmetrical dipole antenna is printed on a thin bendable dielectric substrate (RO3003) with a relative dielectric constant $\varepsilon_r = 3$, $\tan\delta = 0.0013$ and thickness $h = 0.762$ mm with 18 µm copper cladding.

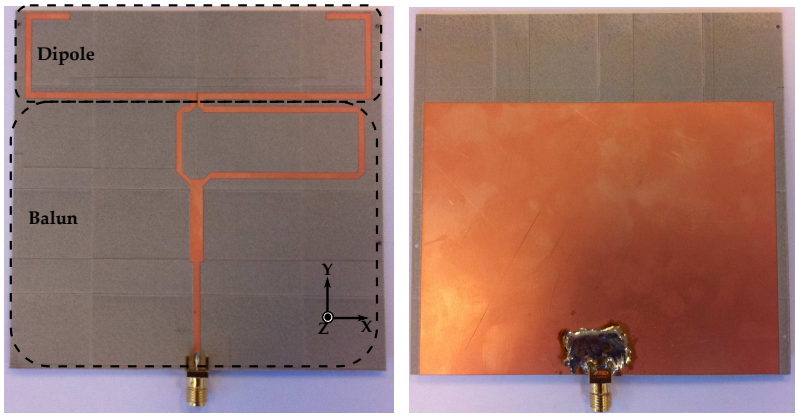


Figure 2.79: Geometry of the proposed dipole antenna (top view and bottom view) fed using a balance to unbalance (balun) transition.

For the presented dipole antenna, the resonance frequency and bandwidth are mainly set by the geometry parameters: dipole length $L$, folded horizontal stub length $T$ and folded vertical stub length $W$. Although the frequency of interest is 868 MHz, the dipole antenna has been designed at a lower frequency; more exactly

at 845 MHz.

In measurements, according to previous results obtained using RO3003 substrate, the resonance frequency tends to shift upwards due to manufacturing tolerances and also due to the variation of the relative dielectric permittivity with respect to its nominal value used in simulations. Moreover, the slight frequency shift expected in measurements could also be due to the commercial MoM software which considers the substrate layers infinite. In this way, by designing the dipole antenna at a lower frequency, the 868 MHz frequency of interest can be covered in measurements.

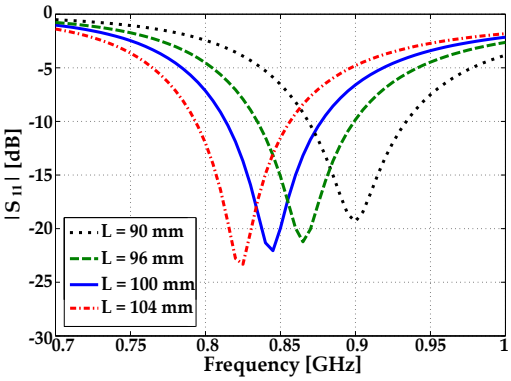


(a) Influence of the $L$ parameter

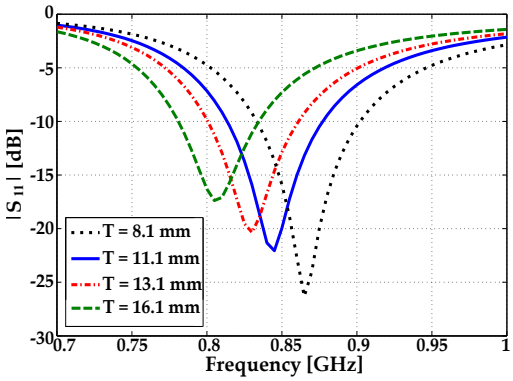


(b) Influence of the $T$ parameter

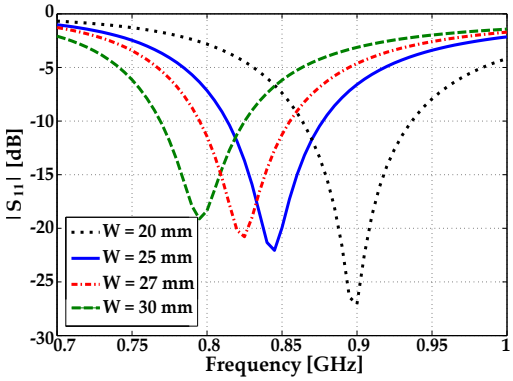


(c) Influence of the $W$ parameter

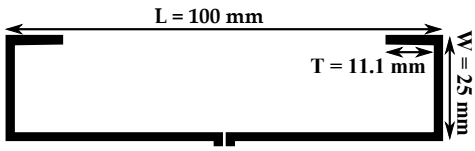


(d) Layout of the dipole antenna

Figure 2.80: Simulated return loss of the dipole antenna without balun versus geometry parameters.

A parameter sweep is performed in simulations and the final optimized parameters of the dipole antenna are shown in Figure 2.80. Only one parameter is change at each time during the analysis. The dipole antenna length $L$ controls the resonance frequency (increasing $L$ shifts the operating band to a lower frequency range while the operational bandwidth is maintained and the matching is improved). The

antenna's resonance frequency rises when both $W$ and $T$ decrease, the bandwidth becomes broader and at the same time, the matching improves.

In order to be able to measure the dipole antenna via coaxial cable a balance-to-unbalance transformer (balun) is used. Many approaches for balun realizations are reported in literature [33, 53]. In this Doctoral Thesis, the balun is printed on the same layer as the dipole antenna shown in Figure 2.79. The balun must introduce a 180° phase delay between the two microstrip line branches of 50 Ω. To obtain the required phase delay the difference in length of the two branches at the center frequency is approximately $\lambda_g/2$ (being $\lambda_g$ the guided wavelength at 868 MHz). Between the 50 Ω input microstrip line and the two branches, a $\lambda_g/8$ transformer is introduced to refine the matching of the prototype. Even if the balun is quite large (due to the low relative dielectric permittivity of the substrate), it is not part of the dipole antenna and it can be considered an external module used just for measurement purposes.

From Figure 2.81, where the simulated return loss is shown, it can be observed that the dipole antenna with and without balun have the same resonance frequency 845 MHz, a proper matching impedance and almost the same operational bandwidth (5.3%).

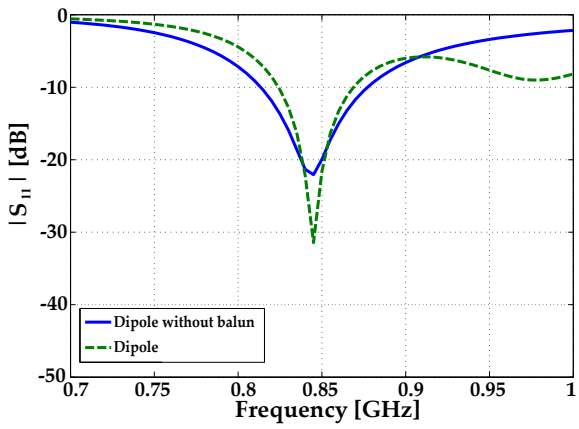


Figure 2.81: Return loss of the Dipole antenna in simulations.

In the vicinity of conductors, the dipole antenna parameters such as the input impedance, bandwidth, radiation pattern or gain vary. The overall efficiency seriously degrades due to the variation of the reactive part of the antenna's impedance and also due to the significant amount of electromagnetic energy that is trapped between the antenna and metallic surface. These problems can be overcome by using the AMC structure [23, 30, 54].

#### 2.4.3.2 Dipole-AMC Combination

The unit-cell geometry designed in Section 2.1.1 is taken as reference for the Dipole-AMC combination. The dielectric substrate used for printing the AMC is RO3010. The simulated reflection phase of the AMC structure is depicted in Figure 2.7. The AMC operational bandwidth is 1.7% at 868 MHz center frequency.

Once the dipole antenna and AMC are designed, the combination of both structures has been considered. A 3x1 arrangement of AMC unit-cells (147.6 x 49.2 mm$^2$) is placed below the dipole antenna (without considering the balun) with the purpose of electromagnetically insulating the dipole antenna from metallic objects/human body without disturbing its performance (in this way the dipole becomes tolerant to positioning on the body/metallic objects). A 0.1 mm double sided non-conducting adhesive tape is used to fix the dipole antenna to the AMC structure (see Figure 2.82).

It is worth mentioning that no additional materials like foam were used. In simulations, considering the Dipole without balun-AMC design, a 2.9 dB improvement in terms of gain is achieved by including the AMC structure.

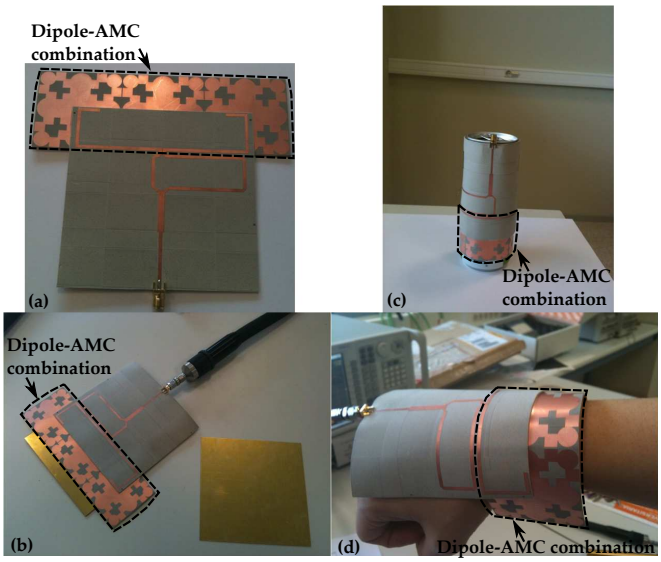


Figure 2.82: Manufactured prototypes. (a) Dipole-AMC. (b) Dipole-AMC fixed over a metallic plate. (c) Dipole-AMC bent and surrounding a metallic can. (d) Dipole-AMC conformed around the human wrist.

#### 2.4.3.3 Measurement Results

Laser micro-machining is used to manufacture the prototypes of the Dipole and Dipole-AMC combination in order to validate the simulation results. The prototypes are characterized in terms of return loss using an Agilent PNA-X series N5247A vector network analyzer while the radiation pattern measurements are performed in the anechoic chamber.

As it can be observed in Figure 2.83, the measured operating bandwidth of the Dipole prototype is 42 MHz (4.9%) at the center frequency of 868 MHz, in good agreement with the simulated bandwidth.

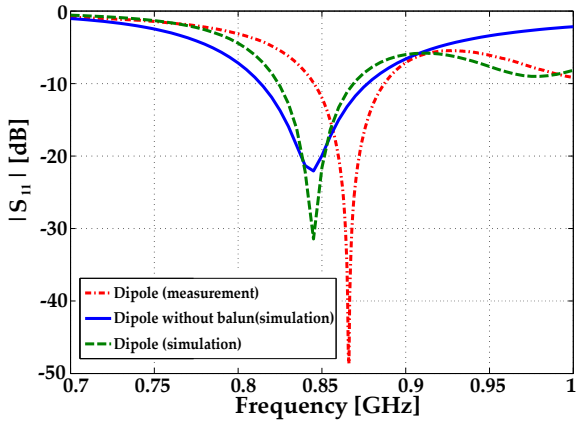


Figure 2.83: Return loss of the Dipole antenna.

When the resonances of the dipole antenna and the AMC unit-cell arrangement combine, the bandwidth of the resulting prototype (Dipole-AMC) becomes narrower. This phenomenon occurs due to the higher quality factor of the AMC compared to the dipole's. Even with narrower bandwidth, the Dipole-AMC combination still works properly for the 868 MHz UHF RFID band (see Figure 2.84). The design can be easily bent, worn as an accessory (bracelet for example) or even integrated into clothing.

As it could be expected, when placed on a metallic plate or conformed around the human wrist, the resonance frequency of the Dipole prototype shifts out of the 868 MHz UHF RFID band, leading to its total malfunctioning.

However, from measurement results in Figure 2.85, the Dipole-AMC prototype works reliably even when placed on a metallic plate or being bent and surrounding a metallic can (see Figure 2.82(c), radius of the metallic can equals to 2.7 cm), as the AMC electromagnetically insulates the dipole from metallic objects. By surrounding the metallic can, the aperture of the Dipole-AMC is reduced compared to the flat

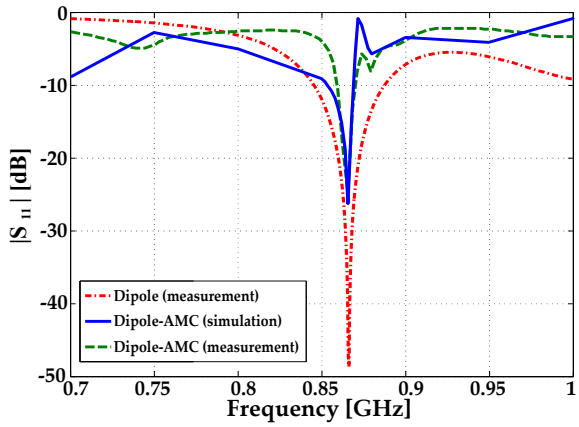


Figure 2.84: Return loss of the Dipole-AMC prototype.

non-deformed Dipole prototype, making the resonance frequency to shift upwards approximately 2% and worsening the matching.

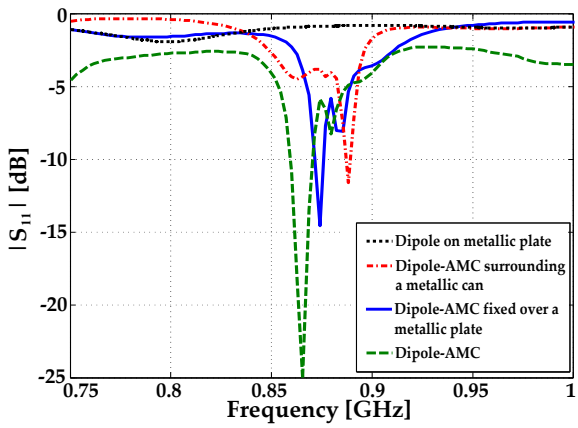


Figure 2.85: Influence of the metallic can/plate on the return loss of the Dipole-AMC prototype in measurements.

Moreover, there are applications where the AMC structure is used to avoid the Dipole antenna's impedance mismatch caused by the proximity to human tissue and to insulate the user's body from undesired exposure to electromagnetic radiation.

Figure 2.86 presents the comparison between the measured return loss of the Dipole-AMC prototype conformed around the human wrist (see Figure 2.82(d)) and Dipole-AMC bent prototype measured in free space. The resonance frequency of the Dipole-AMC conformed around the wrist shifts upwards 1.3%. Nonetheless, at 868 MHz, the return loss remains under -6 dB. The prototype's resonance could

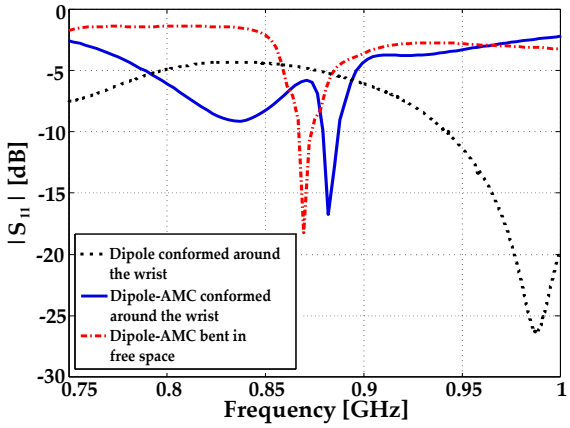


Figure 2.86: Measured return loss of the Dipole-AMC prototype conformed around the wrist and Dipole-AMC prototype bent in free space.

be adjusted (by slightly shifting downwards its resonance frequency) in order to operate at 868 MHz for this specific application. The matching of the Dipole-AMC conformed around the wrist is improved compared to the one that surrounds the metallic can because of a less stressful degree of bending to which the prototype is exposed, so the reflection coefficient decreases.

The measured far field radiation patterns in the XZ cut (E-plane) and YZ cut (H-plane) of each manufactured prototype are shown in Figure 2.87 and Figure 2.88. The AMC preserves the co-polarization - cross-polarization (CP-XP) ratio of the dipole antenna. When the prototypes are bent (Dipole and Dipole-AMC) the CP-XP ratio decreases to approximately 10 dB. In addition, general dipole-like radiation pattern in the E-plane and nearly omnidirectional radiation in H-plane are observed.

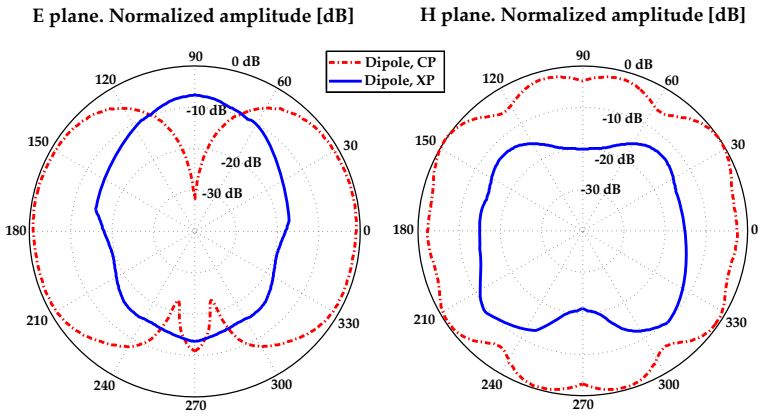


(a) Flat Dipole prototype

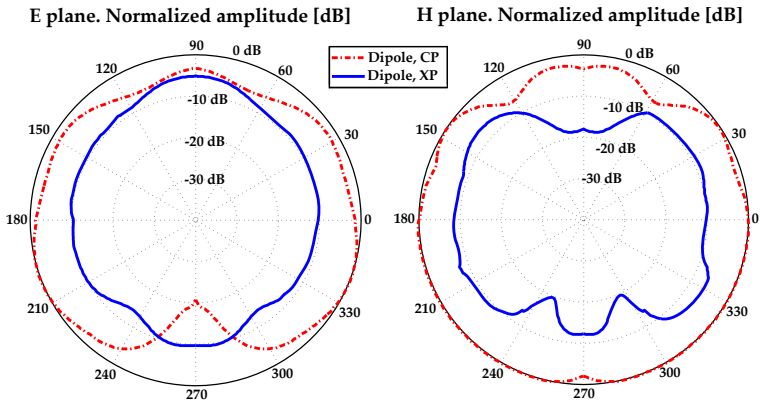


(b) Bent Dipole prototype

Figure 2.87: Dipole measured radiation pattern (normalized, in dB) in the E-plane and H-plane at 868MHz.

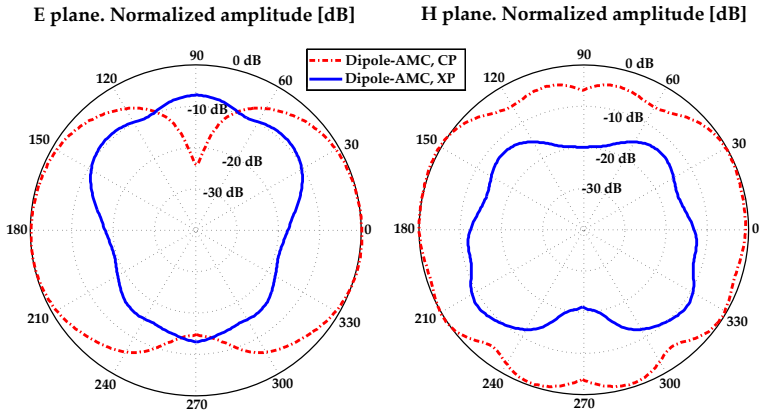


(a) Flat Dipole-AMC prototype

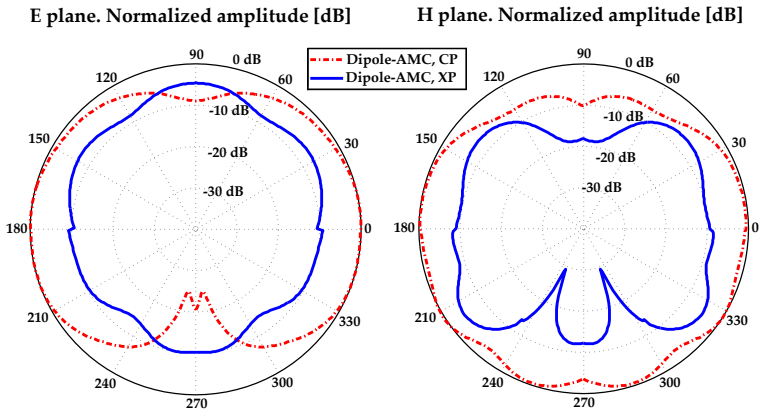


(b) Bent Dipole-AMC prototype

Figure 2.88: Dipole-AMC measured radiation pattern (normalized, in dB) in the E-plane and H-plane at 868MHz.

Radiation properties in terms of peak realized gain, directivity and efficiency are compared in Table 2.11.

In measurements, by using the AMC combined with the antenna, the directivity is enhanced, whereas the peak realized gain is slightly reduced (due to the influence of the balun's ground plane). It should be noted that the directivity could be further increased if more AMC unit-cells were used. However this solution leads to larger design. Therefore, a trade-off solution between the size of the prototype and radiation properties has to be adopted. Regarding the measurements of the bent Dipole, the directivity is preserved while the peak realized gain diminishes compared to the flat Dipole prototype. The same phenomena happen for the Dipole-AMC bent prototype. However, as a reward for the slight radiation efficiency reduction, the dipole antenna operates on metallic objects and in on-body applications.

| Prototype | Gain [dB] | Directivity [dB] | Rad. Eff. [%] |
|---|---|---|---|
| | Sim./Mea. | Sim./Mea. | Sim./Mea. |
| Dipole without balun | 1.7/- | 2/- | 93/- |
| Dipole without balun-AMC | 4.6/- | 4.8/- | 95/- |
| Dipole | 2.6/1.6 | 2.8/2.7 | 95/78 |
| Dipole-AMC | 1.9/1 | 4.3/3.6 | 57/55 |
| Dipole* | -/-0.5 | -/2.9 | -/46 |
| Dipole-AMC* | -/0.5 | -/4.1 | -/44 |
| * Under bent conditions in free space | | | |

Table 2.11: Gain, directivity and radiation efficiency of the prototypes.

## 2.5 Conclusions

The designs of a 5.8 GHz AMC as well as a 6.2 GHz miniaturized polarization dependent AMC and a 6.2 GHz / 10.5 GHz miniaturized dual band polarization insensitive AMC have been presented. All the prototypes have been manufactured and characterized based on reflection coefficient phase. The three designs show proper AMC operation bandwidth and a simulated angular margin of stability higher than ±40°. The 5.8 GHz AMC and the 6.2 GHz / 10.5 GHz miniaturized dual band AMC show polarization angle independency. The miniaturization was obtained by using interdigital capacitors. The complexity in the fabrication process is reduced since no via holed were needed.

Moreover, a flexible AMC with two different bending patterns has been presented together with the equivalent circuit model of the 6.2 GHz miniaturized polarization

dependent AMC. Design guidelines based on a compressive parametric study involving various design parameters of the AMC have been discussed and have been verified by comparing the calculated reflection phase with the full-wave simulation results.

The 5.8 GHz AMC was combined with a bow-tie antenna exhibiting proper operation both alone and when placed on a metallic plate. The gain resulted enhanced and the radiation pattern preserved when placed on a metallic plate. By scaling the 5.8 GHz AMC and using a different antenna, the electromagnetic properties of the resulted prototype in the 2.4 GHz frequency band has been shown. Furthermore, a dipole-AMC combination at 868 MHz has been conformed around a human wrist. The AMC avoids the antenna's impedance mismatch caused by the proximity to human tissue and insulate the user´s body from undesired exposure to electromagnetic radiation.

# Bibliography


[1] F. Yang and Y. Rahmat-Samii, "Electromagnetic Band-Gap Structures in Antenna Engineering," Cambridge, U.K, Cambridge Univ. Press, 2008.

[2] D. Sievenpiper et al., "High-impedance electromagnetic surfaces with a forbidden frequency band," IEEE Trans. Microw. Theory Tech., vol. 47, no. 11, pp. 2059–2074, 1999.

[3] D. J. Kern, D. H. Werner, A. Monorchio, L. Lanuzza, and M. J. Wilhelm, "The design synthesis of multiband artificial magnetic conductors using high impedance frequency selective surfaces," IEEE Trans. Antennas Propag., vol. 53, no. 1, pp. 8–17, 2005.

[4] M. Mantash, M.E. de Cos, A. Tarot, S. Collardey, K. Mahdjoubi, F. Las-Heras, "Dual-band textile hexagonal artificial magnetic conductor for WiFi wearable applications," 6th European Conference on Antennas and Propagation, pp. 1395-1398, 2012.

[5] J. R. Sohn, K. Y. Kim, H.-S. Tae, "Comparative Study On Various Artificial Magnetic Conductors For Low-Profile Antenna," Progress In Electromagnetics Research, vol. 61, pp. 27–37, 2006.

[6] S. E. Melais, T.M. Weller, "A Multilayer Jerusalem Cross Frequency Selective Surface," Wireless and Microwave Tech. Conference, 2009.

[7] N.Christopoulos, et al, "Metamaterials With Multiband AMC And EBG Properties," Proc. European Microwave Conference, 2005.

[8] M.A. Hiranandani, A.B. Yakovlev and A.A. Kishk, "Artificial magnetic conductors realised by frequency-selective surfaces on a grounded dielectric slab for antenna applications," IEE Proc.Microw. Antennas Propag., vol. 153, no. 5, pp. 487-493, 2006.

[9] S. Genovesi, R. Mittra, A. Monorchio, and G. Manara, "Particle swarm optimization of frequency selective surfaces for the design of artificial magnetic conductors," Proc. IEEE AP-S Int. Symp., pp. 3519–3522, 2006.

[10] C.R. Simovski, P. de Maagt, S.A. Tretyakov, M. Paquay and A.A. Sochava, "Angular stabilisation of resonant frequency of artificial magnetic conductors for TE-incidence," Elect. Let., vol. 40, no.2, pp. 92-93, 2004.

[11] P. Kovacs, Z. Raida, M. Martinez Vazquez, "Parametric study of mushroom-like and planar periodic structures in terms of simultaneous AMC and EBG properties," Radioengineering, vol. 17, no. 4, pp. 19-24, 2008.

[12] A. P. Feresidis, G. Goussetis, S. Wang, and J. C. Vardaxoglou, "Artificial magnetic conductor surfaces and their application to low profile highgain planar antennas," IEEE Trans. Antennas Propag., vol. 53, no. 1, pp. 209–215, 2005.

[13] Ansoft HFSS, from Ansoft Corporation, Four Station Square Suite 200, Pittsburgh, PA 15219.

[14] F. H. M. Faisal, J. Z. Kaminski, "Floquet-Bloch theory of high-harmonic generation in periodic structures," Physical Review A, vol. 56, no. 1, pp. 748-762, 1997.

[15] De Cos, M. E., F. Las-Heras, and M. Franco, "Design of planar artificial magnetic conductor ground plane using frequency selective surfaces for frequencies below 1 GHz," IEEE Antennas and Wireless Propagation Letters, vol. 8, pp. 951-954, 2009.

[16] Zheng, Q.-R., Y.-M. Yan, X.-Y. Cao, and N.-C. Yuan, "High impedance ground plane (HIGP) incorporated with resistance for radar cross section (RCS) reduction of antenna," Progress In Electromagnetics Research, vol. 84, pp. 307-319, 2008.

[17] Engheta, N., "Thin absorbing screens using metamaterial surfaces," IEEE Antennas and Propag. Society International Symp., vol. 2, pp. 392-395, 2002.

[18] M. E. de Cos, Y. Alvarez-Lopez, and F. Las Heras Andres, "A Novel Approach for RCS Reduction Using a Combination of Artificial Magnetic Conductors, Progress In Electromagnetics Research," vol. 107, pp. 147-159, 2010.

[19] S. Zhu, and R. Langley, "Dual-band wearable textile antenna on an EBG substrate," IEEE Trans. on Antennas and Propag., vol. 57, no. 4, pp. 926-935, 2009.

[20] P. Salonen, and Y. Rahmat-Samii, "Textile antennas: Effects of antenna bending on input matching and impedance bandwidth," IEEE Aerospace Electronic Systems Magazine, vol. 22, no. 3, pp. 10-14, 2007.

[21] H.R. Raad, A.I. Abbosh, H.M. Al Rizzo and G. Rucker, "Flexible and compact AMC based antenna for telemedicine applications", IEEE Transactions on antennas and propagation, vol. 61, no. 2, pp. 524-531, 2013.

[22] J.C. Vardaxoglou, G. Gousetis and A.P. Feresidis, "Miniaturization schemes for metallodielectric electromagnetic bandgap structures," IET Microw. Antennas Propag., vol. 1, no. 1, pp. 234 – 239, 2007.

[23] R.C. Hadarig, M.E. de Cos Gomez, Y. Alvarez, F. Las-Heras, "Novel Bowtie–AMC Combination for 5.8-GHz RFID Tags Usable with Metallic Objects," IEEE Anten Wirele Propag. Lett., vol. 8, pp. 1217- 1220, 2010.

[24] J. McVay and N. Engheta, "High impedance metamaterial surfaces using Hilbert-curve inclusions," IEEE Microw. Wireless Components Lett., vol. 14, no. 3, pp. 130–132, 2004.

[25] H. Liu, K.L. Ford and R.J. Langley, "Miniaturized artificial magnetic conductor design using lumped reactive components," Electronics Letters, vol.45, no.6, 2009.

[26] M.K. Taher Nuaimi, W.G.Whittow, "Novel Planar AMC for Low Profile Antenna Applications," Loughborough Antennas & Propag.Conf., 2009.

[27] Qi. Luo, H. M. Salgado, A. M. Moura, J. R. Pereira, "Dual-Band Antenna Design Using an EBG Artificial Magnetic Conductor Ground Plane," Loughborough Antennas & Propagation Conference, 2008.

[28] Y. Kim, F. Yang, and A. Z. Elsherbeni, "Compact Artificial Magnetic Conductor Designs Using Planar Square Spiral Geometries," Progress In Electromagnetics Research, vol. 77, pp. 43–54, 2007.

[29] M. Hosseini, A.Pirhadi, M. Hakkak, "Design of a novel AMC with little sensitivity to the angle of incidence and very compact size," Antennas and Propag. Society International Symposium, pp. 1939-1942, 2006.

[30] R.C Hadarig, M.E. de Cos, F. Las-Heras, "On the bandwidth enhancement of patch antenna using EBG/AMC structures," 6th European Conference on Antennas and Propagation (EUCAP), 2012

[31] N. Engheta and W. Ziolkowski, "Metamtamaterials, Physics and Engineering Explorations," John Wiley & Sons, 2006.

[32] J. McVay, A. Hoorfarl and N. Engheta, "Bandwidth Enhancement and Polarization Dependence Elimination of Space-filling Curve Artificial Magnetic Conductors," Proceedings of Asia-Pacific Microwave Conference 2007.

[33] C. A. Balanis, "Antenna Theory: Analysis and Design," 2$^{nd}$ ed. New York, NY, USA: Wiley, 1997.

[34] Y. Li et al., "Prototyping dual-band artificial magnetic conductors with laser micromachining," in Proc. WARS2006 Conf., Leura, NSW, Australia, 2006.

[35] M. E. de Cos, Y. Álvarez, and F. Las-Heras, "Planar artificial magnetic conductor: Design and characterization setup in the RFID SHF band," J. Electromagn. Waves Antennas, vol. 23, pp. 1467–1478, 2009.

[36] C.R. Simovski, P. de Maagt, and I. Melchakova, "High-impedance surface having stable resonance with respect to polarization and incident angle," IEEE Trans. Antennas Propag., vol. 53, no.3, pp. 908-914, 2005.

[37] M. Hosseinipanah, and Q. Wu, "Equivalent Circuit Model for Designing of Jerusalem Cross-Based Artificial Magnetic Conductors," Radioengineering, vol. 18, no. 4, pp. 544-550, 2009.

[38] O. Luukkonen, C. R. Simovsky, G. Granet, G. Goussetis, D. Lioubtchenko, A. Raisanen, and S. A. Tretyakov, "Simple and accurate analytical model of planar grids and high-impedance surfaces comprising metal strips," IEEE Trans. Antennas Propagat., vol. 56, no. 6, pp. 1624-1632, 2008.

[39] D. Ramaccia, F. Bilotti, and A. Toscano, "Analytical model of a metasurface consisting of a regular array of subwavelenght circular holes in a metal sheet," Progress In Electromagnetics Research M, vol. 18, pp. 209-219, 2011.

[40] L. Bilotti, A. Toscano, L. Vegni, K. B. Alici, K. Aydin, and E. Ozbay, "Equivalent circuit models for the design of metamaterials based on artifcial magnetic inclusions," IEEE Trans. Microw. Theory Tech., vol. 55, pp. 2865-2873, 2007.

[41] O. Luukkonen; F. Costa; C.R. Simovski; A. Monorchio; S.A. Tretyakov, "A Thin Electromagnetic Absorber for Wide Incidence Angles and Both Polarizations," IEEE Trans. on Antennas and Propagation, vol.57, no.10, pp.3119-3125, Oct. 2009.

[42] I. Bahl, "Lumped Elements for RF and Microwave Circuit," Norwood, Artech House, (2003).

[43] C.L. Holloway, and E.F. Kuester, "Net and partial inductance of a microstrip ground plane," IEEE Trans. Electromagn. Compat, vol. 49, pp. 33-46, 1998.

[44] K.C. Gupta, R. Garg, I. Bahl, and P. Bhartia, "Microstrip Lines and Slotlines", 2nd ed. Norwood: Artech House, 1996.

[45] D. M. Dobkin and S. M. Weigand, "Environmental effects on RFID tag antennas," in IEEE Microw. Symp. Dig., pp. 135–138, 2005.

[46] R. Clarke, D. Twede, J. R. Tazelaar, and K. K. Boyer, "Radio frequency identification (RFID) performance: The effect of tag orientation and package contents," Packag. Technol. Sci., vol. 19, no. 1, pp. 45–54, 2006.

[47] K. V. Seshagiri Rao, P. V. Nikitin, and S. F. Lam, "Antenna design for UHF RFID tags: A review and a practical application," IEEE Trans. Antennas Propag., vol. 53, no. 12, pp. 3870–3876, 2005.

[48] S. R. Aroor and D. D. Deavours, "Evaluation of the state of passive UHF RFID: An experimental approach," IEEE Syst. J., vol. 1, no. 2, pp. 168–176, 2007.

[49] E. A. Soliman, S. Brebels, P. Delmotte, G. A. E. Vandenbosch, and E. Beyne, "Bow-tie slot antenna fed by CPW," Electron. Lett., vol. 35, no. 7, pp. 514–515, 1999.

[50] J.-W. Niu and S.-S. Zhong, "A CPW-fed broadband slot antenna with linear taper," Microw. Opt. Technol. Lett., vol. 41, no. 3, pp. 218–221, 2004.

[51] Y. L. Chen, C.-L. Ruan, and L. Peng, "A novel ultra-wideband bow-tie slot antenna in wireless communication systems," Prog. Electromagn. Res. Lett., vol. 1, pp. 101–108, 2008.

[52] ADS Momentun EM Simulation Tool, Agilent Technologies, Santa Clara, CA, 2008 [Online]. Available: www.agilent.com/find/eesof

[53] W. R. Deal, N. Kaneda, J. Sor, Y. Qian, and T. Itoh, "A new quasi-Yagi antenna for planar active antenna arrays," IEEE Trans. Microw. Theory Tech., vol. 48, no. 6, pp. 910–918, 2000.

[54] L. Akhoondzadeh-Asl, D. J. Kern, P. Hall, and D. Werner, "Wideband dipoles on electromagnetic bandgap ground planes," IEEE Trans. Antennas Propag., vol. 55, no. 9, pp. 2426–2434, 2007.

# Chapter 3

# Electromagnetic Band-Gap (EBG) Structures

Contents


**3.1 Fundamental Concepts and Characterization of EBG Structures . . . . . 109**

3.1.1 5.8 GHz Electomagnetic Band-Gap Design . . . . . 113

3.1.2 Polarization Dependent Electromagnetic Band-Gap Design 118

3.1.3 Polarization Insensitive Electromagnetic Band-Gap Design 119

**3.2 Characterization and Measurement Results Using the Suspended Microstrip Method . . . . . 120**

3.2.1 5.8 GHz Electromagnetic Band-Gap Design . . . . . 120

3.2.2 Polarization Dependent Electromagnetic Band-Gap Design 121

3.2.3 Polarization Insensitive Electromagnetic Band-Gap Design 122

**3.3 EBGs Applied to Antennas . . . . . 123**

3.3.1 Bandwidth Enhancement of Patch Antennas . . . . . 123

**3.4 EBGs Applied to Filters . . . . . 132**

3.4.1 Band-Pass Filter . . . . . 132

**3.5 Conclusions . . . . . 142**


## 3.1 Fundamental Concepts and Characterization of EBG Structures

Electromagnetic Bandgap (EBG) structures have been studied over the last few years for microwave applications. Their function is to control and manipu-

late the propagation of electromagnetic (EM) waves. An important parameter to describe the propagation property of electromagnetic waves is the wavenumber $k$. The wavenumber $k$ represents the change in phase along the path traveled by the wave at any instant.

For surface waves propagating in a dielectric slab or an EBG structure, it is usually difficult to give an expression for the wavenumber $k$. One has to either solve an eigen-value equation or perform a full wave simulation to determine the wavenumber. It is important to point out that the solution of an eigen-value equation may not be unique. In another words, there may exist several different propagation constants at the same frequency. Each one is known as a specific mode. The relation between the wavenumber $k$ and frequency is often plotted out and referred to as the dispersion diagram. Since periodic structures are involved, only the dispersion diagram for one unit-cell is needed to characterize the entire structure.

The dispersion diagram presents propagating modes and band gaps (frequency bands where the propagation is not allowed) that can potentially exist between such modes [1]. Brillouin, in his theory of wave propagation in periodic structures [2], states that for any periodic structure there are certain vectors (i.e. directions) in the unit-cell that constitute a boundary region of propagation called irreducible Brillouin zone. According to this theory, deriving the propagating modes in the direction of these vectors is sufficient to cover all the possible direction of propagation within the lattice. Hence, the problem of deriving the propagating modes excited at a certain frequency reduces to finding such modes only in the directions of the vectors of the irreducible Brillouin zone. The irreducible zone in the case of a totally symmetric square unit-cell is a triangular wedge with $(1/8)^{\text{th}}$ the area of the square (Figure 3.1).

Two phase shift (shown as phase $p_{\text{x}}$ and phase $p_{\text{y}}$) and proper boundary conditions along the sides of the unit-cell (resembling an infinite structure) are used in order to determine the dispersion diagram [3]. The eigenmode solver of HFSS will calculate the frequencies of propagating waves that would generate such phase shifts.

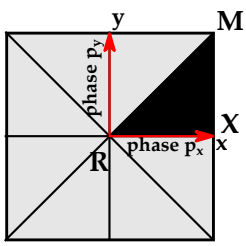


Figure 3.1: Brillouin triangle.

Plotting the dispersion diagram involves three major steps [4]

• The phase $p_y$ along the direction y is fixed at 0°. Correspondingly, the phase $p_x$ along x direction, the base of the Brillouin triangle, called R − X direction, is varied from 0° to 180°. Then, for each phase difference, the first set of eigen mode frequencies are found. This generates the frequency dataset for the wave propagation in the R − X segment of the Brillouin triangle.

• The phase $p_x$ along the R − X segment of the Brillouin triangle, x direction, is then fixed at 180° and the phase $p_y$ along the X −M segment, y direction, is varied from 0° to 180°. Then, from simulations or calculation of dispersion equation the second set of eigen mode frequencies are found.

• The phase $p_x$ and phase $p_y$ along both the segments, R − X and X −M , are varied identically from 180° to 0°. Hence, the third set of eigen mode frequencies are found for the M − R segment of the Brillouin triangle.

An example of two dispersion diagrams of EBG structures [5] showing the evolution of multiple modes of propagation as function of frequency is presented in Figure 3.2. Although the dispersion diagram is seen as one continuous graph, it is composed of three graphs. Each of those graphs describes the dispersion characteristics of one of the three branches mentioned above.

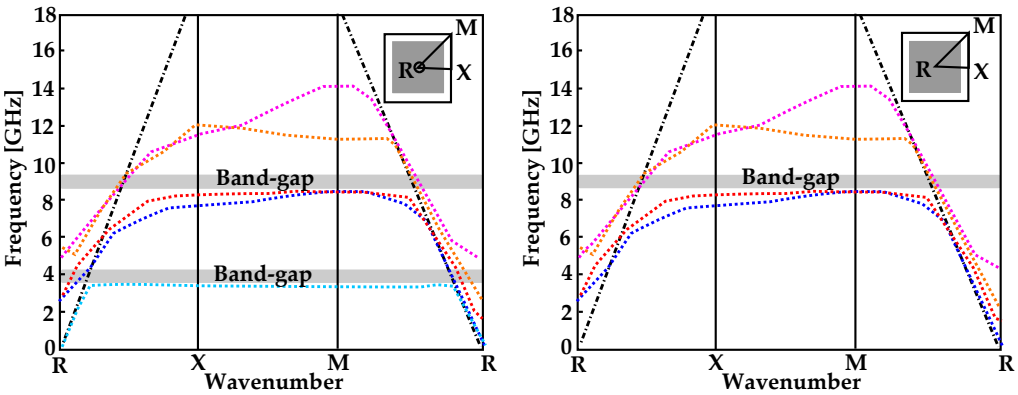


(a) with vias (b) without vias

Figure 3.2: Dispersion diagram of a totally symmetric square unit-cell with and without vias.

The periodic structures can exhibit multiple band-gap properties. The dispersion diagram of the EBG structure having metallic patches connected to the ground plane by metal plated vias (i.e. mushroom-type EBG structure) is shown in Figure 3.2(a). The first dispersion curve is a TM mode. At low frequencies the TM mode lies very near the light line (with a slope equal to the speed of light in vacuum) up to a certain frequency. The second dispersion curve which is represented by a TE mode begins at

a higher frequency and continues upwards with a slope less than the vacuum speed of light. The TE waves that lie to the left of the light line exist as leaky waves.

A band gap, within the EBG periodic structure does not support surface waves, extends from the top edge of the first dispersion curve (TM mode) to the point where the second dispersion curve (TE mode) crosses the light line as presented in Figure 3.2(a). Therefore, the presence of vias is critical for the suppression of TM surface waves and the creation of band gaps at significantly lower frequencies.

In the case of the EBG structure without vias, the dispersion curves starting with the second one are unaffected by the absence of the vias, and appear similar to the waves on the mushroom type-EBG. However, the first dispersion curve, (the TM mode) is no longer terminated below the resonance frequency, as they were when the vias were present, and there is no band gap between the first two modes. The first band gap occurs between the second and the third modes (TE surface wave suppression).

### Suspended Microstrip

The performance of any periodic EBG structure can be analyzed using the scattering parameters [6], [7]. The scattering parameters of structures with finite physical dimensions are usually easy to calculate.

To model this feature, a suspended microstip having a characteristic impedance of 50 Ω is located at 0.02 $\lambda_0$ [8] over the EBG structure (see Figure 3.3). Two 50 Ω SMA connectors, placed at each edge of the suspended microstrip are used to transmit and receive EM waves and the power transfer between them is computed. Without the existence of EBG structure beneath the microstrip line, the EM waves can pass through the strip line with high efficiency. No power reduction can be found within the frequency range without the existence of EBG structure.

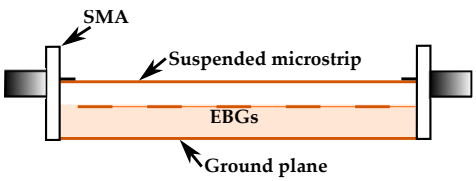


Figure 3.3: Suspended microstrip scheme.

Then, if any periodic EBG structure is placed below the microstrip line, the power transfer reduction band appears (as it is plotted in Figure 3.4), its range being dependent on the geometrical shape of the EBG structure. For frequencies within the power reduction region, the EBG structure will block transmission of

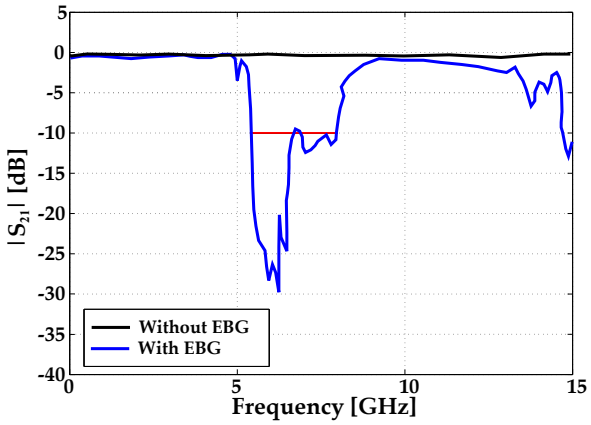


Figure 3.4: Power transfer reduction band with and without EBG structure.

power along the microstrip. Because of this feature, a noticeable reduction in $S_{21}$ can be observed at a certain frequency band, the attenuation level being given by the number of the unit-cells. Increasing the unit-cell number the depth of the reduction band increases so the power transfer reduction band in more obvious. The power reduction transfer band of the EBG structure is defined as the frequency region in which $S_{21}$ is less than -10 dB.

### 3.1.1 5.8 GHz Electomagnetic Band-Gap Design

In Chapter 2, the resonant element, replicated to model an infinite resonant structure, is characterized as an Artificial Magnetic Conductor (AMC) [9] and the in-phase reflection property was studied. This feature enables efficient radiation for antennas placed closed to the periodic structure. In this chapter the same resonant structure is seen from another point of view: as a material that has the possibility to block the propagation of electromagnetic waves in certain frequency bands and guide them in a desired direction (electromagnetic band-gap (EBG)).

#### 3.1.1.1 Dispersion Diagram

The dispersion characteristics, such as the position and width of the band-gap and the frequency of the propagating modes are primarily defined by the geometry of the unit-cell. The same unit-cells as the ones presented in Chapter 2 are characterized. In Figure 3.5 the simulation setup of the 5.8 GHz structure is presented.

The filtering mechanism of the EBG structure is demonstrated through the simulated dispersion diagram for the three lowest modes depicted in Figure 3.6. The

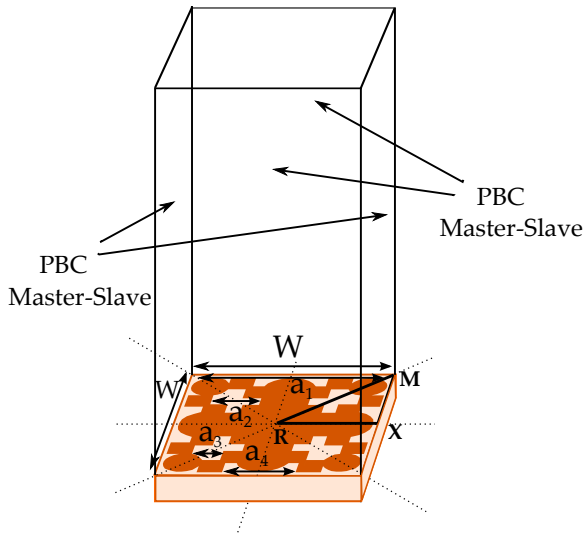


Figure 3.5: Unit-cell resonator - The applied boundary conditions with the irreducible Brillouin triangle.

EBG structure at its irreducible Brillouin zone has propagating modes over a certain frequency band.

When the unit-cell size is $W = 11.52$ mm ($a_1$= 11.40 mm, $a_2$= 2.85 mm, $a_3$= 1.78 mm, $a_4$= 4.27 mm) and ARLON25N is used as dielectric substrate, the first mode propagates in the frequency range from 5 GHz to 6.6 GHz whereas the second mode propagates from 5 GHz to 7 GHz. The resonance frequency takes place between the first and second mode, being around 6 GHz. Moreover, the band-gap is presented in a frequency range between 7 GHz and 7.9 GHz. Within the band-gap regime of the EBG, no propagating modes are possible (the electromagnetic waves cannot propagate at any direction). This band-gap is unique to EBG structures, while for a standard dielectric no such gap exists.

The influence of the unit-cell geometry on the dispersion diagrams has been studied. The distance between the metallization edge and the unit-cell edge controls the band-gap position. More precisely when the mentioned distance increases, the band-gap shifts to a higher frequency band whereas its width increases. The variation of the $a_2$ and $a_3$ parameters (see Figure 3.5) has the following effect: as $a_2$ and $a_3$ increase the band-gap shifts to a lower frequency band whereas the width of the band-gap increases. When $a_1$ and $a_4$ parameters decrease, meaning that the whole unit-cell size decreases, the band-gap shifts to a higher frequency band and its width increases. The thickness of the dielectric substrate also affects the band-gap position. Increasing the thickness, the band-gap shifts to a lower frequency band

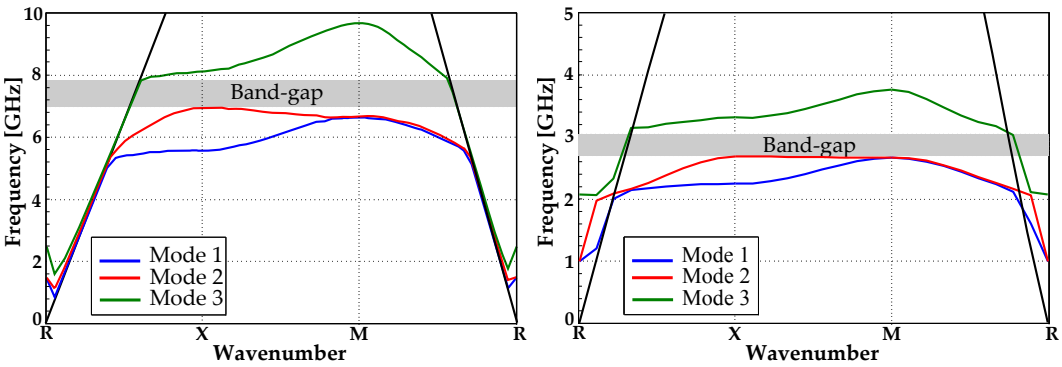


(a) $W$ = 11.52 mm, ARLON25N (b) $W$ = 16.38 mm, RO3010

Figure 3.6: Dispersion diagram of the EBG structure for different dimensions of the unit-cell and different dielectric substrates.

and in the same time its width increases.

As it is expected, by increasing the relative permittivity of the dielectric substrate and making the unit-cell bigger ( $W$ = 16.38 mm, $a_1$= 16.21 mm, $a_2$= 4.05 mm, $a_3$= 2.50 mm, $a_4$= 6.08 mm and using RO3010 as dielectric substrate), the resonance frequency and band-gap shifts to a lower index , the band-gap becoming narrower.

| Unit-cell size (mm) | Dielectric substrate | Rel. perm. $\varepsilon_r$ | Dielectric thickness (mm) | Reso. freq. (GHz) | Band-gap width (MHz/%) |
|---|---|---|---|---|---|
| 11.52 ($\lambda_0$/4.5) | ARLON25N | 3.28 | 1.27 ($\lambda_0$/33) | 6 | 800 / 15 |
| 16.38 ($\lambda_0$/9.3) | RO3010 | 10.2 | 1.27 ($\lambda_0$/95) | 2.5 | 340 / 13.6 |

Table 3.1: Band-gap width for different dimensions of the unit-cell (simulations).

#### 3.1.1.2 Suspended Microstrip

In the previous sections, the in-phase reflection property and the dispersion diagram of an infinite number of unit-cells have been presented. Next, for the same unit-cell geometry, the power transfer reduction band of a finite structure is investigated. To further save computation time, a small EBG structure consisting of 4x4 unit-cells is used and shown in Figure 3.7. By knowing the position of the power reduction band of the structure, the radiation properties and bandwidth of a patch antenna can be enhanced.

Figure 3.8 shows the simulated transmission coefficient $S_{21}$ exploiting the suspended microstrip method. The same geometry of the unit-cell has been used with

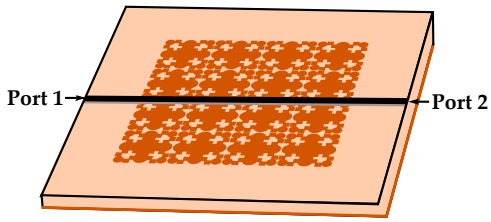


Figure 3.7: Suspended microstrip setup.

two different dielectric substrates. For a unit-cell size of 11.52 mm printed on ARLON25N, the $S_{21}$ value drops below -10 dB between 6.5 GHz and 6.88 GHz, which means a bandwidth of 0.38 GHz. This frequency band indicates the range of the power transfer reduction band for the EBG structure.

In the case of increasing the unit-cell dimensions to 16.38 mm and changing ARLON25N with RO3010, the simulated transmission coefficient between Port 1 and Port 2 lies within 2.47 GHz and 2.62 GHz.

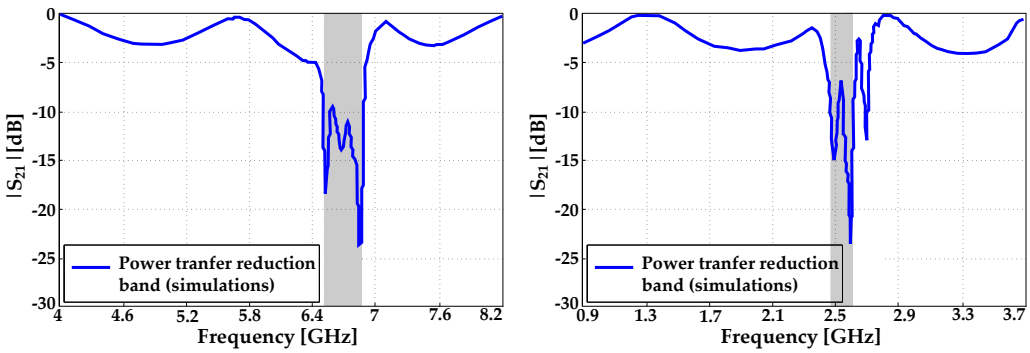


(a) ARLON25N, $W = 11.52$ mm (b) RO3010, $W = 16.38$ mm

Figure 3.8: Power transfer reduction band of the 4x4 periodic structure using different dielectric substrates and different dimensions of the unit-cell.

#### 3.1.1.3 Comparison Between the AMC and EBG Behaviors

The in-phase reflection phase of a normally incident plane wave is the AMC primary feature whereas the band-gap region (characterized by the dispersion diagram) and the power transfer reduction band (characterized using the suspended microstrip method) are characteristic for EBG structures [10]. However, as shown in previous section, the band gap and the reduction of $S_{21}$ for the studied sample occur at higher frequencies than the resonance frequency of a normally incident plane wave. As the unit-cell does not have vias, the frequency band of the AMC behavior

does not coincide with the frequency band of the EBG performance (either the drop in $S_{21}$ or the frequency band where no propagation modes take place).

Next the differences between the two EBG characterizations will be pointed out.

From the dispersion diagram it can be concluded that the lower edge of the band-gap is located at 7 GHz. However, if it is considered the 10 dB power transfer reduction band, for this sample it can be noticed that this band extends from 6.5 GHz to 6.88 GHz. Therefore, the lower edge of the power transfer reduction band is not the same as the lower edge of the band-gap. In addition, it is expected although there is not such a rule that the band-gap is wider than the power transfer reduction band and encompass it. The difference of the two extracted bands is attributed to the following reasons:

1) The dispersion diagram is extracted for an idealistic case where the periodic EBG structure is infinite. However, the power transfer reduction band is extracted for a finite number of EBG unit-cells. In the case under study, in the setup provided in Figure 3.7, two measuring ports (the source and the receiver ports) are separated by only 4 unit-cells of EBGs. Due to the discontinuity in the structure, one can also expect radiation to the surrounding environment and multiple reflections.

2) In a band-gap which is defined between the upper cut off frequency of the lower propagating mode and lower cut off frequency of the upper propagating mode, no modes exists. If there is no infinite number of EBG unit-cells between source and receiver ports, then the 10 dB power transfer reduction band limits might not locate precisely at the edge of the band-gap. Also, the infinite number of EBG unit-cells contributes to infinite-attenuation level in the power transfer reduction band.

Moreover, a band-gap is a gap whose characteristic is the absence of propagating modes whereas a power transfer reduction band is a gap where the power transferred is reduced and does not imply the absence of propagating modes. In other words, in the power transfer reduction band the level of transferred power between two ports (with EBG unit-cells located between them) is reduced by more than 10 dB due to the presence of EBG unit-cells.

The 10 dB power transfer reduction band of this sample determined using the suspended microstrip method is very narrow and it does not overlap with the band-gap region.

Figure 3.9 presents the behavior of the periodic structure when it is characterized as an AMC and as an EBG (the dielectric substrate used is ARLON25N and the dimension of the unit-cell is $W = 11.52$ mm).

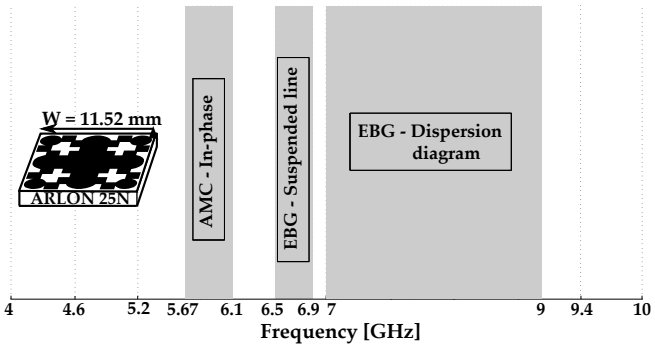


Figure 3.9: Comparison between the AMC and EBG behaviors.

### 3.1.2 Polarization Dependent Electromagnetic Band-Gap Design

#### 3.1.2.1 Suspended Microstrip

To further demonstrate the performance of the polarization dependent EBG structure, a model integrated with a suspended 50 Ω microstrip is simulated, as shown in Figure 3.10.

8x8 miniaturized unit-cells are printed on RO4003C dielectric substrate. The simulated result shows that the frequency range with $S_{21}$below -10 dB extends from 6.84 to 7.06 GHz, the bandwidth achieved being about 0.22 GHz (3.15%). The power transfer reduction band is centered at 7 GHz.

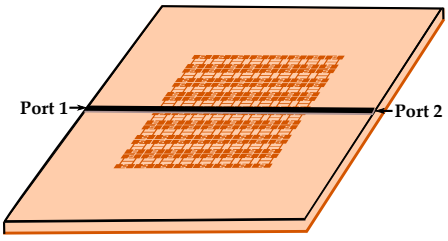


(a) Suspended microstrip setup.

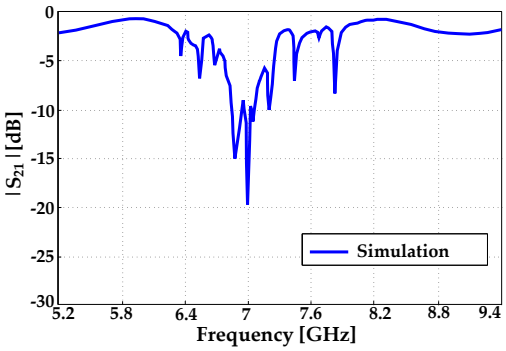


(b) Power transfer reduction band of the polarization dependent EBG structure.

Figure 3.10: Polarization dependent EBG structure.

#### 3.1.2.2 Comparison Between the AMC and EBG Behaviors

For the polarization dependent structure, the AMC and EBG behaviors do not occur simultaneously at the same frequency band. The AMC in-phase [11] characteristics are satisfied at 6.2 GHz while the maximum attenuation of the power transfer reduction band is achieved at 7 GHz (see Figure 3.11). Even though there is a frequency shift (as expected due to the absence of via holes from the unit-cell geometry) of 12%, the simulated bandwidth is almost the same for the two behaviors.

The dispersion diagram for the polarization dependent structure has not been computed because the replicated unit-cell is not completely symmetrical. Although the unit-cell wave propagation issue is reduced to half of its size (due to the unit-cell unique symmetry plane) more than one dispersion diagram could be plotted. Therefore, depending on the application where the EBG structure will be used, and also on the unit-cell parts the designer is focused on, the dispersion diagram could be easily represented.

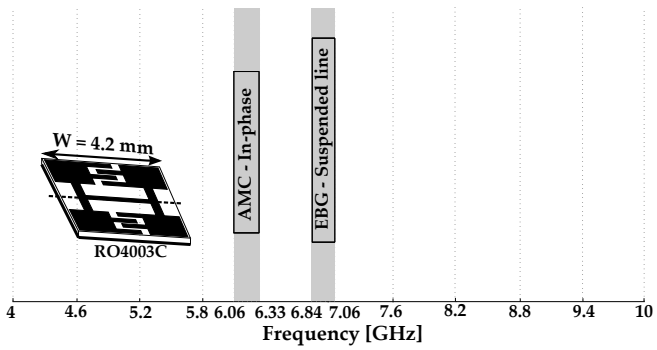


Figure 3.11: Comparison between the AMC and EBG behaviors for the polarization dependent structure.

### 3.1.3 Polarization Insensitive Electromagnetic Band-Gap Design

#### 3.1.3.1 Suspended Microstrip

The layout of the polarization insensitive EBG structure is presented in Figure 3.12. Now the miniaturized unit-cell which forms the new 2x2 polarization independent unit-cell is arranged in a 5x5 lattice in order to be evaluated as an EBG structure (using the suspended microstrip method). As the new 2x2 polarization independent unit-cell embodies in one of its diagonal the original elements (unit-cells) and in the other diagonal the elements rotated clockwise 90°, two power transfer reduction band are expected.

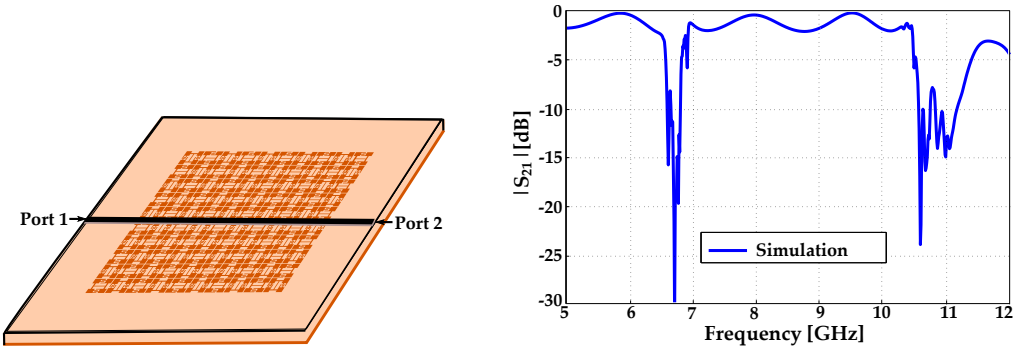


(a) Suspended micostrip setup.

(b) Power transfer reduction band of the polarization insensitive EBG structure.

Figure 3.12: Polarization insensitive EBG structure.

Any frequency contained in the band where the transmission coefficient is less than -10 dB is considered part of the power transfer reduction band. It can be noted that a deeper rejection (maximum rejection of 30 dB) band is obtained around the center frequency 6.7 GHz whereas for the center frequency 10.6 GHz the rejection is approximately 24 dB. Below the first power transfer reduction band and up to 10.56 GHz where the second power transfer reduction band appears, a flat linear variation with low insertion losses is presented. The first power transfer reduction band lies between 6.59 to 6.80 GHz (meaning a bandwidth of 3.15%) respectively from 10.56 to 11.17 GHz (meaning a bandwidth of 5.75%) for the second power transfer reduction band.

#### 3.1.3.2 Comparison between the AMC and EBG behaviors

For the polarization insensitive structure, the EBG behavior takes place at a higher frequency band than the AMC behavior whereas the operational bandwidth of both EBG and AMC behaviors is the same for the lower frequency band. For the upper frequency band, the operational bandwidth of the EBG behavior is contained in the AMC's one as it can be seen in Figure 3.13.

## 3.2 Characterization and Measurement Results Using the Suspended Microstrip Method

### 3.2.1 5.8 GHz Electromagnetic Band-Gap Design

The manufactured prototype is presented in Figure 3.14 together with the comparison between the simulated and measured results. The measurements are slightly

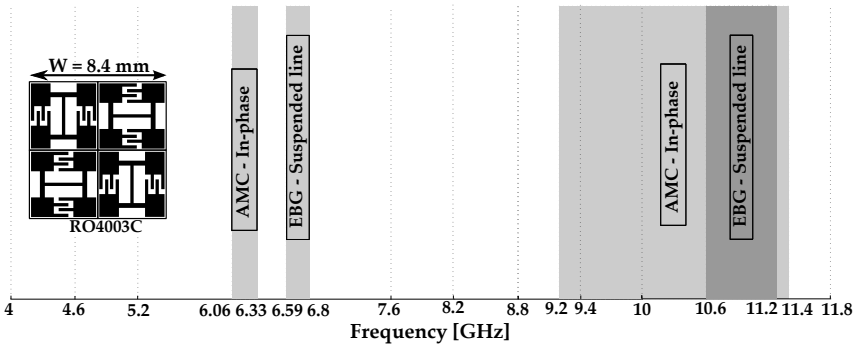


Figure 3.13: Comparison between the AMC and EBG behaviors for the polarization insensitive structure.

shifted (1.5%) downwards in frequency. The mentioned deviation is due to the variation of the relative dielectric permittivity with respect to its nominal value used in simulations. Furthermore, the process misalignments between the suspended microstrip and the EBG structure could cause the frequency variation and also the losses introduced by the two connectors.

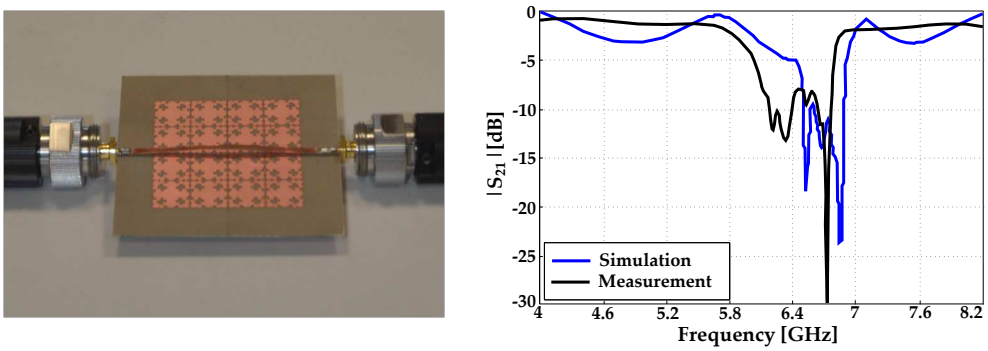


(a) Photo of the suspended microstrip measurement setup.

(b) Measured and simulated transmission coefficient.

Figure 3.14: 5.8 GHz EBG design - characterization and results.

### 3.2.2 Polarization Dependent Electromagnetic Band-Gap Design

Figure 3.15 presents the measurement results of the EBG structure with the suspended microstrip 0.02 $\lambda_0$ above the surface. The drop in $S_{21}$shows a clear power transfer reduction band around 6.87 GHz. Apart from the slight frequency shift, the measurement results are consistent with the simulations.

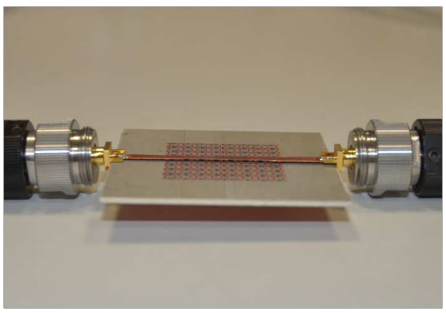

(a) Photo of the suspended microstrip measurement setup.

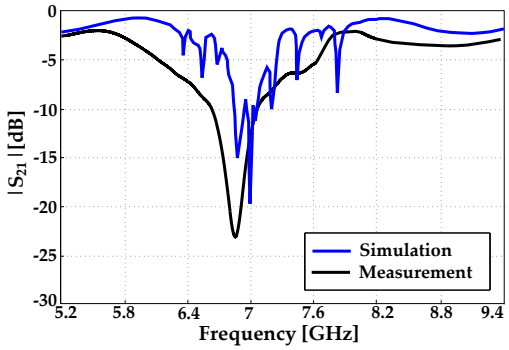


(b) Measured and simulated transmission coefficient.

Figure 3.15: Polarization dependent EBG - characterization and results.

### 3.2.3 Polarization Insensitive Electromagnetic Band-Gap Design

When the miniaturized unit-cell which forms the new 2x2 polarization independent unit-cell is arranged in a 5x5 lattice in order to be evaluated as an EBG structure (using the suspended microstrip method), the center frequency of the power transfer reduction band in measurement and simulation agree well in both frequency bands. Additionally, the measured bandwidth is broaden (see Figure 3.16), normally due to the losses introduced by the two connectors and due to the misalignments when placing the suspended microstrip line. At the higher frequency, the bandwidth increases even more.

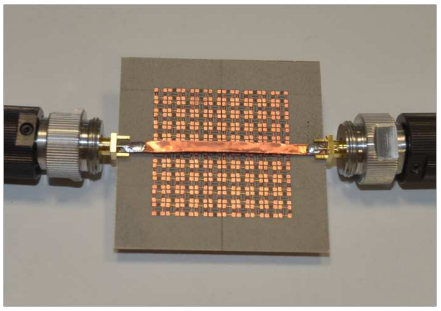

(a) Photo of the suspended microstrip measurement setup.

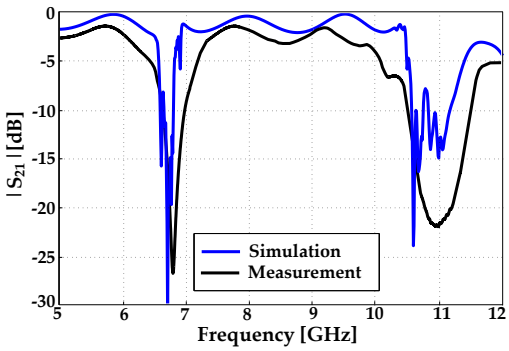


(b) Power transfer reduction band of the polarization insensitive EBG structure.

Figure 3.16: Polarization insensitive EBG - characterization and results.

## 3.3 EBGs Applied to Antennas

### 3.3.1 Bandwidth Enhancement of Patch Antennas

Microstrip patch antennas offer an attractive solution to compact and ease-low-cost design of modern wireless communication systems due to their many advantages as light weight and low volume, low profile, planar configuration which can be easily made conformal to host surface, low fabrication cost, and the capability of obtaining dual and triple frequency operations.

When mounted on rigid surfaces microstrip patch antennas are mechanically robust and can be easily integrated with microwave integrated circuits (MICs). However, microstrip patch antennas suffer from a number of disadvantages as compared to conventional antennas.

Some of their major drawbacks are the narrow bandwidth, low gain, and surface wave excitation that reduce the radiation efficiency. To overcome one of their more critical restrictions, narrow bandwidth, several techniques can be used [12]. First of all, a thicker substrate with a low dielectric constant or a ferrite composition provides a wider bandwidth but the first approach leads to no low-profile designs and increased in size, whereas the second solution is expensive. Secondly, noncontacting feeding methods such as proximity/aperture coupled can be used to improve the impedance bandwidth, but this is difficult to fabricate. Another possibility is multi-resonator stack configuration with the inconvenient of resulting large thickness prototype. The surface waves can be minimized using electromagnetic band-gap structures whereas for obtaining a high gain antenna an array configuration for the patch elements is needed [13, 14, 15].

#### 3.3.1.1 Patch Antenna Design

The microstrip patch antenna is a narrow band design. Depending on the substrate's parameters (thickness and relative permittivity) and feeding method employed the bandwidth and frequency of operation can be tuned.

The higher the substrate's thickness and lower the dielectric permittivity the wider the bandwidth. The antenna design has been carried out using an electromagnetic simulator based on the Method of Moments. ROGER3010 substrate having a thickness of $h = 1.27$ mm, relative dielectric permittivity $\varepsilon_r = 10.2$ and $\tan\delta = 0.0023$ has been used. Such a high dielectric permittivity substrate has been used to reduce the antenna size. The characteristic impedance of the transmission line is 50 Ω. The layout of the 2.48 GHz antenna with its dimensions is shown in Figure 3.17. From Figure 3.18, it can be extracted that the simulated operating bandwidth of the patch antenna is 20 MHz (0.81%).

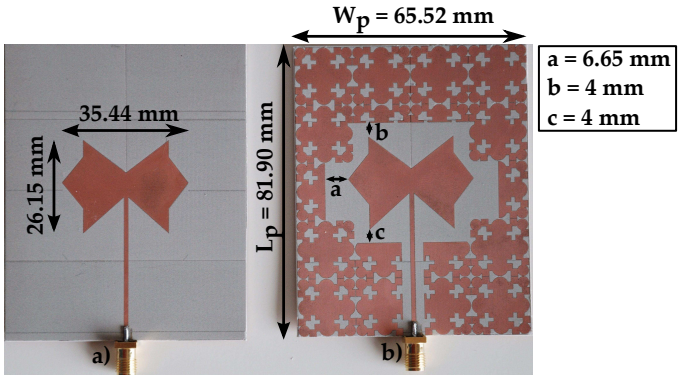


Figure 3.17: Manufactured prototypes: (a) Patch antenna; (b) Patch antenna-EBG.

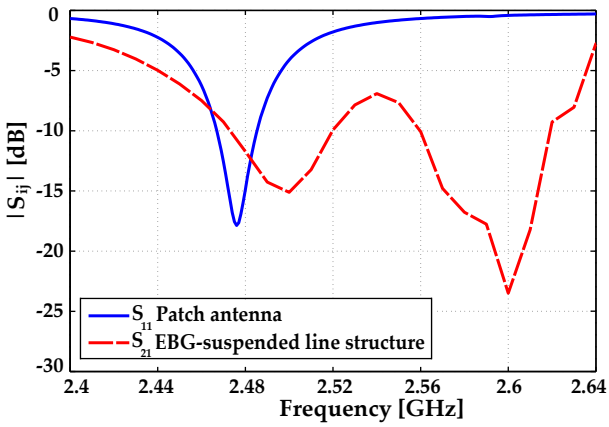


Figure 3.18: Resonances to be coupled in order to achieve bandwidth enhancement.

#### 3.3.1.2 Patch Antenna Combined with EBGs/AMCs

- Patch antenna surrounded by the EBG

In order to suppress the surface waves and to increase the bandwidth, the EBG structure is arranged around the patch, forming a uniplanar design [16] (Figure 3.17(b)). The resonance frequency of both structures (patch antenna and EBG structure) is mutually influenced, and depending on the frequency difference between them and the unit-cell arrangement around the patch antenna, the resulting resonance frequency changes.

The power transfer reduction band of the EBG structure is designed to be adjacent to the frequency band of the patch antenna, so that when integrating the two structures on the same layer, their resonances couple each other, and, as a result, a wider bandwidth will be generated without disturbing other characteristics of the patch antenna such as the radiation pattern [17].

The frequencies included on the patch antenna's bandwidth are adjacent to the ones included on the lower power transfer reduction band. The selected EBG arrangement with respect to the antenna is a trade-off between performance and size.

The dimensions of the final structure (Figure 3.17(b)) are $W_{\mathrm{p}} = 65.52$ mm and $L_{\mathrm{p}} = 81.90$ mm. The dimension of the unit-cell using RO3010 dielectric substrate in the case of EBG characterization is 16.38 mm.

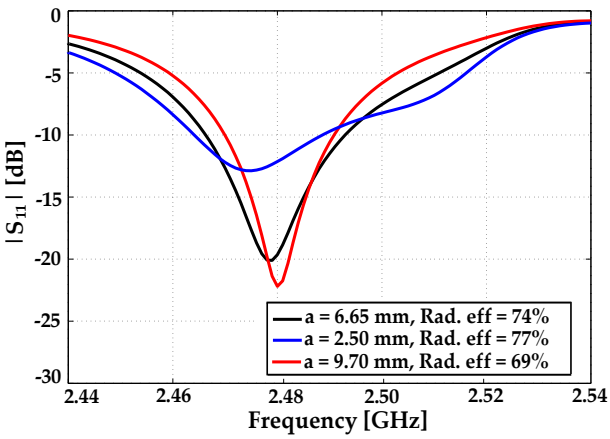


Figure 3.19: Return loss of the Patch antenna-EBG versus parameter $a$.

A parametric study regarding the distance between the patch antenna and the unit-cells has been conducted. With the unit-cells sufficiently separated from the antenna (increasing the parameter $a$) the bandwidth and radiation efficiency decrease, whereas the level of the return loss at the main resonance frequency increases (Figure 3.19). The matching is slightly influenced by the parameter $b$ whereas the $c$

parameter does not have a big influence in the functionality of the antenna. The optimal distance $a$ between the patch antenna and unit cell is 6.65 mm. Above this distance the bandwidth and radiation efficiency decrease (Figure 3.20).

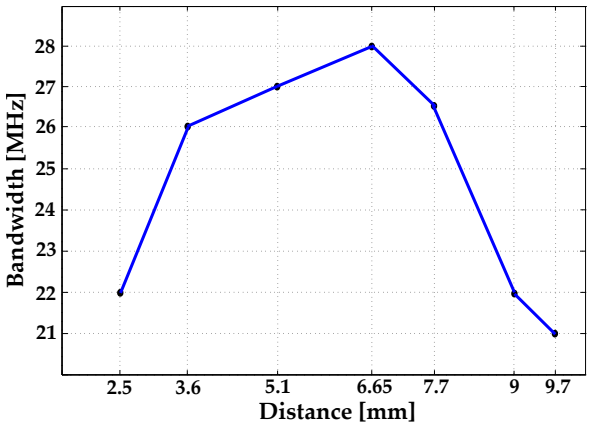


Figure 3.20: Bandwidth of the Patch antenna-EBG versus parameter $a$.

- Patch antenna placed above by the AMC

A $4 \times 5$ cells planar AMC structure is placed as patch antenna ground plane [18] (see Figure 3.21) in order to analyze if the antenna's bandwidth and the radiation properties can be improved. The antenna is fixed to the AMC structure by a 0.1 mm double-sided nonconducting adhesive tape.

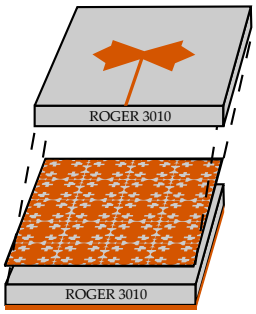


Figure 3.21: Patch antenna-AMC prototype layout.

The microstrip patch antenna bandwidth is 20MHz whereas the AMC operation bandwidth is 130 MHz (see Figure 2.7), having each one the same resonance frequency, 2.48 GHz. However, for combining the two structures, the antenna's ground plane has been removed and is placed above the AMC. As a consequence the antenna's resonance frequency decreases due to capacitive effects for those frequencies within the AMC bandwidth.

A resonance is obtained in the AMC bandwidth and outside this band the antenna behaves as if its substrate thickness had doubled. Merging both effects, the combined structure resonates in a bandwidth wider than the microstrip patch antenna alone, but narrower than the AMC bandwidth. As disadvantage, the thickness of the combined structure is increased.

#### 3.3.1.3 Measurement Results

Prototypes of the patch antenna, patch antenna placed above the AMC structure, and patch antenna surrounded by the EBG cells have been manufactured using laser micromachining. The return losses of each manufactured prototype have been measured.

As it can be observed in Figure 3.22 the measured operating bandwidth of the patch antenna is 23 MHz. The difference in bandwidth between simulations (20 MHz) and measurements (23 MHz) could be due to the fact that the commercial MoM software considers infinite extension for the dielectric substrate, or even more likely due to manufacturing tolerances.

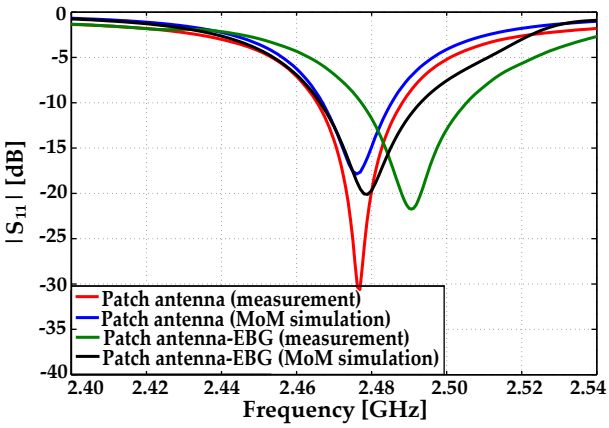


Figure 3.22: Simulation and measurement comparison between the prototypes: patch antenna and patch antenna-EBG.

In the case of placing the antenna above the AMC structure the antenna resonance frequency is shifted downwards to 2.43 GHz (see Figure 3.23) due to the capacitive effects that are generated between the two combined structures. Also, as the AMC structure has wider bandwidth than the patch antenna, the resulting prototype bandwidth increases to 46 MHz, meaning a 100% broader bandwidth.

When the patch antenna is surrounded by one row of EBG unit-cells the bandwidth increases 50% due to the property of coupling the frequency bands of the

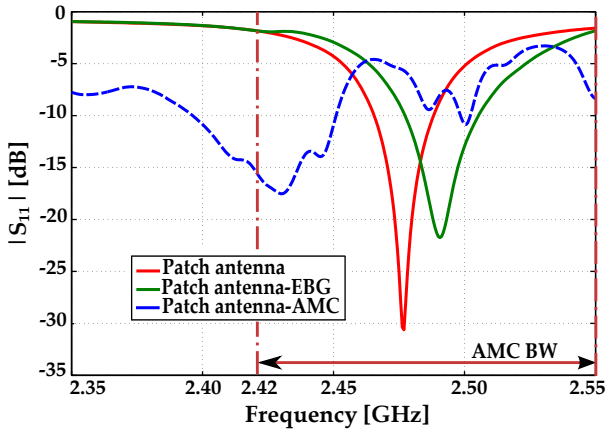


Figure 3.23: Measurement comparison between the prototypes: patch antenna, patch antenna-EBG and patch antenna-AMC.

two structures composing the prototype. It is remarkable that this 50% bandwidth improvement is achieved neither increasing the prototype size nor the thickness. In Table 3.2 a comparison in terms of bandwidth, gain, directivity and radiation efficiency is presented.

| Prototype | Bandwidth [MHz] | Gain [dB] | Directivity [dB] | Rad. Eff. [%] |
|---|---|---|---|---|
| | Mea. | Sim./Mea. | Sim./Mea. | Sim./Mea. |
| Patch antenna | 23(0.93%) | 4.29/4.6 | 5.59/7.33 | 68.23/53 |
| Patch antenna-EBG | 34(1.37%) | 5.56/4.6 | 6.84/7.50 | 74.47/51 |
| Patch antenna-AMC | 46(1.90%) | 0.79/0 | 8.52/6.72 | 16.86/21 |

Table 3.2: Gain, directivity and radiation efficiency of the prototypes.

Measured radiation pattern cuts in the E and H planes of each manufactured prototype are presented in Figure 3.24 and Figure 3.25. The patch antenna prototype exhibits co-polarization-cross-polarization (CP-XP) ratio better than 25 dB (see Table 3.3), whereas for the patch antenna-EBG prototype the (CP-XP) ratio is even increased.

In measurements the gain of the patch antenna (4.6 dB) is preserved when the antenna is surrounded by one row of EBG unit-cells. From the simulation results, using EGB structures around the patch antenna its radiation efficiency increases, due to surface wave suppression property. However from measurement results it can be concluded that for this specific arrangement, the radiation efficiency is preserved (while improving bandwidth).

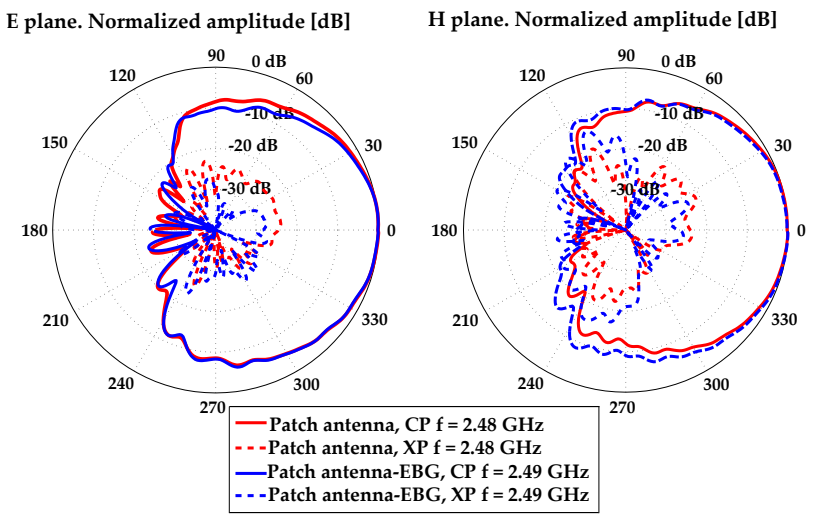


Figure 3.24: Measured radiation diagram of the prototypes: patch antenna and patch antenna-EBG.

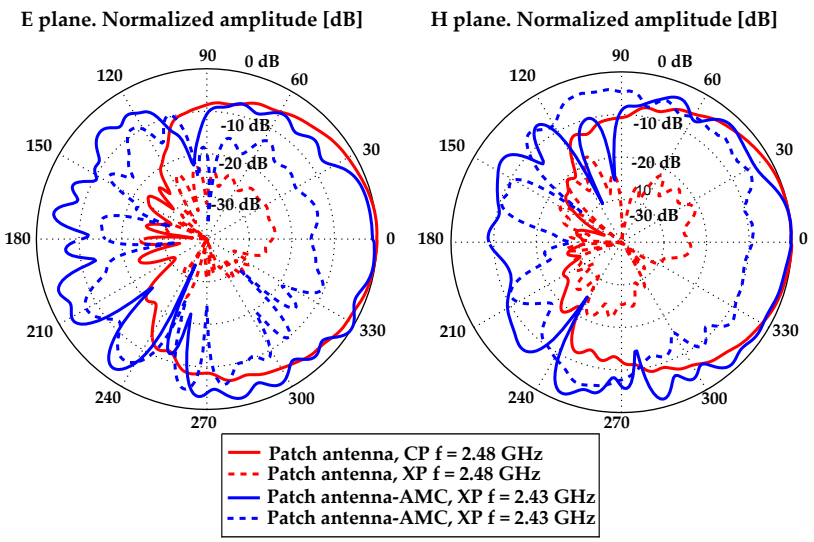


Figure 3.25: Measured radiation diagram of the prototypes: patch antenna and patch antenna-AMC.

The difference between simulations and measurements relies on the fact that the simulation method implemented by Momentum considers infinite dielectric under the finite EBG metallization but also the difference could be attributable to misalignment in the anechoic chamber. Radiation pattern properties of the patch antenna-AMC prototype show a (CP-XP) ratio inferior to the other two prototypes and a gain close to 0 dB.

| Prototype | CP-XP ratio (E plane, dB) | CP-XP ratio (E plane, dB) |
|---|---|---|
| Patch antenna | 25.8 | 25.0 |
| Patch antenna-EBG | 30.4 | 28.8 |
| Patch antenna-AMC | 13.9 | 9.4 |

Table 3.3: CP-XP ratio comparison.

As the AMC does not have the ability to suppress the surface waves and the fact that the thicker the substrate, the stronger the surface waves, the gain of the patch antenna-AMC prototype does not improve. Also as the CP-XP ratio is worst for patch antenna-AMC than for the other prototypes, part of the energy could be radiated in other polarizations and backwards.

In order to improve the gain, a gap between the antenna and the AMC structure could be used but this is technologically less advantageous.

In addition, the microstrip patch antenna's gain and directivity can be increased when more rows or/and columns surround the prototype, so a trade-off between performance and size must be taken (the higher the number of unit-cells in a periodic arrangement, the closer its behavior to an infinite EBG structure).

By adding rows and columns of EBG unit-cells around the patch antenna (Figure 3.26), the resonance frequency together with the radiation characteristics can be tuned (Figure 3.27), but this runs counter the principle of compact design in wireless communication circuits.

From Table 3.4 it can be concluded that the directivity increases when the antenna is surrounded by more unit-cells (the higher the number of unit-cells in a periodic arrangement, the closer its behavior to an infinite periodic structure). However the gain increases only when the unit-cells are added in the upper part of the design and the increment is lower than the one in the directivity which can lead to low radiation efficiency. Thus depending on the intended application a trade-off between enhancement in bandwidth, gain and directivity has to be adopted. It is remarkable that the presented patch antenna-EBG prototype exhibits enhancement in bandwidth and radiation efficiency without increasing the size of the reference patch

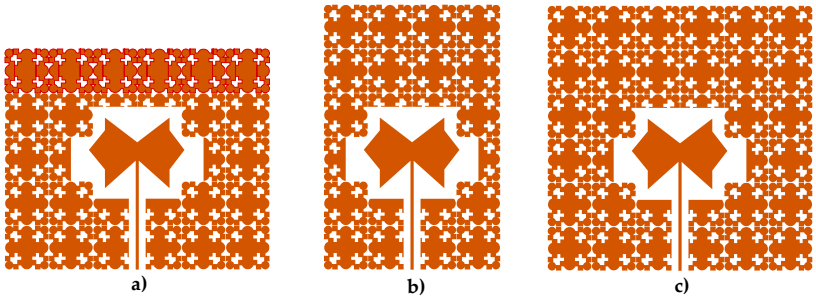


Figure 3.26: Different unit-cell arrangements combined with the patch antenna. a) Patch antenna-EBG-#2, b) Patch antenna-EBG-#3, and c) Patch antenna-EBG #4.

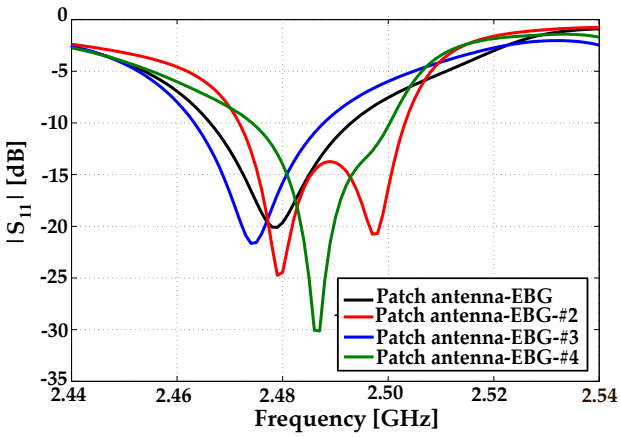


Figure 3.27: Simulated return loss for the Patch antenna-EBG, Patch antenna-EBG-#2, Patch antenna-EBG-#3 and Patch antenna-EBG-#4.

antenna prototype and being more compact than the others presented in Table 3.4.

| Prototype | Freq. [GHz] | Bandw. [MHz] | Direct. [dB] | Gain [dB] | Rad. eff. [%] |
|---|---|---|---|---|---|
| Patch antenna | 2.476 | 20(0.81%) | 5.9 | 4.3 | 69 |
| Patch antenna-EBG | 2.479 | 27(1.09%) | 6.8 | 5.5 | 74 |
| Patch antenna-EBG-#2 | 2.479 | 32(1.30%) | 7.7 | 4.8 | 51 |
| Patch antenna-EBG-#3 | 2.474 | 25(1.01%) | 8.5 | 6.9 | 69 |
| Patch antenna-EBG-#4 | 2.487 | 27(1.09%) | 10.7 | 7.7 | 50 |

Table 3.4: Radiation properties of the patch antenna combined with different cell arrangements. (simulations).

## 3.4 EBGs Applied to Filters

Filters play important roles in many microwave applications. In recent years, emerging applications have continued to challenge microwave filters' designers with stringent simultaneous requirements such as high performance, light weight, low cost and miniaturization.

As the electromagnetic spectrum is limited and has to be shared, small sized band-pass filters with narrow frequency response and high selectivity are used to confine the signals within assigned spectral limits and to reject the noise and interferences from adjacent channels.

Depending on the requirements and specifications, filters may be designed as lumped element or distributed element circuits.

To minimize the filter size, a practical strategy is to reduce the resonator circuit by modifying its physical structures [19, 20]. Starting from the conventional parallel coupled band-pass filter [21, 22, 23] which has a simple synthesis procedure and ending with U-shape resonators and open loops [24], hairpin filters make has helped progress in size reduction. However, with the rapid evolution of modern communication systems the sizes of these resonators are still not small enough to be used.

### 3.4.1 Band-Pass Filter

In this part of the Doctoral Thesis a novel band-pass filter (henceforth referenced as BPF) without vias is presented. The novelty relies on taking advantage of the predicted electromagnetic band-gap (EBG) properties of a resonator unit-cell (by means of its dispersion diagram) to achieve the band-pass filter behavior.

In Section 3.1.1.1 the dispersion diagram of the unit-cell resonator is presented. The dimension of the unit-cell resonator is $W = 11.52$ mm and ARLON25N is used as dielectric substrate.

With the purpose of designing a band-pass filter having the same size as the unit-cell resonator, the propagation mode paths along the R-X-M triangle and predicted by the dispersion diagram could be followed. The frequency of the modes propagating along the edges of the Brillouin triangle have to be taken into account to define the filter passband, whereas the band-gap can be used to achieve the filter stopband.

Taking into account that the goal is to obtain a selective band-pass filter, only the (M-R) region and part of the (X-M) region from the dispersion diagram will be considered.

#### 3.4.1.1 Band-Pass Filter Design

The band-pass filter consists of a unit-cell resonator and two narrow lines coupled to the resonator. Each narrow line has a width of 0.1 mm and a length of 11.52 mm. The two narrow lines are placed symmetrically with respect to the unit-cell resonator. The gap between the coupling narrow line and unit-cell resonator is 0.1 mm. The filter is excited by a pair of non-orthogonal input/output 50 Ω microstrip feeding lines of 1.8 mm width and is printed on ARLON25N substrate. The layout of the filter in 6.4 GHz frequency band is presented in Figure 3.28.

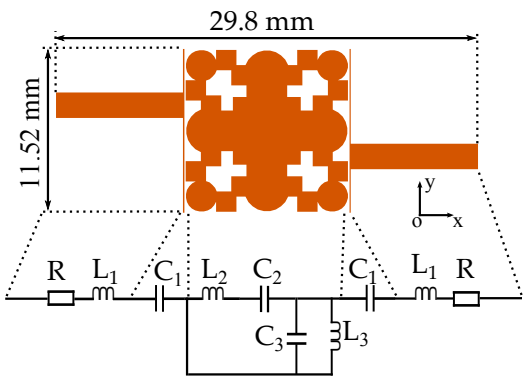


Figure 3.28: Layout of the BPF with its characteristic circuit model

In order to determine the characteristics of the BPF two approaches could be followed.

The first one is to model the BPF using its equivalent circuit (or at least a simplified version) as it can be seen in Figure 3.28. The resonator unit-cell can

be model based on transmission line theory [25] providing that the unit-cell size is electrically small enough. The presented unit-cell is $\lambda_0/5$ and its dimensions are at the limit of application of such a model. In any case the model would comprise a series connection ($L_2$ and $C_2$) in parallel with the equivalent impedance of the parallel $L_3$ and $C_3$ components. In series with the mentioned circuit, the capacitance $C_1$ (formed between the resonator and each narrow coupling line) and $L_l$ and $R$ components (modeling the transmission line) are placed.

The second approach consists in explaining the physical phenomena under the filter behavior. To achieve this aim the modes propagation in the structure should be explained based on the dispersion diagram so the second approach is followed.

The dimensions of the filter are 29.8 x 11.52 x 0.762 mm$^3$ ($0.64\lambda_0$ x $0.25\lambda_0$ x $0.016\lambda_0$, $\lambda_0$ is the free space wavelength, $\lambda_0$= 47 mm at 6.4 GHz) considering the input/output feeding lines and 11.92 x 11.52 x 0.762 mm$^3$ ($0.25\lambda_0$ x $0.25\lambda_0$ x $0.016\lambda_0$) without the input/output feeding lines.

From simulation results in Figure 3.29(a), the 3dB passband of BPF without harmonic suppression goes from 6.25 GHz to 6.62 GHz, meaning 5.75% fractional bandwidth at the center frequency 6.44 GHz. The minimum insertion loss is 1.7 dB whereas the maximum return loss value is greater than 17 dB (see Figure 3.29(b)).

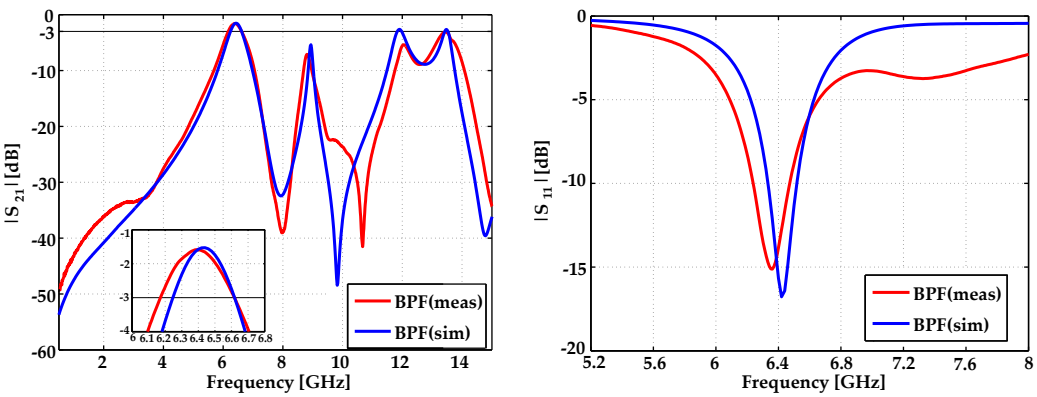


(a) $S_{21}$ (b) $S_{11}$

Figure 3.29: Transmission and reflection coefficients of the BPF in simulation and measurement.

Taking into account the position of the feeding lines with respect to the unit-cell geometry, the propagation follows a quasi-diagonal path, which coincides with the (M-R) region from the dispersion diagram together with part of the (X-M) region. Furthermore, from the (M-R) region, as well as part of the (X-M) region of the dispersion diagram, it resulted that the first mode propagates in the frequency spectrum between 6 GHz and 6.6 GHz. This band corresponds to the electromagnetic

wave propagation through the BPF geometry whereas from 7 GHz to 7.9 GHz the structure does not allow any mode propagation which corresponds to the stopband frequency region of the BPF.

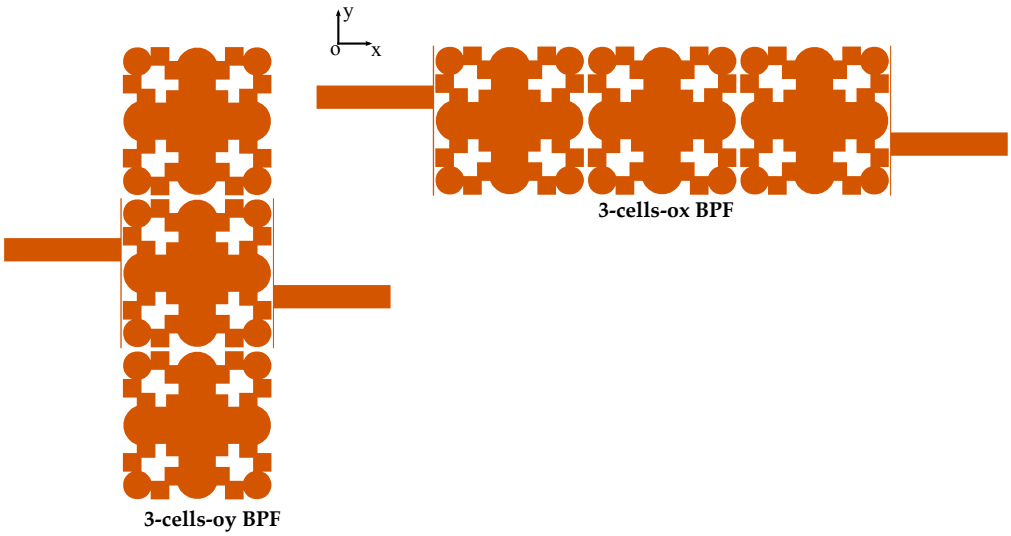


Figure 3.30: Layout of the 3-cells-oy BPF and 3-cells-ox BPF

In Table 3.5 the 3 dB bandwidth together with the quality factor Q are presented. In a band-pass filter, the overall width of the passband between the upper and lower 3 dB levels of the filter determines the quality factor. The lower the value of the Q factor, the wider the bandwidth and consequently the higher the Q factor, the narrow and more selective the filter. According to the analysis shown in Table 3.5, if three resonators are cascaded in the OY direction (henceforth referenced as 3-cells-oy BPF, see Figure 3.30) the 3 dB passband goes from 6.45 GHz to 6.61 GHz, meaning 2.45% fractional bandwidth at the center frequency 6.52 GHz whereas in the OX direction (filter henceforth referenced as 3-cells-ox BPF) the 3 dB passband goes from 6.55 GHz to 6.67 GHz, meaning 1.8% fractional bandwidth at the center frequency 6.62 GHz.

Moreover, using three unit-cells in the direction of the current flow, the filter becomes more selective (see Figure 3.31). The increment in the number of unit-cells in the OY direction has an influence only in the passband of the filter, which becomes narrower; meanwhile the slope in the stop bands remains the same. The benefit of the novel BPF over the square shaped resonator BPF is a quality factor three times greater. Figure 3.31 shows that the return loss increases with the number of unit-cells.

| Prototype | $f_c$ | 3 dB | | BW (3dB) | Q | Size (mm x mm) |
|---|---|---|---|---|---|---|
| | | $f_{low}$ (GHz) | $f_{high}$ (GHz) | GHz / % | | |
| BPF | 6.44 | 6.25 | 6.62 | 0.37 / 5.57 | 17.40 | 29.80x11.52* 11.92x11.52 |
| 3-cells-oy-BPF | 6.52 | 6.45 | 6.61 | 0.16 / 2.45 | 40.75 | 29.80x34.56* 11.92x34.56 |
| 3-cells-ox-BPF | 6.62 | 6.55 | 6.67 | 0.12 / 1.81 | 55.16 | 52.84x11.52* 11.92x34.56 |
| Square BPF | 6.70 | 6.13 | 7.30 | 1.17 / 17.4 | 5.72 | 29.80x11.52* 11.92x34.56 |
| * Considering the input/output feeding lines | | | | | | |

Table 3.5: Characteristics of the filters (simulations).

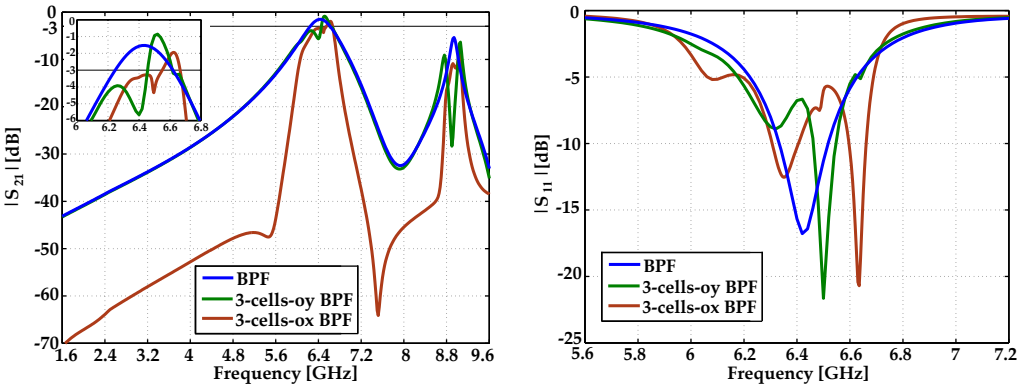


(a) $S_{21}$ (b) $S_{11}$

Figure 3.31: Transmission and reflection coefficients by varying the number of unit-cells in simulation .

#### 3.4.1.2 Second Harmonic Suppression

In order to suppress the second harmonic, several techniques have been reported in literature. In [26] two quarter wavelength open ended stubs are attached at the edges of the resonators in the main coupling path in order to have harmonic suppression but this implies additional circuit elements against compact filter design. Another interesting alternative, such as using a continuous modulation in the coupled section of the filter [27] and using Koch fractal geometry [28] have also been considered, but both are time consuming due to the need of many parameters optimization. In this Doctoral Thesis, defected ground structures (DGS) are used to act as a low-pass filter. The slots are placed in the ground plane, directly under the input/output feeding lines [29].

The dimensions of the slots are chosen as $c = 6.6$ mm, $d = 5$ mm, $f = 1.3$ mm, $g = 0.4$ mm, $l = 4.8$ mm, $m = 4.4$ mm, $n = 1.3$ mm, $x = 1.6$ mm, $y = 1.9$ mm (see Figure 3.32(a)). The conductor strip of the microstrip line on the top plane has a width of 1.8 mm, corresponding to a 50 Ω characteristic impedance.

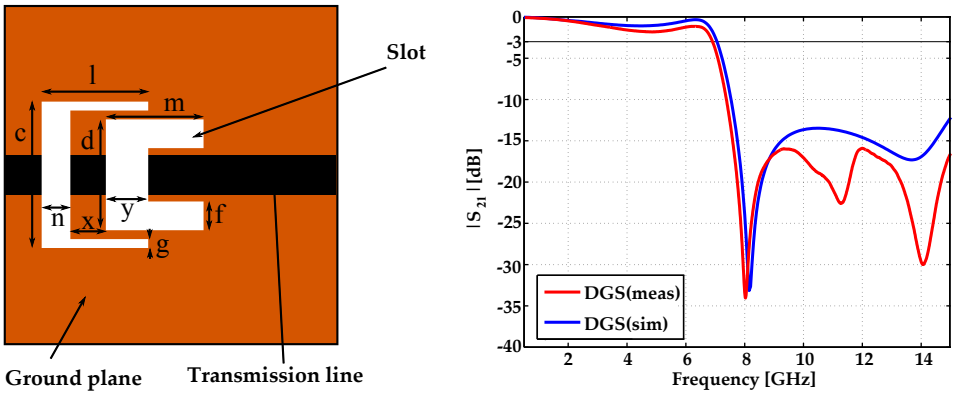


(a) Topology of the DGS section (bottom view)

(b) Transmission coefficient of the DGS section

Figure 3.32: DGS section - design and characterization.

From simulation results in Figure 3.32(b), the DGS structure under the microstrip transmission line exhibits a 3 dB cutoff frequency at 7.15 GHz and a center frequency of the stopband at 8.25 GHz with a maximum attenuation of 33 dB.

The dimensions of the slots placed in the ground plane influence the 3 dB cutoff frequency and the attenuation. Figure 3.33 shows the parametric study of the most important parameters $x$, $l$, $m$ and $c$. Only one parameter is changed at a time during the analysis. By increasing the $x$ parameter, the 3 dB cutoff frequency decreases whereas the attenuation is almost the same at 8.25 GHz. The $l$ parameter controls

both the attenuation at the center frequency of the stopband and the 3 dB cutoff frequency. On decreasing $l$, the center frequency of the stopband, the attenuation and the 3 dB cutoff frequency increase. The parameters $c$ and $m$ influence only the 3 dB cutoff frequency. The 3 dB cutoff frequency decreases when the parameters $c$ and $m$ decrease.

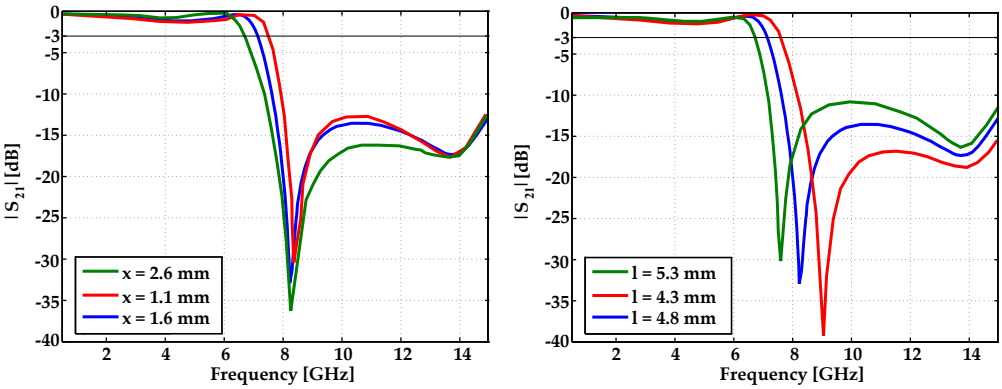


(a) $x$ variation




(b) $l$ variation

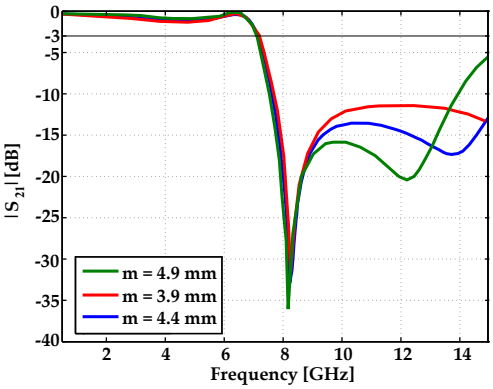


(c) $m$ variation

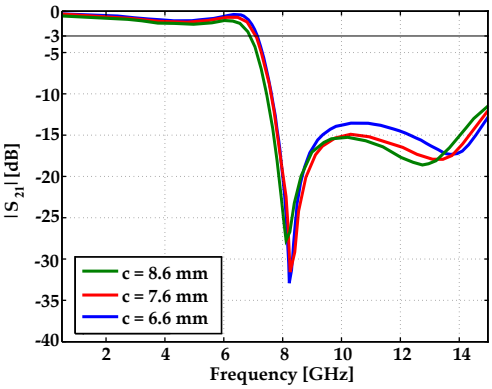


(d) $c$ variation

Figure 3.33: Parametric analysis of the DGS structure.

#### 3.4.1.3 Measurement Results

Prototypes of the band-pass filter with second harmonic suppression (henceforth referenced as BPF-DGS) and without harmonic suppression using one unit-cell resonator have been manufactured (see Figure 3.34).

The results of measured transmission coefficient for the BPF-DGS and BPF prototypes are depicted in Figure 3.35. The measured 3 dB bandwidth goes from

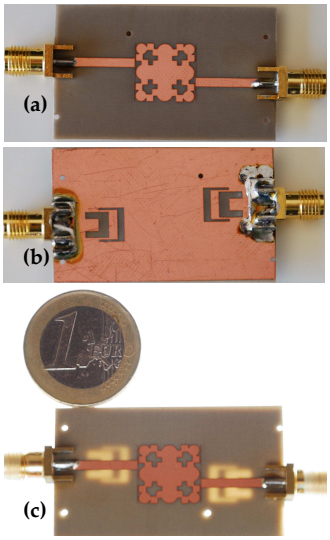


Figure 3.34: Manufacutured prototype BPF-DGS. (a) Top view. (b) Bottom view. (c) Cross-section view.

6.16 GHz to 6.62 GHz (7.18% fractional bandwidth at the center frequency 6.4 GHz), for the BPF prototype. There is good agreement between measurement and simulation results for the filter without harmonic suppression.

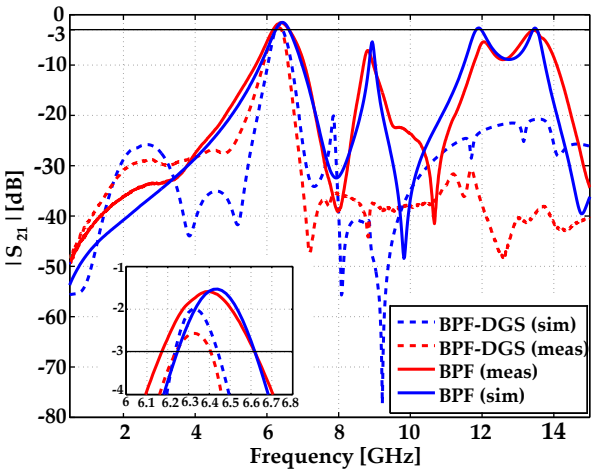


Figure 3.35: Transmission coefficient of the BPF and BPF-DGS in simulation and measurement.

Regarding the BPF-DGS prototype, a 3 dB passband that goes from 6.22 GHz to 6.43 GHz (3.32% fractional bandwidth at the center frequency 6.32 GHz) is obtained

in simulation whereas, in measurements, the 3 dB passband goes from 6.225 GHz to 6.4 GHz (2.76% fractional bandwidth at the center frequency 6.33 GHz). In the stopband regions some slightly differences between measurement and simulation can be observed. The fact that commercial MoM software considers infinite extension of the dielectric substrate together with manufacturing process tolerances and cables' and connectors' losses explains the differences in the stopband region.

Nevertheless, the simulations and measurement results are in good agreement and they meet the application requirements in the C band range. The filter with DGS exhibits approximately 50% less passband than the BPF without harmonic suppression because of the reduced coupling generated.

The absence of multilayer substrates and vias make the filters suitable to be used not only in satellite/terrestrial communication applications, but also in wearable applications where the prototypes could be shape adapted and bended. From Table 3.6, it can be easily seen that the size of the proposed BPF is minimized compared to band-pass filters with similar performance and substrate as used in [30], [33, 34, 35], whereas the BPF-DGS shows a higher quality factor.

The miniaturized BPF-DGS is demonstrated at 6.33 GHz, which is at higher frequency than the reported filter in [31]. If the proposed filter would be made to operate in the same frequency band as in [31], the filter would have a smaller size compared to [31].

In [36], the proposed filter renders a quality factor of 6.26, which is approximately three or six times lower compared to 17.4 of the BPF and 36.38 of the BPF-DGS. In [38], the upper conducting layer of the filter is connected through the bottom ground plane using vias. Even though in [38] a $0.1\lambda_0$ x $0.023\lambda_0$ miniaturized band-pass filter is shown, with a lower quality factor, it has the disadvantage of high cost and a difficult manufacture process due to the use of vias which are vulnerable to environmental influences such as being insufficiently plated through or filled with solder. This may cause the delamination or cracking of the vias.

| Prototype | $f_c$ | 3dB | | BW (3dB) | Q | Size (mm x mm) $\lambda_0$- wavelength at the corresp. $f_c$ |
|---|---|---|---|---|---|---|
| | | $f_{low}$ [GHz] | $f_{high}$ [GHz] | GHz / % | | |
| BPF | 6.44 | 6.25 | 6.62 | 0.37 / 5.57 | 17.40 | 29.80x11.52* $0.63\lambda_0$x$0.25\lambda_0$* 11.92x11.52 $0.25\lambda_0$x$0.25\lambda_0$ |
| BPF-DGS | 6.33 | 6.23 | 6.40 | 0.17 / 2.76 | 36.38 | 29.80x11.52 $0.63\lambda_0$x$0.25\lambda_0$ |
| [30] | 5.65 | 5.46 | 5.84 | 0.38 / 6.72 | 14.80 | 46.20x11.50 $0.87\lambda_0$x$0.21\lambda_0$ |
| [31] | 5.71 | 5.58 | 5.83 | 0.25 / 4.46 | 22.80 | 40x40 $0.76\lambda_0$x$0.19\lambda_0$ |
| [31] | 5.71 | 5.39 | 6.02 | 0.63 / 11.14 | 9.06 | 40x40 $0.76\lambda_0$x$0.19\lambda_0$ |
| [32] | 6 | 5.88 | 6.12 | 0.24 / 4.05 | 25 | 15x13 $0.30\lambda_0$x$0.26\lambda_0$ |
| [33] | 6.8 | 6.63 | 6.96 | 0.33 / 4.90 | 20.6 | 20x22 $0.45\lambda_0$x$0.50\lambda_0$ |
| [34] | 5.25 | 5.09 | 5.35 | 0.26 / 4.90 | 20.2 | 45x14 $0.79\lambda_0$x$0.25\lambda_0$ |
| [35] | 5.24 | 5.14 | 5.38 | 0.24 / 4.57 | 21.8 | 19.8x17.9 $0.35\lambda_0$x$0.31\lambda_0$ |
| [36] | 5.2 | 4.78 | 5.61 | 0.83 / 16 | 6.26 | 26.3x9.9 $0.45\lambda_0$x$0.17\lambda_0$ |
| [37] | 5.7 | 5.54 | 5.86 | 0.32 / 5.6 | 17.81 | 26x8 $0.50\lambda_0$x$0.15\lambda_0$ |
| [38] | 1.42 | 1.36 | 1.49 | 0.13 / 9 | 10.9 | 22.14x5.08 $0.10\lambda_0$x$0.02\lambda_0$ |
| * Considering the input/output feeding lines | | | | | | |

Table 3.6: Comparison with other band-pass filters.

## 3.5 Conclusions

The electromagnetic band-gap properties of the 5.8 GHz EBG structure as well as the 6.2 GHz miniaturized polarization dependent EBG structure and 6.2 GHz / 10.5 GHz miniaturized dual band polarization insensitive EBG structure have been studied. There are various ways for identifying the electromagnetic band-gap properties of a EBG structures, the most widely used in engineering applications are the suspended microstrip method and the dispersion diagram. The dispersion analysis of any infinite EBG structure has been simulated and analyzed by imposing periodic boundary conditions with appropriate phase shifts onto the unit-cell in a suitable eigenmode solver. Regarding the propagation on a suspended microstrip, the measured transmission coefficient obtained by means of the suspended microstrip shows good agreement with the theoretical result, clearly showing the presence of a power transfer reduction band for the fabricated prototypes.

The reduction or total suppression of surface waves plays an a useful role in improving the radiation efficiency of antennas and also allows the control of unwanted side and back lobes in the radiation pattern. As neither of the unit-cells have vias to connect the metallization with the ground plane, the EBG and AMC behaviors do not coincide.

By taking advantage of the predicted dispersion diagram, the design of a band-pass filter with small dimensions and high selectivity has been presented. A prototype has been manufactured at 6.4 GHz and characterized based on transmission loss measurements. Second harmonic suppression was obtained using a DGS topology. The filter presents a high selectivity with a sharp passband to stop band transition. The compact size, low cost, simple fabrication and integration with other components in the system make it appropriate for satellite/terrestrial communication and wearable applications.

Moreover, bandwidth enhancement of microstrip patch antenna by means of EBG structure for 2.48 GHz frequency band has been shown. In order to broaden the antenna bandwidth, the power transfer reduction band of the EBG structure is designed to be adjacent to the frequency band of the patch antenna. From measurements it can be concluded that the patch antenna-EBG prototype improves the bandwidth of the patch antenna and preserves its radiation properties without being necessary to increase the prototype's size. The presented patch antenna-EBG prototype is compact, robust, does not require via holes or multilayer substrates, and could be easily integrated on flexible substrates or textiles. In addition it presents higher compatibility with standard planar fabrication technology.

# Bibliography


[1] R. E. Collin, “Field Theory of Guided Waves,” Second Edition, John Wiley and Sons, Inc. 1991.

[2] L. Brillouin, “Wave propagation in periodic structures, Electric Filters and Crystal Lattices,” McGraw-Hill Inc., 1946.

[3] L. Zhang, N.G. Alexopoulos, D. Sievenpiper, E. Yablonovitch, “An Efficient Finite-Element Method for the Analysis of Photonic Band-Gap Materials," Microwave Symposium Digest, IEEE MTT-S International, vol. 4, pp. 1703 – 1706, Jun. 1999

[4] R. Remski, “Modeling of photonic bandgap (PBG) structures using Ansoft HFSS 7 and Optometrics,” Ansoft International Road Show, August 2000.

[5] P. Kovacs, “Design and optimization of electromagnetic ban dgap structures,” Doctoral Thesis, Brno, 2010.

[6] F. R. Yang, K. P. Ma, Y. Qian, and T. Itoh, “A uniplanar compact photonic-bandgap (UC-PBG) structure and its applications for microwave circuit,” IEEE Trans. Microw. Theory Tech., vol. 47, no. 8, pp. 1509–1514, Aug. 1999.

[7] L. Yang, M. Fan, F. Chen, J. She, Z. Feng, “A novel compact electromagnetic-bandgap (EBG) structure and its applications to microwave circuits,” IEEE Transactions and Microwave Theory and Techniques, vol. 53, no. 1, pp. 183-190, 2005.

[8] A. Aminian, F. Yang, Y.R. Samii, “In-phase reflection and EM wave suppression characteristics of electromagnetic band gap ground planes,” IEEE AP-S Digest, vol. 4, pp. 430-433, 2003.

[9] M. E. de Cos, Y. Alvarez-Lopez, R.C. Hadarig and F. Las Heras Andres, “Novel SHF-Band Uniplanar Artificial Magnetic Conductors,” IEEE Antennas and Wireless Propagation Letters, vol. 9, pp. 44-47, 2010.

[10] R. C. Hadarig, M. E. de Cos, and F. Las-Heras, "Microstrip patch antenna bandwidth enhancement using AMC/EBG structures," International Journal of Antennas Propagation, vol. 2012, 2012.

[11] R. C. Hadarig, M. E. de Cos, and F. Las-Heras, "Novel Miniaturized Artificial Magnetic Conductor," IEEE Antennas and Wireless Propagation Letters, vol. 12, pp.174-177, 2013.

[12] Garg, R., Bhartia, I., Bahl, I., Ittipiboon, A., "Microstrip antenna design handbook," Artech House, Boston, 2001.

[13] H. F. Shaban, H. A. Elmikaty, and A. A. Shaalan, "Study the effects of electromagnetic band-gap (EBG) substrate on two patches microstrip antenna," Progress In Electromagnetics Research B, vol. 10, pp. 55–74, 2008.

[14] S. Chaimool, K. Chung, P. Akkaraekthalin, "Bandwidth and gain enhancement of microstrip patch antennas using reflective metasurface", IEICE Trans. Commun, vol. E93-B, no. 10, pp. 2496-2503, 2010.

[15] J. Liang J. and H.-Y. D. Yang, "Radiation Characteristics of a Microstrip Patch Over an Electromagnetic Bandgap Surface, " IEEE Trans. on Antennas and Propag., vol. 55, no. 6, pp. 1691-1697, 2007.

[16] M. E. de Cos, Y. Álvarez, F. Las-Heras, "Enhancing patch antenna bandwidth by means of uniplanar EBG-AMC," Microwave and Optical Technology Letters, vol. 53, no. 6, pp. 1372-1377, 2011.

[17] M.E. de Cos, F. Las-Heras, "Dual-Band Uniplanar CPW-Fed Monopole/EBG Combination With Bandwidth Enhancement," Antennas and Wireless Propagation Letters, IEEE , vol.11, pp.365-368, 2012.

[18] R.C. Hadarig, M. E. De Cos Gomez, Y. Alvarez, F. Las-Heras, "Novel bow-tie antenna on artificial magnetic conductor for 5.8 GHz radio frequency identification tags usable with metallic objects," IET Microw. Antennas Propag., vol. 5, pp. 1097-1102, 2011.

[19] M.S. Kam, T. Mo, Q. Xue, C.H. Chan, "A Compact Bandpass Filter With Two Tuning Transmission Zeros Using a CMRC Resonator," IEEE Transactions On Microwave Theory And Techniques, vol. 53, no. 3, pp. 895-900, 2005.

[20] C.Y, Hsu, C.Y, Chen, H.R., Chuang, H.R. "Shunted-Line Stepped-Impedance Resonator," IEEE Microwave Magazine. pp.34-48, 2012.

[21] G. Matthaei, L. Young, E. Jones, "Microwave filters, impedance matching networks, and coupling structures" Artech House, USA, 1980.

[22] G. Matthaei, "Design of Parallel-Coupled Resonator Filters," IEEE Microwave Magazine, pp. 78-87. 2007.

[23] H. Kuan, Y. Lin, R. Yang, R.; Y.A. Chang, "A multilayered parallel coupled microstrip bandpass filter with embedded SIR cells to have a broad upper rejection band," IEEE Microwave and Wireless Comp. Letters, vol. 20, no. 1, pp. 25-27, 2010.

[24] J.S. Hong, M.J. Lancaster, "Coupling of microstrip square open loop resonators for cross-coupled planar microwave filters," IEEE Trans. Microw. Theory Tech, vol. 44, no. 12, pp. 2099–2109, 1996.

[25] C. Caloz, T. Itho, "Electromagnetic metamaterials: Transmission line theory and microwave applications," Wiley Interscience, 2005.

[26] S. Karthikeyan, R.S. Kshetrimayum, "Harmonic suppression of parallel coupled microstrip line bandpass filter using CSRR," Progress in Electromagnetic Research Letters, vol. 7, pp. 193-201, 2009.

[27] T. Lopetegi, M.A.A.G. Laso, J. Hernández, M. Bacaicoa, D. Benito, M.J. Garde, M. Sorolla, M. Guglielmi, "New microstrip wiggly-line filters with spurious passband suppression," IEEE Trans. Microwave Theory and Techniques, vol. 49, no. 9, pp. 1593-1598, 2001.

[28] K. Kim, N.D. Kingsley, M.A. Morton, J. Papapolymerou, M.M. Tentzeris, J.G.G. Yook, "Fractal shaped microstrip coupled line band pass filters for suppression of 2nd harmonic," IEEE Microwave Theory and Techniques, vol. 53, no. 9, pp. 2943-2948, 2005.

[29] D. Woo, T. Lee, J. Lee, C. Pyo, W. Choi, "Novel U slot and V slot DGSs for bandstop filter with improved Q factor," IEEE Trans Microw. Theory and Tech., vol. 54, no. 6, pp. 2840-2847, 2006.

[30] B. Su, R. Huang, "5.8GHz bandpass filter design using planar couple microstrip lines," International Conf. on Communications, Circuits and Syst, vol. 2, pp. 1204 – 1207, 2004.

[31] C. Lugo, D. Thompson, J. Papapolymerou, "Reconfigurable Bandpass Filter with Variable Bandwidth at 5.8GHz using a capacitive gap variation technique," 33rd European Microwave Conference, 2003.

[32] Y. Dong, C. T. M. Wu, T. Itoh, "Miniaturised multi-band substrate integrated waveguide filters using complementary split-ring resonators", IET Microwaves, Antennas & Propagation, vol. 6, no. 6, pp. 611–620, 2012.

[33] W. Hung-Wei, R. Yang, "A New Quad-Band Bandpass Filter Using Asymmetric Stepped Impedance Resonators," IEEE Microwave And Wireless Components Letters, vol. 21, no. 4, pp. 203-205, 2011.

[34] C. Fu-Chang, Q. Chu, "Design of Compact Tri-Band Bandpass Filters Using Assembled Resonators," IEEE Transactions On Microwave Theory And Techniques, vol. 57, no. 1, pp. 165-171, 2009.

[35] C.H. Lee, G.H. Chung, C.C Hsu, "Balanced Dual-Band BPF With Stub-Loaded SIRs for Common-Mode Suppression," IEEE Microwave And Wireless Comp. Letters, vol. 20, no. 2, pp. 70-72, 2010.

[36] C.M. Cheng, C.F. Yang, "Develop Quad-Band (1.57/2.45/3.5/5.2 GHz) Bandpass Filters on the Ceramic Substrate," IEEE Microwave and Wireless Components Letters, vol. 20, no. 5, pp. 268-270, 2010.

[37] C.Y. Chen, C.Y. Hsu, "A Simple and Effective Method for Microstrip Dual-Band Filters Design," IEEE Microwave And Wireless Components Letters, vol. 16, no. 5, pp. 246-248, 2006.

[38] S.C. Lin, C.H. Wang, C.H. Chen, "Novel Patch-Via-Spiral Resonators for the Development of Miniaturized Bandpass Filters With Transmission Zeros," IEEE Transactions On Microwave Theory And Techniques, vol. 55, no. 1, pp. 137-146, 2007.

# Chapter 4

# General Conclusions and Future Lines

**Contents**


**4.1 Conclusions** . . . . . **147**
**4.2 Future Lines** . . . . . **149**


## 4.1 Conclusions

In this Doctoral Thesis the design and characterization of several electromagnetic band-gap (EBG) and artificial magnetic conductor (AMC) structures for low profile antenna applications have been studied and experimentally evaluated.

Research on EBG/AMC structures can be split into design, characterization and applications. The characteristics of EBG/AMC structures can be described by either employing electromagnetic simulations or by using analytical models.

Firstly, the in-phase reflection properties of artificial magnetic conductors using electromagnetic simulations are studied, followed by the integration antenna-AMC. The AMC structure designs are validated by experimental results obtained through the fabrication and measurement of prototypes on rigid dielectric substrates. The design at 5.8 GHz RFID band shows broad AMC operation bandwidth (7.7%), polarization angle independency and a simulated angular margin of stability under oblique incidence higher than ±40°. Due to the fact that the AMC will be used in RFID tags or in wearable antennas it is desirable to have AMC object shape adapted without loosing functionality. Therefore, a flexible AMC has been employed and characterized based on reflection coefficient phase. Two bending patterns have been

tested and compared to the flat prototype and just a 0.6% frequency shift of the manufactured bent prototypes is reported.

A method for reducing the resonance frequency of the AMC structure without increasing it's size has been employed. It consists in adding interdigital capacitors in the unit-cell geometry. The novel unit-cell is smaller than $\lambda_0/10$ and at the same time the angular margin of stability under oblique incidence is improved reaching $\pm 65°$. In addition, a technique for eliminating the polarization dependence of the miniaturized AMC structure is presented.

The characteristics of the AMC structure are determined also using an analytical model. The analytical model is easy to be used and yields an insight into the physical phenomena. For normal incident wave to the surface of the miniaturized AMC, the accuracy of the proposed model has been checked by designing various samples and the results have been validated by electromagnetic simulations.

The AMC has been combined with dipole antennas in UHF and SHF RFID bands in order to solve the dipole antenna's problem with metals and human tissue proximity. It has been shown that the metallic objects/human tissue do not degrade the behavior of the dipole antenna-AMC due to the AMC's in-phase reflection characteristics. The backward radiation toward the human body and the mismatch problems of dipole antennas associated with human tissue proximity can be overcome using the AMC. Moreover, under bent conditions, the prototype does not exhibit drastic performance degradation.

The periodic structure that comprises the AMC is characterized as an electromagnetic band-gap (EBG) to block the propagation of electromagnetic waves at certain frequency bands. The power transfer reduction band using the suspended microstrip method over the EBG structure and the band-gap resulted after computing the dispersion diagram are presented. Taking advantage of the power transfer reduction band, the EBG structure surrounds a microstrip patch antenna in order to enhance the operational bandwidth. In addition, the microstrip patch antenna's gain and directivity can be increased when more rows and columns surround the prototype, so a trade-off between performance and size must be taken.

Finally, a novel band-pass filter with high selectivity, small dimensions and second harmonic suppression is proposed. A good agreement has been found between the transmission coefficient obtained in the simulations and measurements.

## 4.2 Future Lines

Throughout the development of this Doctoral Thesis, many possible issues have been opened to extend the study of EBG/AMC structures and the applications to different designs of planar antennas.

The following are the recommendation of possible future work resulting from this research: to study the effect of the miniaturized polarization dependent EBG/AMC on a single band/dual band antenna, to design a tunable EBG/AMC structure for change its resonance by varying the diode polarization, to decrease even more the dimension of the miniaturized unit-cell by placing the interdigital capacitors on each side of the unit-cell, in this way increasing even more the capacitive coupling.

It would be advisable to continue studying other EBG/AMC structures which could lead to improved radiation or matching features.

# List of publications

Publications Directly Originated by the Doctoral Thesis

International Journal Papers

[1] **R.C. Hadarig**, M. E. de Cos Gomez and F. Las-Heras: "A Compact Band-Pass Filter with High Selectivity and 2nd Harmonic Suppression" Materials, vol.6, no.12, pp. 5613-5624, 2013.

[2] **R.C. Hadarig**, M. E. de Cos and F. Las-Heras: "UHF Dipole-AMC Combination for RFID Applications" IEEE Antennas and Wireless Propagation Letters, vol.12, pp. 1041-1044, 2013.

[3] **R.C. Hadarig**, M. E. de Cos and F. Las-Heras: "Novel Miniaturized Artificial Magnetic Conductor" IEEE Antennas and Wireless Propagation Letters, vol.12, pp. 174-177, 2013.

[4] **R.C. Hadarig**, M. E. de Cos and F. Las-Heras: "High-Performance Computational Electromagnetic Methods Applied to the Design of Patch Antenna with EBG Structure", International Journal of Antennas and Propagation, vol. 2012, pp.1-5, 2011.

[5] **R.C. Hadarig**, M. E. de Cos and F. Las-Heras: "Microstrip Patch Antenna Bandwidth Enhancement Using AMC/EBG Structures", International Journal of Antennas and Propagation, vol. 2012, pp.1-6, 2011.

[6] **R.C. Hadarig**, M. E. de Cos, Y. Alvarez, and F. Las-Heras: "Novel Bow-tie Antenna on Artificial Magnetic Conductor for 5.8 GHz Radio Frequency Identification Tags Usable with Metallic Objects", IET Microwaves, Antennas & Propagation, vol. 5, pp. 1097-1102, 2011.

[7] **R.C. Hadarig**, M. E. de Cos, Y. Alvarez, and F. Las-Heras: "Novel Bow-tie-AMC Combination for 5.8 GHz RFID Tag Usable with Metallic Objects", IEEE Antennas and Wireless Propagation Letters, vol. 9, pp. 1217-1220, 2010.

[8] M. E. de Cos, Y. Alvarez, **R.C. Hadarig** and F. Las-Heras: "Flexible Uniplanar Artificial Magnetic Conductor", Progress in Electromagnetics Research, PIER, vol. 106, pp. 349-362, 2010.

[9] M. E. de Cos, Y. Alvarez, **R.C. Hadarig** and F. Las-Heras: "Novel SHF band uniplanar Artificial Magnetic Conductor", IEEE Antennas and Wireless Propagation Letters, vol.9, pp. 44-47, 2010.

International Conference Papers

[1] **R.C. Hotopan**, M. E. de Cos and F. Las-Heras: "Small Sized Uniplanar Artificial Magnetic Conductor", 8th European Conference on Antennas and Propagation, EUCAP, The Hague, The Netherlands, April 6 – 11, 2014.

[2] **R.C. Hotopan**, M. E. de Cos and F. Las-Heras: "Reduced Size C-Band Band-pass Filter with 2nd Harmonic Suppression", 8th European Conference on Antennas and Propagation, EUCAP, The Hague, The Netherlands, April 6 – 11, 2014.

[3] **R.C. Hotopan**, M. E. de Cos, P. Rocca, A. Massa and F. Las-Heras: "Behavioral Study of a CPW-fed Dual-Band Antenna Combined with a Polarization Dependent AMC", 2013 IEEE International Symposium in Antennas and Propagation, Memphis, Tennessee, USA, July 6-12, 2014.

[4] **R.C. Hadarig**, M. E. de Cos and F. Las-Heras: "On The Bandwidth Enhancement Of Patch Antenna Using EBG/AMC Structures", 6th European Conference on Antennas and Propagation, EUCAP, Prague, Czech Republic, May 26 – 30, 2012.

[5] **R.C. Hadarig**, M. E. de Cos and F. Las-Heras: "Bandwidth Enhancement Through Coupling Microstrip Patch Antenna And Electromagnetic Band-Gap Resonances", 6th European Conference on Antennas and Propagation, EUCAP, Prague, Czech Republic, May 26 – 30, 2012.

[6] M. E. de Cos, Y. Alvarez, **R.C. Hadarig** and F. Las-Heras: "Flexible Uniplanar Artificial Magnetic Conductor", 5th European Conference on Antennas and Propagation, EUCAP, Rome, Italy, April 11 – 15, 2011.

[7] M. E. de Cos, Y. Alvarez, **R.C. Hadarig** and F. Las-Heras: "Novel SHF band uniplanar Artificial Magnetic Conductor", 4th Internacional Conference on advanced Electromagnetic Materials in Microwave and Optics, Metamaterials, Karlsruhe, Germany, Sept. 13 – 17, 2010.

# List of Figures


1.1 Classification of materials. . . . . 7
1.2 Phase change of incident wave for $\lambda_0/4$ spacing between the dipole antenna and PEC ground plane. . . . . 13
1.3 Radiating element (dipole antenna) lying parallel and close to the perfect electric conductor. . . . . 13
1.4 Radiating element (dipole antenna) separated $\lambda_0/4$ from the perfect electric conductor. . . . . 13
1.5 Radiating element (dipole antenna) lying parallel above a perfect magnetic conductor ground plane. . . . . 14
1.6 Radiating element (dipole antenna) lying parallel above an artificial magnetic conductor. . . . . 14

2.1 Impedance of a parallel resonant circuit. . . . . 25
2.2 Simple square unit-cell. . . . . 26
2.3 Simulation model for determining the reflection properties of the AMC. 29
2.4 Phase of the reflection coefficient on the AMC surface. . . . . 30
2.5 Magnitude of the reflection coefficient on the AMC surface. . . . . 31
2.6 Simulated surface impedance of the AMC. . . . . 31
2.7 Simulated reflection phase of the AMC structure using different dielectric substrates. . . . . 32
2.8 Reflection phase comparison for ARLON25N and RO4003C. . . . . 33
2.9 TE and TM polarized waves. Polarization and incidence angles variation schemes. . . . . 34
2.10 Simulated reflection phase of the AMC structure for different incident field ($E_{\mathrm{inc}}$) polarization angles ($\varphi$). . . . . 35
2.11 Simulated reflection phase of the AMC structure for TE and TM polarized waves for different incident angles ($\Theta_{\mathrm{inc}}$). . . . . 35
2.12 Possible bending patterns of a flexible AMC. . . . . 36

2.13 Reflection phase shifting versus scale factor of the unit-cell for the flat non-deformed RO3003 dielectric substrate. . . . . 37
2.14 AMC-1 unit-cell geometry. . . . . 38
2.15 Simulated reflection phase of the AMC-1 design. . . . . 39
2.16 AMC-1 and AMC-2 unit-cell geometries. . . . . 39
2.17 Reflection phase of the AMC-2 design using RO3010 dielectric substrate. 40
2.18 Reflection phase of the AMC-2 design using RO4003C dielectric substrate. . . . . 40
2.19 Simulated surface impedance of the AMC-2 design using RO4003C dielectric substrate. . . . . 41
2.20 Simulated reflection phase of the AMC-2 for different incident field ($E_{\mathrm{inc}}$) polarization angles ($\varphi$) for TE/TM polarized waves under normal incidence. . . . . 44
2.21 Simulated reflection phase of the AMC-2 for different oblique incident angles ($\Theta_{\mathrm{inc}}$) for both TE/TM polarized waves under 0° polarization angle. . . . . 45
2.22 Simulated reflection phase of the AMC structure for different oblique incident angles ($\Theta_{\mathrm{inc}}$) and 45° polarization angle for TE/TM polarized waves. . . . . 45
2.23 AMC unit-cell formed by 2x2 AMC-2 unit-cells. . . . . 46
2.24 Simulated reflection phase of the polarization insensitive AMC structure for normal incidence and 0° polarization angle. . . . . 47
2.25 Simulated surface impedance of the polarization insensitive AMC structure for normal incidence and 0° polarization angle. . . . . 47
2.26 Simulated reflection phase of the polarization insensitive AMC structure for different incident field ($E_{\mathrm{inc}}$) polarization angles ($\varphi$) for both TE and TM polarized waves under normal incidence. . . . . 48
2.27 Simulated reflection phase of the polarization insensitive AMC structure for different oblique incident angles ($\Theta_{\mathrm{inc}}$) for both TE and TM polarized waves under 0° polarization angle. . . . . 48
2.28 Reflection coefficient measurement setup in anechoic chamber. . . . . 50
2.29 LPKF Proto Laser-S machine. . . . . 50
2.30 Unit-cell geometry. a) side view, b) planar AMC manufactured prototype. . . . . 51
2.31 Reflection phase of the simulated and manufactured AMC prototype. 52
2.32 Reflection phase of the manufactured AMC prototype for different incident field ($E_{\mathrm{inc}}$) polarization angles ($\varphi$). . . . . 53

2.33 Reflection phase of the manufactured AMC prototype for different incident angles ($\Theta_{\text{inc}}$). . . . . 53
2.34 Bending patterns. (a) Creeping prototype with $W_1 = 56.6$ mm, $W_2 = 30.0$ mm, $W_3 = 21.5$ mm, $W_4 = 18.3$ mm and $h = 5$mm, (b) smooth prototype with $W = 120$ mm, and $h = 10$ mm. . . . . 54
2.35 Reflection coefficient measurement setup in anechoic chamber. . . . . 55
2.36 Reflection phase of the flat (simulation and measurement) and bent (measurements) prototypes. . . . . 56
2.37 Reflection phase of the manufactured smooth AMC prototype for different incident field ($E_{\text{inc}}$) polarization angles ($\varphi$). . . . . 57
2.38 Reflection phase of the manufactured flat AMC prototype for different incident angles ($\Theta_{\text{inc}}$). . . . . 58
2.39 Reflection phase of the manufactured smooth AMC prototype for different incident angles ($\Theta_{\text{inc}}$). . . . . 58
2.40 Manufactured AMC-2 prototype. . . . . 59
2.41 Reflection phase of the AMC-2 design using RO3010 and RO4003C dielectric substrates. . . . . 60
2.42 Reflection phase of the manufactured AMC-2 structure for different incident field ($E_{\text{inc}}$) polarization angles ($\varphi$) under normal incidence. . 61
2.43 Reflection phase of the manufactured AMC-2 structure for different oblique incident angles ($\Theta_{\text{inc}}$) under 0° polarization angle. . . . . 62
2.44 Manufactured polarization insensitive AMC prototype. . . . . 62
2.45 Reflection phase of the manufactured polarization insensitive AMC prototype. . . . . 63
2.46 Lower frequency band. Reflection phase of the manufactured polarization insensitive AMC prototype for different incident field ($E_{\text{inc}}$) polarization angles ($\varphi$) under normal incidence. . . . . 64
2.47 TE polarized waves. Reflection phase of the manufactured polarization insensitive AMC prototype for different incident angles ($\Theta_{\text{inc}}$). . 65
2.48 TM polarized waves. Reflection phase of the manufactured polarization insensitive AMC prototype for different incident angles ($\Theta_{\text{inc}}$). . 65
2.49 Semi-infinite strips. . . . . 66
2.50 Surface impedance of an AMC. . . . . 67
2.51 Surface impedance of an AMC. . . . . 67
2.52 AMC-2 unit-cell - Equivalent circuit model of the grid impedance for TE and TM polarized waves. . . . . 69

2.53 Simulated reflection phase of the AMC-2 resulted from the electromagnetic simulation and analytical model when $\Theta_{\text{inc}}$ is varied for TE polarized plane waves. . . . . 71
2.54 Simulated reflection phase of the AMC-2 resulted from the electromagnetic simulation and analytical model for normal incidence. . . 72
2.55 The effect of the capacitive interdigital fingers' length for *TE (0°, 0°)*. 73
2.56 The effect of inductive component width for *TE (0°, 0°)*. . . . . 74
2.57 The effect of gap width for *TE(0°, 0°)*. . . . . 75
2.58 The effect of dielectric substrate thickness for *TE(0°, 0°)*. . . . . 75
2.59 The effect of dielectric substrate permittivity. . . . . 76
2.60 Equivalent circuit model. . . . . 77
2.61 Comparison between the simulation results and the analytical model of the AMC. . . . . 78
2.62 Elements of the manufactured prototype: (a) double bow-tie antenna; (b) AMC unit-cell arrangement; (c) Bow-tie-AMC prototype. . . . . 81
2.63 Return loss of CPW-fed double bow-tie antenna versus geometry dimensions. . . . . 82
2.64 Simulated return loss of the CPW-fed double bow-tie antenna. . . . 82
2.65 Bow-tie-AMC prototype layout. . . . . 83
2.66 Return loss of the CPW-fed double bow-tie antenna. . . . . 84
2.67 Different AMC unit-cells arrangements combined with the double bow-tie antenna: (Left to right) Bow-tie-AMC, Bow-tie-AMC-#2 and Bow-tie-AMC-#3. . . . . 84
2.68 Measured return loss for the Bow-tie-AMC, Bow-tie-AMC-#2 and Bow-tie-AMC-#3 prototypes. . . . . 85
2.69 Measured return loss for the Bow-tie-AMC design and for the Bow-tie and Bow-tie-AMC designs on a metallic plate. . . . . 86
2.70 Simulated surface currents distribution (normalized). . . . . 87
2.71 Measurement setup in anechoic chamber for Bow-tie-AMC at (Left) the edge and (Right) centered on a metallic plate. . . . . 87
2.72 Bow-tie and Bow-tie-AMC measured radiation pattern (normalized in dB) (Left) E plane and (Right) H plane without metallic plane. . 88
2.73 Bow-tie-AMC measured radiation pattern when placed on a metallic plate (normalized in dB) (Left) E-plane and (Right) H-plane. . . . . 88
2.74 Simulated antenna bandwidth and gain. . . . . 89
2.75 Antenna-AMC layout. . . . . 90
2.76 Manufactured prototypes. . . . . 90
2.77 Reflection coefficient of the prototypes. . . . . 91

2.78 Antenna and antenna-AMC measured radiation pattern (normalized in dB) (Left) E-plane and (Right) H-plane. . . . . 91
2.79 Geometry of the proposed dipole antenna (top view and bottom view) fed using a balance to unbalance (balun) transition. . . . . 92
2.80 Simulated return loss of the dipole antenna without balun versus geometry parameters. . . . . 93
2.81 Return loss of the Dipole antenna in simulations. . . . . 94
2.82 Manufactured prototypes. (a) Dipole-AMC. (b) Dipole-AMC fixed over a metallic plate. (c) Dipole-AMC bent and surrounding a metallic can. (d) Dipole-AMC conformed around the human wrist. . . . . 95
2.83 Return loss of the Dipole antenna. . . . . 96
2.84 Return loss of the Dipole-AMC prototype. . . . . 97
2.85 Influence of the metallic can/plate on the return loss of the Dipole-AMC prototype in measurements. . . . . 97
2.86 Measured return loss of the Dipole-AMC prototype conformed around the wrist and Dipole-AMC prototype bent in free space. . . . . 98
2.87 Dipole measured radiation pattern (normalized, in dB) in the E-plane and H-plane at 868MHz. . . . . 99
2.88 Dipole-AMC measured radiation pattern (normalized, in dB) in the E-plane and H-plane at 868MHz. . . . . 100

3.1 Brillouin triangle. . . . . 110
3.2 Dispersion diagram of a totally symmetric square unit-cell with and without vias. . . . . 111
3.3 Suspended microstrip scheme. . . . . 112
3.4 Power transfer reduction band with and without EBG structure. . . 113
3.5 Unit-cell resonator - The applied boundary conditions with the irreducible Brillouin triangle. . . . . 114
3.6 Dispersion diagram of the EBG structure for different dimensions of the unit-cell and different dielectric substrates. . . . . 115
3.7 Suspended microstrip setup. . . . . 116
3.8 Power transfer reduction band of the 4x4 periodic structure using different dielectric substrates and different dimensions of the unit-cell. 116
3.9 Comparison between the AMC and EBG behaviors. . . . . 118
3.10 Polarization dependent EBG structure. . . . . 118
3.11 Comparison between the AMC and EBG behaviors for the polarization dependent structure. . . . . 119
3.12 Polarization insensitive EBG structure. . . . . 120

3.13 Comparison between the AMC and EBG behaviors for the polarization insensitive structure. . . . . 121
3.14 5.8 GHz EBG design - characterization and results. . . . . 121
3.15 Polarization dependent EBG - characterization and results. . . . . 122
3.16 Polarization insensitive EBG - characterization and results. . . . . 122
3.17 Manufactured prototypes: (a) Patch antenna; (b) Patch antenna-EBG. . . . . 124
3.18 Resonances to be coupled in order to achieve bandwidth enhancement. 124
3.19 Return loss of the Patch antenna-EBG versus parameter $a$. . . . . 125
3.20 Bandwidth of the Patch antenna-EBG versus parameter $a$. . . . . 126
3.21 Patch antenna-AMC prototype layout. . . . . 126
3.22 Simulation and measurement comparison between the prototypes: patch antenna and patch antenna-EBG. . . . . 127
3.23 Measurement comparison between the prototypes: patch antenna, patch antenna-EBG and patch antenna-AMC. . . . . 128
3.24 Measured radiation diagram of the prototypes: patch antenna and patch antenna-EBG. . . . . 129
3.25 Measured radiation diagram of the prototypes: patch antenna and patch antenna-AMC. . . . . 129
3.26 Different unit-cell arrangements combined with the patch antenna. a) Patch antenna-EBG-#2, b) Patch antenna-EBG-#3, and c) Patch antenna-EBG #4. . . . . 131
3.27 Simulated return loss for the Patch antenna-EBG, Patch antenna-EBG-#2, Patch antenna-EBG-#3 and Patch antenna-EBG-#4. . . . 131
3.28 Layout of the BPF with its characteristic circuit model . . . . . 133
3.29 Transmission and reflection coefficients of the BPF in simulation and measurement. . . . . 134
3.30 Layout of the 3-cells-oy BPF and 3-cells-ox BPF . . . . . 135
3.31 Transmission and reflection coefficients by varying the number of unit-cells in simulation . . . . . 136
3.32 DGS section - design and characterization. . . . . 137
3.33 Parametric analysis of the DGS structure. . . . . 138
3.34 Manufacutured prototype BPF-DGS. (a) Top view. (b) Bottom view. (c) Cross-section view. . . . . 139
3.35 Transmission coefficient of the BPF and BPF-DGS in simulation and measurement. . . . . 139

# List of Tables


2.1 Comparative study of the AMC unit-cell using different dielectric substrates (simulations). . . . . 33
2.2 Analysis of presented miniaturized unit-cells (simulations). . . . . 41
2.3 Unit-cell size comparison for 2.45 GHz and RO TMM6 dielectric substrate ($\varepsilon_r = 6$, dielectric thickness $h = 2.54$ mm). . . . . 42
2.4 Unit-cell size comparison for RO3010 dielectric substrate ($\varepsilon_r = 10.2$, dielectric thickness $h = 1.27$ mm). . . . . 42
2.5 Unit-cell size comparison for $\varepsilon_r = 2.2$, dielectric thickness $h = 1$ mm. 43
2.6 Unit-cell size comparison between [29] and AMC-2 design for $\varepsilon_r = 13$. 43
2.7 Prototypes' comparison . . . . . 56
2.8 Analysis of presented miniaturized AMC-2 unit-cell. . . . . 60
2.9 Manufactured protototypes' gain. . . . . 87
2.10 Measured gain, directivity and radiation efficiency of the manufactured prototypes. . . . . 92
2.11 Gain, directivity and radiation efficiency of the prototypes. . . . . 101

3.1 Band-gap width for different dimensions of the unit-cell (simulations). 115
3.2 Gain, directivity and radiation efficiency of the prototypes. . . . . 128
3.3 CP-XP ratio comparison. . . . . 130
3.4 Radiation properties of the patch antenna combined with different cell arrangements. (simulations). . . . . 132
3.5 Characteristics of the filters (simulations). . . . . 136
3.6 Comparison with other band-pass filters. . . . . 141